Anomalous Dynamics
of Disordered Materials

Zihua Liu

Anomalous Dynamics of Disordered Materials

Zihua Liu

Anomalous Dynamics of Disordered Materials

Anomale Dynamica van Wanordelijke Materialen
(met een samenvatting in het Nederlands)

Proefschrift

ter verkrijging van de graad van doctor aan de
Universiteit Utrecht
op gezag van de
rector magnificus, prof. dr. H.R.B.M. Kummeling,
ingevolge het besluit van het College voor Promoties
in het openbaar te verdedigen op

maandag 24 juni 2024 des middags te 12.15 uur

door

Zihua Liu

geboren op 15 september 1993
te Jinzhong city, China

路漫漫其修远兮，吾将上下而求索。
The road ahead is long and arduous,
I shall venture up and down in search of answers.

屈原（Qu Yuan） (c.340 BC – 278 BC)

List of papers

- Liu Z, Panja D, Barkema G T. Structural dynamics of polycrystalline graphene[J]. *Physical review E*, 2022, 105(4): 044116.

- Liu Z, Vatansever E, Barkema G T, et al. Critical dynamical behavior of the Ising model[J]. *Physical review E*, 2023, 108(3): 034118.

- Liu Z, Panja D, Barkema G T. Domain Growth in Polycrystalline Graphene[J]. *Nanomaterials*, 2023, 13(24): 3127.

- Liu Z, Panja D, Barkema G T. Structural dynamics of a model of amorphous silicon (Under review).

Contents

Introduction

Abstract

The mystery of the universe stems from the inherent disorder on its spatial scale and its constant evolution, which is manifested in the study of the dynamics of disordered systems and materials. In this chapter, we introduce the basic concepts of disordered materials and anomalous dynamics, the two central to the theme of this thesis. An outline of this paper is also presented.

1.1 Ordered and disordered materials

In material science, disordered materials can be defined clearly and straightforwardly as having an arrangement of atoms/molecules that is not crystalline. Let's begin with crystals that are often regarded as structure with order. Crystals are ordered since they can be obtained by periodical translation of an elementary (geometric) cell in space. In other words, in a crystal an assembly of particles (atoms or molecules) is packed in a regular structure along lines in space and planes in a geometric lattice [1]. Disordered materials are without long range order, but typically have significant local chemical and topological order. Unlike the case of a crystal, the order rapidly decays with distance: distances of second neighbors are more uncertain than for first neighbors, and so on. The decay of these spatial correlations is an experimental observable that is accessible via diffraction. Well-known disordered states of matter are liquids and gases, but there are more disordered solids, such as polycrystals, glasses, polymer melts, and gels. Also these have garnered widespread attention and research due to their unique structures which exhibit intriguing transport, thermal conductivity, and mechanical properties. Fig. 1.1 succinctly illustrates the comparison between disordered solid materials and single crystals.

Disordered

Crystalline   Polycrystalline   Amorphous
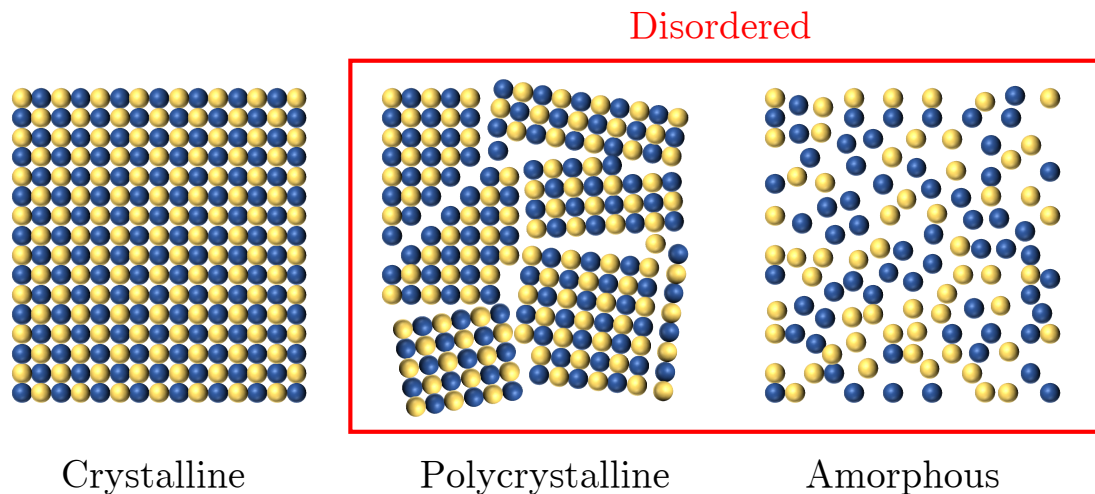
Figure 1.1: The comparesion of crystalline and disordered states for solid.

In this thesis, polycrystalline graphene and amorphous silicon (a-Si) (as shown in Fig. 1.2) have been selected as the two types of disordered solids for my primary research. Graphene, with its remarkable electrical, mechanical, and thermal properties, has been a subject of intense research since its first isolation in 2004 by Andre Geim and Konstantin Novoselov [2]. This two-dimensional (2D), one-atom-thick layer of carbon atoms arranged in a hexagonal lattice has shown promise for revolutionizing fields ranging from electronics and energy storage to materials science and nanotechnology [3–7].

Due to the limitations of fabrication technology, the synthesized graphene is mostly present in a polycrystalline state [8]. Polycrystalline graphene retains many of the extraordinary properties of its single-crystal counterpart but introduces new physics and phenomena due to the presence of grain boundaries. These grain boundaries, typically characterized by their mismatch angles and the arrangement of pentagonal, hexagonal, and heptagonal carbon rings, can significantly impact the material's overall properties [9–11].

Amorphous silicon (a-Si) is a non-crystalline form of silicon that has garnered significant interest in the field of electronics and photovoltaics. Unlike its crystalline counterpart, amorphous silicon is characterized by a random network of silicon atoms. This lack of long-range order gives a-Si unique electronic and optical properties that differ significantly from crystalline silicon (c-Si). Early studies on the structure of amorphous silicon (a-Si) primarily relied on X-ray scattering experiments and electron microscope imaging. Over the past half-century, the development of computer-assisted research technologies has led to the proposition of various structural topology models for a-Si, which have enhanced our understanding of its complex structure and propelled applications in various fields such as optoelectronics and solar cells [12, 13].

The electronic and mechanical properties of polycrystalline graphene and a-Si have been well-studied over the past few decades. The dynamical properties related to mechanical characteristics are, however, still poorly understood. Chapters 3 to 5 of this thesis discuss and investigate the dynamical properties of polycrystalline graphene and a-Si in the hope of filling gaps in knowledge in this research area.

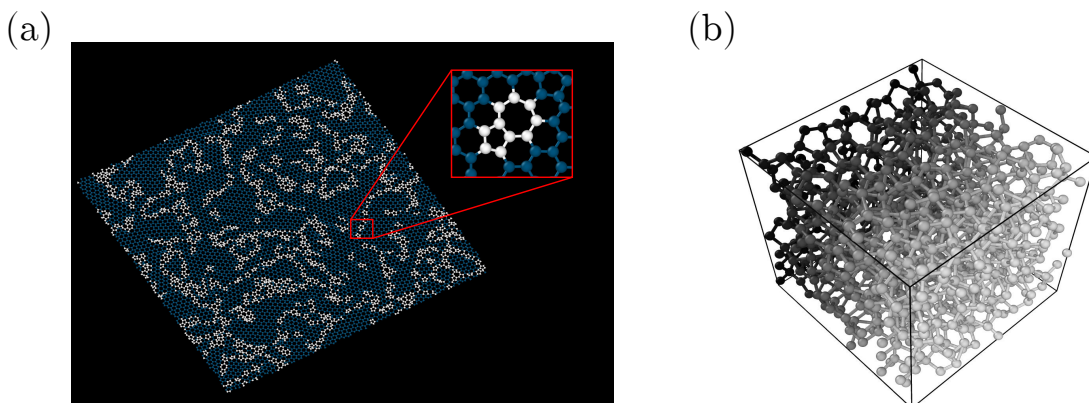(a)   (b)

Figure 1.2: (a) A buckled polycrystalline graphene sample with grain boundaries constituted by pairs of 5-7 rings are marked in white. (b) A sample of amorphous silicon.

1.2   Ising model
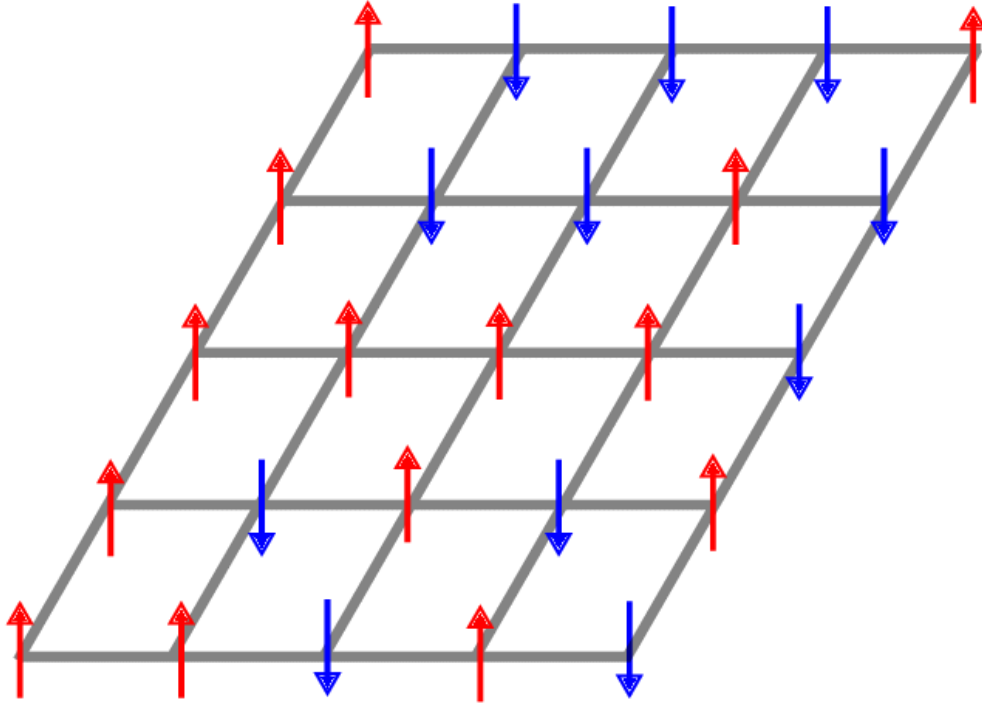
Figure 1.3: A schematic diagram of a two-dimensional square Ising lattice [14], where red and blue arrows represent spins oriented upwards and downwards, respectively.

The Ising model, named after the German physicist Ernst Ising [15], is a fundamental model in statistical mechanics and condensed matter physics. It serves as a crucial framework for understanding the behavior of magnetic materials, ferromagnetism in particular. The Ising model is a binary spin system, where each spin can take one of two possible values, typically denoted as "up" or "down", as shown in Fig. 1.3. Red and blue arrows represent spins oriented upwards and downwards, respectively. In the simplest case of Ising model, without an external field, the Hamiltonian of the Ising model on a $L \times L$ square lattice is defined as

$$\mathcal{H} = -J \sum_{\langle i,j \rangle} s_i s_j. \tag{1.1}$$

Here, J is the interaction strength between spins, $s_i = \pm 1$ is the orientation of the spin at site i, and the summation runs over all pairs of nearest-neighbor spin sites. It has been proved that a phase transition does exist for spatial dimensions $d \geq 2$ [16]. The critical temperature has been reported to be $T_c = 2/\ln(1 + \sqrt{2})$ and 4.5116174(2) for $d = 2$ and $d = 3$, respectively [17].

Several well-known algorithms have been proposed for the simulation study of Ising dynamics. For example, Glauber dynamics [18, 19], Kawasaki Dynamics [20], or cluster dynamics [21, 22]. The difference between Glauber and Kawasaki dynamics is whether the magnetization is locally conserved or not. In Kawasaki dynamics, the spins at neighboring sites are proposed to be exchanged, which keeps the magnetization constant and is particularly useful for the study of the conserved-order-parameter (COP) Ising model. The Wolff algorithm is usually faster than Glauber dynamics. Glauber dynamics is solely considered in the thesis. Glauber dynamics is a single-spin-flip dynamics, where spin flips are proposed at random locations, which are then either accepted or rejected according to the Metropolis algorithm [18]. For a transition from state u to state v, the resulting energy difference $\Delta E = E_v - E_u$ is measured. If $\Delta E < 0$, the proposed flip is always accepted; otherwise, the flip is accepted with the probability $e^{-\beta \Delta E}$, with inverse temperature $\beta = (kT)^{-1}$, in which k is the Boltzmann constant and T is temperature.

1.3   Anomalous dynamics
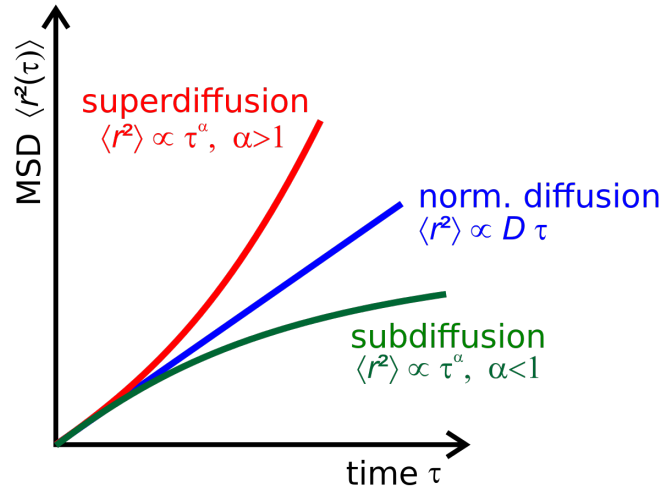
Figure 1.4: In a double-logarithmic plot, the variation of the mean square displacement (MSD) with respective to time for normal and anomalous diffusion, respectively. JKRIEGER/(CC BY-SA 3.0)

In classical Brownian motion or normal diffusion, the mean square displacement (MSD) of particle motion exhibits a linear dependence on time, as described by the Einstein-Smoluchowski equation:

$$\langle (r(t) - r(0))^2 \rangle = 2dDt, \tag{1.2}$$

where $r(t)$ is the position at time t, d is the dimensionality and D is the so-called diffusion coefficient. In the case of anomalous diffusion, the relationship between the mean square displacement and time τ is no longer linear and follows a power-law dependence:

$$\langle (r(t) - r(0))^2 \rangle \propto t^{\alpha}, \tag{1.3}$$

in which α is a positive exponent that is not equal to one. Based on the value of α, anomalous diffusion can be categorized into two types.

When $\alpha > 1$, the diffusion is referred to as superdiffusion or enhanced diffusion. In this regime, particles move faster than they would during conventional Brownian motion, and the mean square displacement grows more rapidly than a linear function of time. This behavior may be due to long-distance movement events or persistent driving forces such as convective flows in fluids [23].

When $\alpha < 1$ the phenomenon is known as subdiffusion or slowed diffusion. In subdiffusive behavior, the particle displacement increases slower than it would in conventional Brownian motion. This is often due to the presence of obstacles or traps, such as in porous media [24] or colloidal gels [25], where particles are hindered by obstructions.

Anomalous diffusive behavior has been observed in a variety of natural and engineered systems, including molecular motion within living cells [26, 27], time series of economic indicators [28], and the spread of contaminants in the environment [29]. The study of anomalous diffusion contributes to a deeper understanding and description of transport processes in these complex systems.

1.3.1 A simple example

A well-known one-dimensional (1D) particle diffusion model that exhibits anomalous diffusion is the Single-File diffusion model (as shown in Fig. 1.5). In this model, a sequence of particles is confined to a 1D channel, where each particle is free to diffuse without the influence of an external potential field, performing random walks to the left or right. However, the particles cannot pass each other, meaning that exclusion forces prevent them from swapping positions or overlapping during movement. Consequently, the movement of any given particle is constrained by its neighbors, differing from the traditional Brownian motion or normal diffusion, where each particle moves independently without exclusion forces.

For the Single-File Diffusion model, the anomalous diffusion exponent α is typically $1/2$, which means that the mean square displacement MSD $\propto t^{1/2}$. This reflects a diffusion speed that is slower than that of normal diffusion. The reason for this anomalous diffusion behavior can be understood through the constrained dynamics of the particles. Since the particles cannot cross each other, their movement is strongly influenced by the motion of the adjacent particles. As such, even though all particles engage in unbiased random walks, their effective diffusion

distance is reduced due to the confinement, leading to subdiffusive behavior.

The Single-File Diffusion model serves not only as a tool to understand anomalous diffusive behavior but also to describe particle diffusion in practical problems, such as ion transport in proteins and pores [30,31], and molecular diffusion in nanotubes [32]. The model is particularly useful in explaining diffusion constraints within material and biological systems on a microscopic scale.
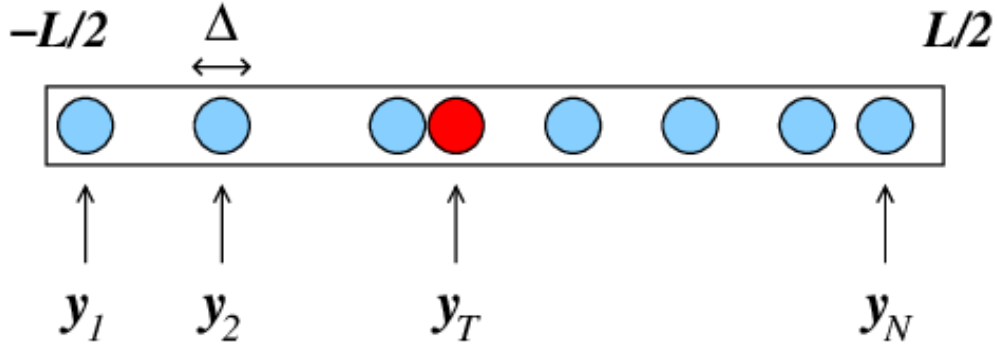
Figure 1.5: A typical Single-File diffusion model [33]. Diffusing particles in a one-dimensional channel where mutual passage is excluded, i.e $y_j \leq y_{j+1} - \Delta$ for $j = 1, \ldots, N-1$.

1.3.2   Classical models
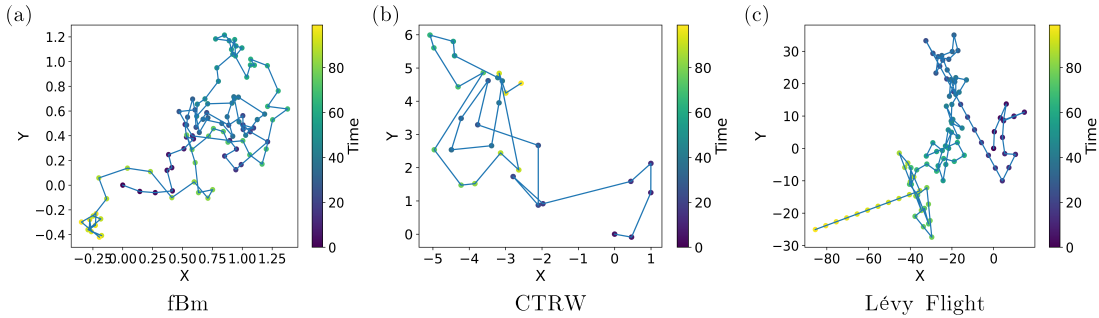
Figure 1.6: Comparison of the 2D trajectories of three classic random models over 100 time steps. The probability density of fractional Brownian motion (fBm) is Gaussian, but it can lead to anomalous diffusion. The continuous time random walk (CTRW) model consists of waiting times and jumping lengths of different distribution forms. In Lévy flights, the particle has finite velocity.

We list some classical models that can result in anomalous diffusion. The comparison between these models and the anomalous dynamics in disordered materials is discussed in Chapter 4.

- Fractional Brownian Motion (fBm): This model was first introduced by Kolmogorov in 1940 within the framework of Hilbert space [34]. Its probability density distribution function is Gaussian, but it can lead to anomalous diffusion. Fig. 1.6(a) presents a typical two-dimensional trajectory of fBm. fBm is a generalization of Brownian motion with long-range correlations, where the step sizes are positively (persistent) or negatively (anti-persistent) correlated with previous steps [35–38]. The stochastic integral expression of fBm $B_H(t)$ can be represented as follows:

$$
\begin{aligned}
B_H(t) = \frac{1}{\Gamma\left(H + \frac{1}{2}\right)} \Bigg(&\int_{-\infty}^{0} \left((t-s)^{H-\frac{1}{2}} - (-s)^{H-\frac{1}{2}} \right) \mathrm{d}B(s) \\
&+ \int_{0}^{t} (t-s)^{H-\frac{1}{2}} \, \mathrm{d}B(s) \Bigg)
\end{aligned}
\tag{1.4}
$$

  Here $B(t)$ represents Brownian motion, γ is the gamma function. H is the Hurst exponent, $H \in (0,1)$. fBm shows sub-diffusive behavior when $H < 1/2$, normal diffusion and super-diffusive behavior when $H = 1/2$ and $H > 1/2$, respectively.

- Continuous-Time Random Walk (CTRW): CTRW is a model that effectively describes the diffusion process of particles, which was introduced by Montroll and Weiss in 1965 [39]. They extended the concept of regular random walks on a lattice to a continuous time scale. This process exhibits jumps at random intervals, where the waiting times and jump lengths often follow heavy-tailed distributions, such as power-law distributions [40–44]. For a CTRW model characterized by different distributions of waiting times $\psi(t)$ and jump lengths $\omega(x)$, the model exhibits sub-diffusive behavior when $\psi(t)$ has a divergent first moment and $\omega(x)$ has a finite second moment. A typical CTRW particle diffusion trajectory is shown in Fig. 1.6(b), where it can clearly be seen that there are waiting times between each jump event.

- Lévy Flight: In this process, particles perform a random walk with step lengths drawn from a heavy-tailed distribution like the Lévy distribution, which has an infinite variance and mean that result in finite velocities of particles and super-diffusive behavior [45–47]. Fig. 1.6(c) exhibits a typical diffusion trajectory of particle in Lévy Flight model.

1.4   Organization of this thesis

The structure of this thesis follows the following arrangement:

In Chapter 1, two fundamental concepts are introduced that are central to the theme of this thesis: disordered materials and anomalous dynamics. These

basic concepts run throughout the entire thesis, serving as a foundation for the subsequent chapters.

In Chapter 2, the dynamic critical behavior of the two-dimensional and three-dimensional Ising model is studied in equilibrium state under Glauber dynamics. Unlike the previous research, we focus on the mean square deviation (MSD) of the magnetization M over time, as well as the autocorrelation function of M. We numerically verify and speculate novel dynamic exponents.

In Chapter 3, the structural dynamical properties of polycrystalline graphene is studied. The natural fluctuations of a sample of polycrystalline graphene are separated into the dynamical equivalences of the bulk modulus and shear modulus. The analysis of their MSDs is studied, and a relationship between their diffusion coefficients is established. The relationship between these diffusion coefficients and the response to external forces is constructed through the Einstein equation.

In Chapter 4, we similarly constructed structural quantities in amorphous silicon and studied their dynamical properties. We found that the MSD exhibits normal diffusion behavior in the early stage, while the quantities related to the shear modulus exhibit anomalous subdiffusive behavior over longer times: MSD $\sim t^a$ ($a < 1$). We compare the dynamical behavior with classic models describing anomalous diffusion, such as fractional Brownian motion (fBm) and continuous random time walks (CRTW). We find the velocity autocorrelation function to be negative, which is an essential difference with CRTW, but also holds for fBm.

In Chapter 5, the domain growth behavior in polycrystalline graphene is studied, which is an out-of-equilibrium process. We used a domain recognition algorithm to quantify the coarsening process. We also describe the crystal orientation distribution and defect density, as a function of time in the crystallization process of polycrystalline graphene. We also discuss the effects of a substrate on the domain growth.

Critical dynamical behavior of the Ising model

Abstract

We investigate the dynamical critical behavior of the two- and three-dimensional Ising model with Glauber dynamics in equilibrium. In contrast to the usual standing, we focus on the mean-squared deviation of the magnetization M, MSD_M, as a function of time, as well as on the autocorrelation function of M. These two functions are distinct but closely related. We find that MSD_M features a first crossover at time $\tau_1 \sim L^{z_1}$, from ordinary diffusion with $\mathrm{MSD}_M \sim t$, to anomalous diffusion with $\mathrm{MSD}_M \sim t^\alpha$. Purely on numerical grounds, we obtain the values $z_1 = 0.45(5)$ and $\alpha = 0.752(5)$ for the two-dimensional Ising ferromagnet. Related to this, the magnetization autocorrelation function crosses over from an exponential decay to a stretched-exponential decay. At later times, we find a second crossover at time $\tau_2 \sim L^{z_2}$. Here, MSD_M saturates to its late-time value $\sim L^{2+\gamma/\nu}$, while the autocorrelation function crosses over from stretched-exponential decay to simple exponential one. We also confirm numerically the value $z_2 = 2.1665(12)$, earlier reported as the single dynamic exponent. Continuity of MSD_M requires that $\alpha(z_2 - z_1) = \gamma/\nu - z_1$. We speculate that $z_1 = 1/2$ and $\alpha = 3/4$, values that indeed lead to the expected $z_2 = 13/6$ result. A complementary analysis for the three-dimensional Ising model provides the estimates $z_1 = 1.35(2)$, $\alpha = 0.90(2)$, and $z_2 = 2.032(3)$. While z_2 has attracted significant attention in the literature, we argue that for all practical purposes z_1 is more important, as it determines the number of statistically independent measurements during a long simulation.

2.1   Introduction

Universality is a key concept in statistical physics [48]. Phenomena which at a first glance seem completely unrelated, such as the liquid-gas phase transition and the ferromagnetic-paramagnetic phase transition in magnetic materials, belong to the same universality class, sharing the same set of critical exponents and other renormalization-group invariants that characterize their equilibrium behavior around the critical point [49]. The Ising model [50], the simplest fruit-fly model in statistical physics which lends itself well for theory and simulation, is found to belong to the same universality class [51–53]. Studies of the critical equilibrium properties of the Ising model are therefore of direct experimental relevance [51].

The concepts of critical phenomena can fortunately be extended to dynamical processes – for a seminal review see Ref. [54]. However, while universality is well established for equilibrium properties, it is not clear in how far it also extends to dynamical properties [54–57]. As it is well-known, the onset of criticality is marked by a divergence of both the correlation length ξ and the correlation time τ. While the former divergence yields singularities in static quantities, the latter manifests itself notably as critical slowing down. To describe dynamical scaling properties, an additional exponent is required in addition to the static exponents. This so-called dynamic exponent z links the divergences of length and time scales, i.e., $\tau \sim \xi^z$ [58, 59]. In a finite system, ξ is bounded by the linear system size L, so that $\tau \sim L^z$ at the incipient critical point. The dynamic critical exponent z has been numerically computed to be $z = 2.1665(12)$ at two dimensions by Nightingale and Blöte [58]. Note the value $z = 2.0245(15)$ at three dimensions [59].

In the chapter we attempt to extend our knowledge in the field by highlighting an overlooked aspect of dynamic critical phenomena using single spin-flip (Glauber) dynamics on the two- and three-dimensional Ising ferromagnet. In contrast to the standard belief that the dynamical critical behavior is characterized by a single dynamic exponent z, we provide numerical evidence that there is another dynamic critical exponent, considerably smaller than the most studied one, which appears to be of greater practical relevance. In particular, we provide a more refined description of the magnetization autocorrelation function featuring three regimes that are separated by two crossover times, namely $\tau_1 \sim L^{z_1}$ and $\tau_2 \sim L^{z_2}$, where z_1 is a newly identified dynamic exponent and z_2 the already well-known exponent [56–59].

The rest of the chapter is laid out as follows: In Sec. 2.1 we introduce the model and outline the numerical details of our implementation. In Sec. 2.2 we introduce the key observables under study and elaborate on the analysis of the numerical data, placing our findings into context. Finally, in Sec. 2.3 we critically summarize the main outcomes of this work in the framework of the current literature and also set an outlook for future studies.

We consider the nearest-neighbor, zero-field Ising model with Hamiltonian

$$\mathcal{H} = -J \sum_{\langle i,j \rangle} \sigma_i \sigma_j, \tag{2.1}$$

where $J > 0$ indicates ferromagnetic interactions, $\sigma_i = \pm 1$ denotes the spin on lattice site i, and $\langle \ldots \rangle$ refers to summation over nearest neighbors only. Here, we study the two- and three-dimensional Ising model on the square $(L \times L)$ and simple cubic $(L \times L \times L)$ lattices respectively, employing periodic boundary conditions. Many equilibrium properties of these models are known, especially at two dimensions where exact results are available, such as the location of the critical temperature, i.e., $T_c = 2/\ln\left(1 + \sqrt{2}\right) = 2.269185\ldots$ [16]. For the three-dimensional model on the other hand, there is a wealth of high-accuracy estimates of critical parameters from various approximation methods, see Ref. [60] and references therein. One such prominent example is the value of the critical point $T_c = 4.511523\ldots$, recently proposed in Ref. [61] via large-scale numerical simulations.

The Ising model is without doubt a prototypical model for studying dynamical properties. For this purpose, an elementary move is a proposed flip of a single spin at a random location, which is then accepted or rejected according to the Metropolis algorithm [18]. One unit of time then consists of $N = L^2$ elementary moves at two dimensions (similarly, $N = L^3$ at three dimensions). This dynamics is often referred to as Glauber dynamics [62–64], even though Glauber originally used a slightly different acceptance probability. Note that transition rates in Glauber dynamics are never higher, but always at least half of those of single spin-flip Metropolis dynamics, so that all dynamic exponents are shared. Other commonly used dynamical algorithms in the extensive literature are the spin-exchange (Kawasaki) dynamics [65–67], as well as numerous types of cluster algorithms [68–70]. Yet, these are outside the scope of the current work.

On the technical side, our numerical simulations of the Ising model were performed at the critical temperature [16, 61] using single spin-flip dynamics and systems with linear sizes within the range $L = \{16 - 96\}$ at two dimensions (accordingly, $L \in \{10 - 40\}$ at three dimensions). We note that the simulation time needed for a single realization on a node of a *Dual Intel Xeon E5-2690 V4* processor was 1 hour for $L = 96$ at two dimensions. The analogous CPU time was 35 minutes for $L = 40$ at three dimensions. For each system size L, $10^4 - 10^5$ independent realizations have been generated at both dimensions.

2.2 Results and Analysis
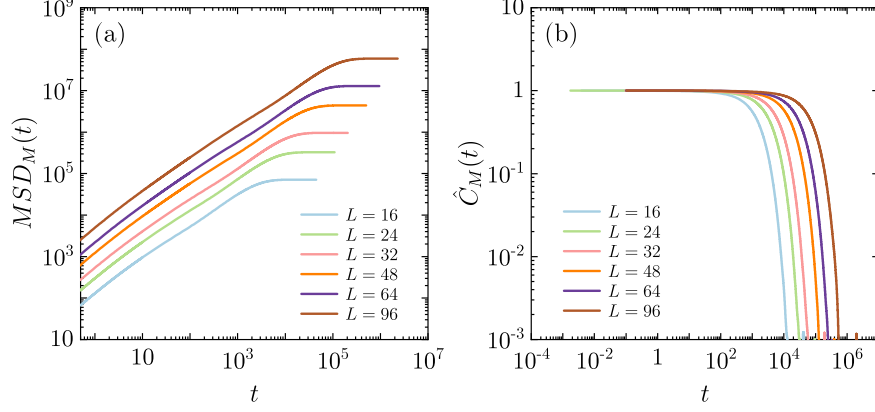
Figure 2.1: (a) Mean-square displacement of the magnetization $\langle \Delta M^2(t) \rangle$ vs. time t. (b) The normalized autocorrelation $\hat{C}_M(t) = \langle M(t)M(0) \rangle / \langle M^2(0) \rangle$ as a function of t. Results for the two-dimensional Ising model.
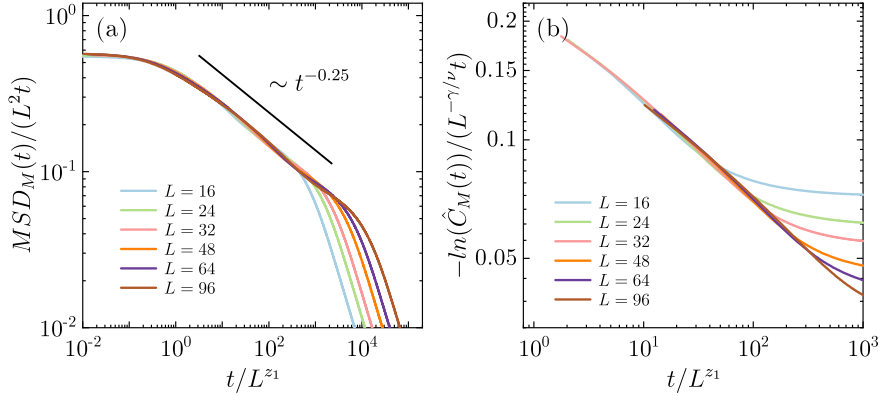
Figure 2.2: (a) Data collapse of $\mathrm{MSD}_M(t)$ curves over various system sizes around the first crossover L^{z_1}, with a scaling form of $\mathrm{MSD}_M(t)/(L^2 t) \sim t/L^{z_1}$, where z_1 is 0.45 ± 0.05. $\mathrm{MSD}_M(t)$ turns over from the normal diffusion ($\sim L^2 t$) to anomalous diffusion ($\sim L^{2+z_1-\alpha z_1} t^\alpha$) at $t = L^{z_1}$. (b) Data collapse for $-\ln(\hat{C}_M(t))$ over various L around $t = L^{z_1}$ with a scaling factor $L^{-\gamma/\nu}$ (note that $\gamma/\nu = 1.75$ for the two-dimensional Ising model). $\hat{C}_M(t)$ shifts from exponential to stretched exponential around $t = L^{z_1}$. Results for the two-dimensional Ising model.

The two key observables that allow us to elaborate on some new aspects of the dynamical behavior of the Ising ferromagnet are based on the order parameter (magnetization) of the system

$$M = \sum_i \sigma_i. \tag{2.2}$$

The first is the mean-squared deviation of the magnetization

$$\text{MSD}_M(t) = \langle (\Delta M(t))^2 \rangle = \langle (M(t) - M(0))^2 \rangle, \tag{2.3}$$

and the second the magnetization's autocorrelation function, defined as

$$C_M(t) = \langle M(t) \cdot M(0) \rangle. \tag{2.4}$$

We start the presentation with the two-dimensional Ising model and the raw numerical data, as shown in Fig. 2.1. In particular Fig. 2.1(a) depicts the $\text{MSD}_M(t)$, whereas Fig. 2.1(b) the normalized autocorrelation $\hat{C}_M(t) = \langle M(t)M(0) \rangle / \langle M^2(0) \rangle$, both as a function of time. Three distinct regimes can be identified, separated by two crossover correlation times, τ_1 and τ_2.

At short times t, the dynamics consist of $L^2 t$ proposed spin flips at spatially separated locations, of which a fraction $f \approx 0.14$ is accepted, as determined numerically. The dynamics thus involve $fL^2 t$ uncorrelated changes of $\Delta M = \pm 2$. Consequently, MSD_M in the short-time regime is given by

$$\text{MSD}_M = 4fL^2 t \quad (t \ll \tau_1). \tag{2.5}$$

At these short times, the magnetization does not have enough time to change significantly. Hence, it stays close to its value at $t = 0$. The expectation of the squared magnetization is related to the magnetic susceptibility [52]

$$\chi = \frac{\beta}{L^2} \langle M^2 \rangle. \tag{2.6}$$

Thus, in the short-time regime,

$$C_M(t) \approx k_b T L^2 \chi \sim L^{2+\gamma/\nu} \quad (t \ll \tau_1). \tag{2.7}$$

Here, we used the equilibrium property $\chi \sim L^{\gamma/\nu}$.

On the other hand, at very long times the two values of the magnetization are uncorrelated so that $\langle M(t) \cdot M(0) \rangle$ is small as compared to $\langle M^2 \rangle$. Hence we can derive that MSD_M saturates as follows

$$\begin{aligned}
\text{MSD}_M(t) &= \langle M(t)^2 + M(0)^2 - 2M(t)M(0) \rangle \\
&\approx 2\langle M^2 \rangle \approx 2k_b T L^2 \chi.
\end{aligned} \tag{2.8}$$
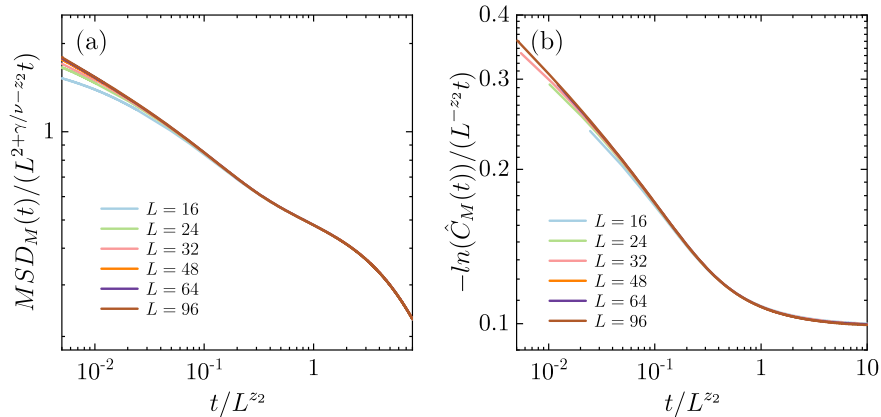
Figure 2.3:   (a) Data collapse of $\mathrm{MSD}_M(t)$ curves at the second crossover $t \approx L^{z_2}$, with a scaling form of $\mathrm{MSD}_M(t)/(L^\lambda t) \sim t/L^{z_2}$, the numerically found λ and z_2 are $2 + \gamma/\nu - z_2$ and 2.1667, respectively. $\mathrm{MSD}_M(t)(t)$ gradually transforms to saturation ($\sim L^{2+\gamma/\nu}$) from the anomalous diffusion ($\sim L^{2+z_1-\alpha z_1} t^\alpha$). (b) Data collapse for $-\ln\left(\hat{C}_M(t)\right)$ around $t = L^{z_2}$, where the scaling factor L^{-z_2} leads to an excellent collapse. $\hat{C}_M(t)$ is expected to turn over from stretched exponential to exponential around $t = L^{z_2}$. Results for the two-dimensional Ising model.
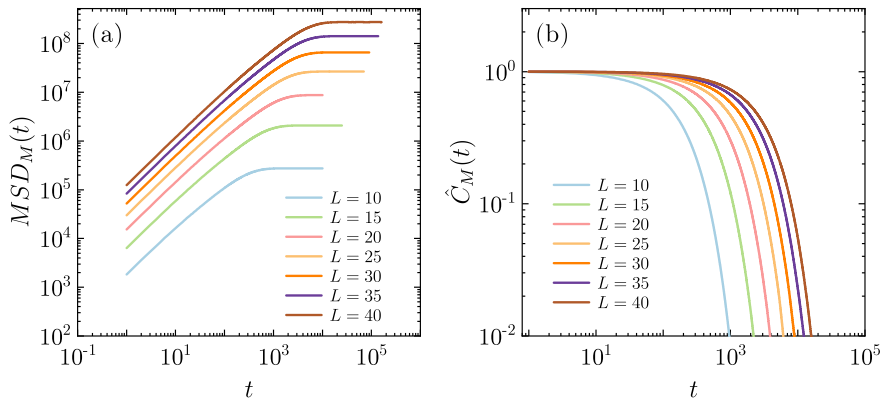
Figure 2.4:   Similar to Fig. 2.1 but for the three-dimensional Ising model.

Rather than an operational procedure, the dynamics can also be formulated as the application of the transition matrix $\mathcal{A}$ to a state vector $\vec{S}$. This is a rather unpractical formulation as $\mathcal{A}$ is a sparse matrix of size $2^{L^2} \times 2^{L^2}$, but nevertheless useful for the sake of argument. This transition matrix has an eigenvalue of $e_0 = 1$, with an eigenvector in which each element lies the likelihood of that state (the Boltzmann distribution). It also has a second-highest eigenvalue $e_1 \approx 1$, which determines the ultimate exponential decay of the autocorrelation. At long times t, the dynamical matrix is applied tL^2 times. Thus, expressed in A the

dynamics can be written as

$$C_M(t) = \langle \vec{S}_t \mathcal{A}^{tL^2} \vec{S}_0 \rangle. \tag{2.9}$$

For long times, the decay of the autocorrelation function is dominated by the largest non-zero eigenvector and eigenvalue

$$C_M(t) \sim e_1^{tL^2} \sim \exp\left[-t/\tau_2\right], \tag{2.10}$$

in which $\tau_2 = -L^2 \ln(e_1)$. It is very hard to obtain τ_2 via e_1 numerically unless L is a very small number, but this provides a valid argument to show that the magnetization autocorrelation function will decay exponentially at long times for finite L. Let us point out here that at times between τ_1 and τ_2 many modes contribute and the sum of their exponential is well-approximated by the stretched-exponential function.

As it is natural, the intermediate regime has to connect the short- and long-time regimes monotonically. The numerical data suggest that this happens via anomalous diffusion, i.e., $\mathrm{MSD}_M \sim t^\alpha$, whereas the autocorrelation function seems to decay as a stretched-exponential with the same anomalous exponent α.

Clearly, the key quantities that we want to establish in this manuscript are the dynamic exponents z_1 and z_2, as well as the anomalous exponent α. To this end, we use the method of finite-size scaling [51–53]. Figure 2.2 embodies the collapse of $\mathrm{MSD}_M(t)$ curves for the wide range of system sizes studied around the first transition point, obtained for $z_1 = 0.45 \pm 0.05$. At the intermediate regime of this plot, the curve is expected to decay as $\sim t^{\alpha-1}$. Numerically, we estimate the anomalous exponent to be $\alpha = 0.752 \pm 0.005$. Figure 2.3 now illustrates an analogous collapse of the curves for around the second transition point. This is attained by plotting $-\ln(C_M(t)/C_M(0))/(L^{-z_2}t)$ as a function of t/L^{z_2}, where $z_2 = 2.1665$ is set equal to the value for z as reported by Nightingale and Blöte [58].

The intermediate regime for MSD_M starts at time $\tau_1 \sim L^{z_1}$ at a value of $\langle (\Delta M)^2 \rangle \sim L^{2+z_1}$, then increases following a power-law mode with an exponent α, until it reaches its saturation value $\sim L^{2+\gamma/\nu}$ at time $\tau_2 \sim L^{z_2}$. Assuming a single power-law function in the intermediate regime, the anomalous exponent is expected to be

$$\alpha = (\gamma/\nu - z_1)/(z_2 - z_1). \tag{2.11}$$

Purely based on numerical findings, we speculate that $z_1 = 1/2$ and $\alpha = 3/4$; in that case, we obtain from Eq. (2.11) that $z_2 = 13/6 = 2.1667$ in excellent agreement with the most accurate numerical estimates [58].

To further corroborate on the main aftermath of our work, we undertook a parallel examination of the three-dimensional Ising ferromagnet. Analogously to the analysis sketched above for the two-dimensional Ising model, we obtained data collapses around the first and second crossover times. Figures 2.4 - 2.6 below

summarize our main findings: Fig. 2.4 exhibits the raw data, Fig. 2.5 suggests that $\mathrm{MSD}_M(t)/(L^3 t)$ is a function of t/L^{z_1} with $z_1 = 1.35 \pm 0.02$, and Fig.2.6 that $-\ln(\hat{C}_M(t))/(L^{-z_2} t)$ is a function of t/L^{z_2} with $z_2 = 2.032 \pm 0.003$. Thus, as in two dimensions, the dynamical critical behavior features two crossover times characterized by two dynamic critical exponents. Additionally, the exponent of the intermediate anomalous diffusion α for the three-dimensional Ising ferromagnet is numerically found to be 0.90 ± 0.02. An overview of critical exponents reported in this manuscript is given in Tab. 2.1.

Table 2.1: A summary of critical exponents as reported in this manuscript for the two-dimensional (2D) and three-dimensional (3D) Ising ferromagnet. The last two columns refer to exact [51] or high-precision [60] estimates of the critical exponents γ and ν that have been used in the data collapse.

	z_1	z_2	α	γ	ν
2D	0.45(5)	2.1665(12)	0.752(5)	7/4	1
3D	1.35(2)	2.032(3)	0.90(2)	1.237075(10)	0.629971(4)
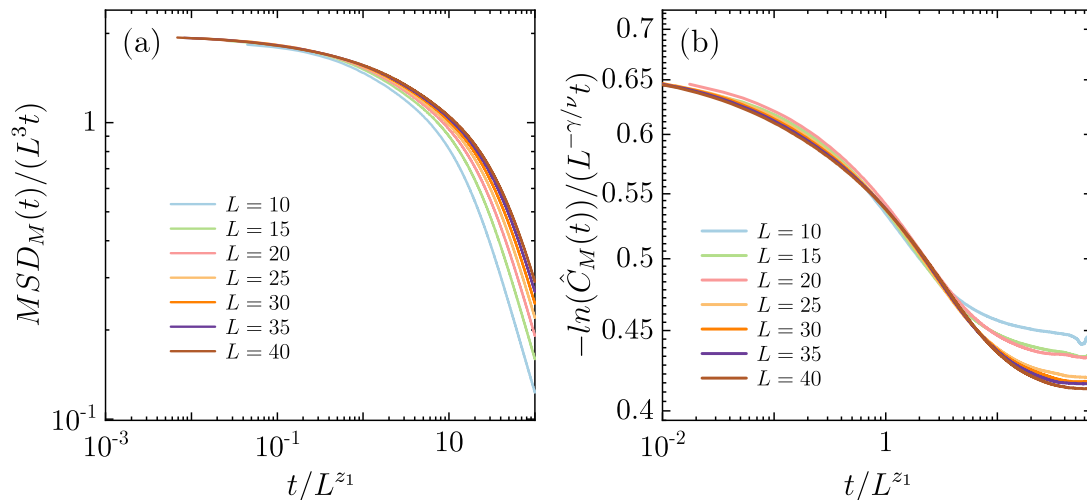
Figure 2.5: Data collapse around the first crossover for the three-dimensional Ising model. (a) $\mathrm{MSD}_M(t)$ collapse over various L, with a scaling form of $\mathrm{MSD}_M(t)/(L^3 t) \sim t/L^{z_1}$, where the numerically found estimate for z_1 is 1.35 ± 0.02. $\mathrm{MSD}_M(t)$ turns over from normal diffusion ($\sim L^3 t$) to anomalous diffusion ($\sim L^{3+z_1-\alpha z_1} t^\alpha$) at $t = L^{z_1}$. (b) $-\ln(\hat{C}_M(t))$ collapse around $t = L^{z_1}$ with a scaling factor $L^{-\gamma/\nu}$ (note that $\gamma/\nu = 1.9637$ in the three-dimensional Ising universality class [53]). $\hat{C}_M(t)$ shifts from exponential to stretched exponential around $t = L^{z_1}$.
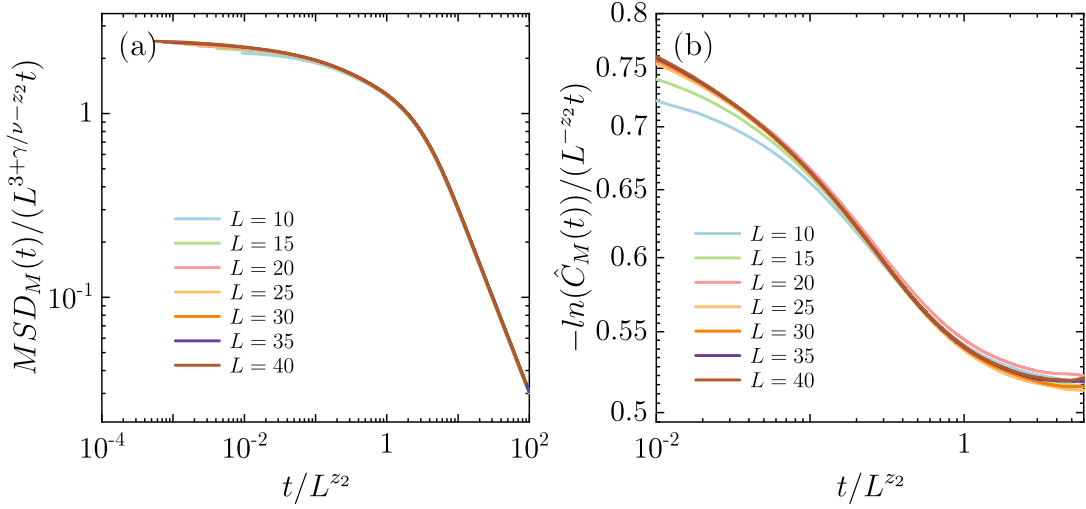
Figure 2.6:   Data collapse around the second crossover for the three-dimensional Ising model.   (a) $\mathrm{MSD}_M(t)$ collapse at $t \approx L^{z_2}$, with a scaling form of $MSD_M(t)/(L^\lambda t) \sim t/L^{z_2}$, the numerically found λ and z_2 are $3 + \gamma/\nu - z_2$ and 2.032 ± 0.003, respectively. $\mathrm{MSD}_M(t)$ gradually transforms to saturation ($\sim L^{3+\gamma/\nu}$) from the anomalous diffusion ($\sim L^{3+z_1-\alpha z_1}t^\alpha$). (b) Data collapse for $-\ln(\hat{C}_M(t))$ around $t = L^{z_2}$, where the scaling factor L^{-z_2} leads to excellent collapse. $\hat{C}_M(t)$ is expected to turn over from stretched exponential to exponential around $t = L^{z_2}$.

2.3   Summary and outlook

We analyzed the results of extensive simulations of the two- and three-dimensional Ising model with Glauber dynamics. In particular, we scrutinized the mean-squared deviation and autocorrelation function of the magnetization, showcasing the existence of three dynamical regimes, separated by two crossover times at $\tau_1 \sim L^{z_1}$ and $\tau_2 \sim L^{z_2}$. In the short-time regime, the mean-squared deviation of the magnetization shows ordinary diffusive behavior and the autocorrelation function exponential decay. In the second intermediate regime the mean-squared deviation is characterized by anomalous diffusive behavior and the autocorrelation function decays as a stretched-exponential way. Finally, in the third late-time regime the mean-squared deviation saturates at a constant value while the autocorrelation function again decays exponentially.

The second crossover to the exponential decay of the autocorrelation function has been extensively studied in the literature. Nightingale and Blöte reported that this exponential decay sets in at a time determined by the dynamic critical exponent $z = 2.1665(12)$ [58]; this is in agreement with our estimate z_2 at the second crossover. To the best of our knowledge, the first crossover has not yet been reported or was assumed to occur at some fixed time (i.e., $z_1 = 0$) without

substantiation. The simulations and analysis captured here clearly manifest the existence of this first crossover at a time governed by a new dynamic critical exponent z_1. We should stress here that earlier work on non-equilibrium dynamics has also suggested the presence of a new exponent θ [71] akin to the newly introduced exponent z_1 of the present work. The authors of Ref. [71] considered a quench from a high temperature configuration with an initial magnetization $M(0)$ to the critical temperature T_{c}; the exponent θ was introduced to describe the behavior in the critical initial slip.

We also postulated a speculative argument about the crossover times at two dimensions. Purely on numerical grounds, we suspect the first crossover to correspond to a dynamic exponent $z_1 = 1/2$, and the exponent of the anomalous diffusion to be $\alpha = 3/4$. In this case, we showed that the second crossover is governed by the exponent $z_2 = 13/6$, in full agreement with the numerical result $z = 2.1665(12)$. At this stage, the development of a solid theoretical argument supporting the presence of the numerically observed first crossover and the relevant dynamic and anomalous diffusion exponent z_1 and α respectively is called for.

To sum up, we hope that the relevance of our work will be twofold: (i) On the practical side, for obtaining statistically uncorrelated samples the proper sampling frequency should be set by the newly reported exponent z_1: the correlation between consecutive samples which are separated by (multiples of) $\tau_1 \sim L^{z_1}$ has decayed in a stretched-exponential way to a value which is as small as one would want. Hence, for obtaining statistically uncorrelated samples it is not necessary to sample with an interval scaling as τ_2. (ii) On the theoretical side, the critical dynamical behavior of the Ising model with Glauber dynamics is much richer than reported till date featuring two distinct crossovers. Thus, if dynamic universality exists, it must also be much more substantial and needs further investigation.

Closing, we would like to raise some motivational comments for future work. In a recent paper [72] it was shown that the ϕ^4 model with local dynamics appears to belong to the same dynamic universality class as the Ising model; this was done by probing numerically the dynamic critical exponent which was found to be $z = 2.17(3)$. If indeed this is the case, then also the exponent z_1 should apply to the ϕ^4 model; see also Refs. [73–75] for extensive aspects on the dynamic Ising universality. Furthermore, in Ref. [76] the Ising model with Kawasaki dynamics was studied and the authors reported that the Fourier modes of the magnetization are in very close agreement with the dynamical eigenmodes, suggesting that $z = 4 - \eta = 15/4$. Investigating this aspect under the prism of the newly introduced exponent z_1 might be another intriguing continuation of our work [77]. We plan to pursue these and other relevant open questions in the near future.

Structural dynamics of polycrystalline graphene

Abstract

The exceptional properties of the two-dimensional material graphene make it attractive for multiple functional applications, whose large-area samples are typically polycrystalline. Here, we study the mechanical properties of graphene in computer simulations and connect these to the experimentally relevant mechanical properties. In particular, we study the fluctuations in the lateral dimensions of the periodic simulation cell. We show that over short time scales, both the area A and the aspect ratio B of the rectangular periodic box show diffusive behavior under zero external field during dynamical evolution, with diffusion coefficients D_A and D_B that are related to each other. At longer times, fluctuations in A are bounded, while those in B are not. This makes the direct determination of D_B much more accurate, from which D_A can then be derived indirectly. We then show that the dynamic behavior of polycrystalline graphene under external forces can also be derived from D_A and D_B via the Nernst-Einstein relation. Additionally, we study how the diffusion coefficients depend on structural properties of the polycrystalline graphene, in particular, the density of defects.

3.1 Introduction

Graphite is a material in which layers of carbon atoms are stacked relatively loosely on top of each other. Each layer consists of carbon atoms, arranged in a honeycomb lattice. A single such layer is called graphene. This material has many exotic properties, both mechanical and electronic. Experimentally produced samples of graphene are usually polycrystalline, containing many intrinsic [8, 78, 79], as well as extrinsic [80] lattice defects. Unsaturated carbon bonds are energetically very costly [81–85], and therefore extremely rare in the bulk of the material. Polycrystalline graphene samples are therefore almost exclusively three-fold coordinated, and well described by a continuous random network (CRN) model [86], introduced by Zachariasen almost 90 years ago.

Polycrystalline graphene is continuously evolving in time, from one CRN-like state to another. A mechanism by which such a topological change can happen, was introduced by Wooten, Winer, and Weaire (WWW) in the context of the the simulation of samples of amorphous Si and Ge. This so-called WWW algorithm became the standard modeling approach for the dynamics of these kind of models [87, 88].

In the WWW approach, a configuration C_i consists of a list of the coordinates of all N atoms, coupled with an explicit list of the bonds between them. From this configuration C_i, a trial configuration C_i' is produced via a *bond transposition*: a sequence of carbon atoms $\{i, j, k, l\}$ is selected, connected with explicit bonds i-j, j-k and k-l. The first and last of these bonds are then replaced by bonds i-k and j-l, while bond j-k is preserved. After this change in topology, the atoms are allowed to relax their positions. This simulation approach requires a potential that uses the explicit list of bonds, for instance the Keating potential [89] for amorphous silicon. The resulting configuration is then called the trial configuration C_i'. The proposed change to this trial configuration is either accepted, i.e. $C_{i+1} = C_i'$, or rejected, i.e. $C_{i+1} = C_i$. The acceptance probability is determined by the energy difference via the Metropolis criterion:

$$P = \min\{1, \exp(-\beta \Delta E)\}, \tag{3.1}$$

where $\beta = (k_B T)^{-1}$, with Boltzmann constant k_B and temperature T, and $\Delta E = E(C') - E(C)$ is the change in energy due to the bond transposition. In this way, the simulation produces a Markov chain $C_0 \ldots C_M$, satisfying detailed balance.

The properties of polycrystalline graphene sheets have been a topic of intense research already for some time [90–94]. More recently, Ma *et al.* reported that the thermal conductivity of polycrystalline graphene films dramatically decreases with decreasing grain size [95]. The work of Gao *et al.* shows that the existence of single-vacancy point defect can reduce the thermal conductivities of graphene [96]. Wu *et al.* reported the magnetotransport properties of zigzag-edged graphene nanoribbons on an *h*-BN substrate [97]. Additionally, strain

effects on the transport properties of triangular and hexagonal graphene flakes were studied in the work of Torres *et al.* [98].

This chapter reports on the dynamical properties of polycrystalline graphene. In particular, we study two geometric quantities that are readily accessible in computer simulations without having a clear experimental counterpart. In our simulations, the $L_x \times L_y$ graphene sample is rectangular, with periodic boundary conditions in the x- and y-directions; the quantities of interest are the area $A = L_x L_y$ and the aspect ratio $B = L_x/L_y$, and their mean square displacements (MSDs) under simulations in which the dynamics is the WWW algorithm. The results show that in the absence of external forces, MSD_A and MSD_B initially both increase linearly in time. At longer times, MSD_A saturates due to geometric limitations, while MSD_B keeps increasing linearly at all times. We measure the diffusion coefficients D_A and D_B, and demonstrate that the two are related.

We then continue to show that D_A and D_B govern the response of the sample to stretching and shear forces respectively, following the Nernst-Einstein relation.

The main relevance of the research presented here lies in establishing the relation between observables that are readily accessible in simulations but without a clear experimental counterpart (A and B and their dynamics), and mechanical properties of real-life graphene (e.g. response to external stretching and shear forces). Additionally, we demonstrate a clear relation between MSD_A and MSD_B, thereby also relating the bulk- and the shear-properties. Thus far, much less is known about this shape fluctuation-driven diffusive behavior; our work provides insight into the dynamics and mechanics of polycrystalline graphene.

3.2   The model

For simulating graphene, we use a recently developed effective semiempirical elastic potential [99]:

$$E_0 = \frac{3}{16}\frac{\alpha}{d^2}\sum_{i,j}(r_{ij}^2 - d^2)^2 + \frac{3}{8}\beta d^2 \sum_{j,i,k}\left(\theta_{jik} - \frac{2\pi}{3}\right)^2 + \gamma\sum_{i,jkl}r_{i,jkl}^2. \qquad (3.2)$$

Here, r_{ij} is the distance between two bonded atoms, θ_{jik} is the angle between the two bonds connecting atom i to atoms j and k, and $r_{i,jkl}$ is the distance between atom i and the plane through the three atoms j, k and l connected to atom i. The parameter $\alpha = 26.060$ eV/Å^2 controls bond-stretching and is fitted to the bulk modulus, $\beta = 5.511$ eV/Å^2 controls bond-shearing and is fitted to the shear modulus, $\gamma = 0.517$ eV/Å^2 describes the stability of the graphene sheet against buckling, and $d = 1.420$ Å is the ideal bond length for graphene. The parameters in the potential (3.2) are obtained by fitting to DFT calculations [99].

This potential has been used for the study of various mechanical properties of single-layer graphene, such as the vibrational density of states of defected and

polycrystalline graphene [100] as well as of various types of carbon nanotubes [101], the structure of twisted and buckled bilayer graphene [102], the shape of nanobubbles trapped under a layer of graphene [103], and the discontinuous evolution of defected graphene under stretching [104].

The initial polycrystalline graphene samples are generated as in [105]. Here, $N/2$ random points are placed in a square simulation box with periodic boundary conditions, and the Voronoi diagram is generated: around each random point, its Voronoi cell is the region in which this random point is nearer than any other random point. We then translate the boundaries between neighboring Voronoi cells into bonds, and the locations where three boundaries meet into atomic positions. In this way, we have created a three-fold coordinated CRN which is homogeneous and isotropic (i.e. does not have preferred directions). It is, however, an energetically unfavorable configuration; therefore, we then evolve the sample using the improved bond-switching WWW algorithm to relax it, while preserving crystalline density.

Up to this point, the sample is completely planar (i.e., all z-coordinates are zero). After some initial relaxation, we then assign small random numbers to the z-coordinates followed by energy minimization, which results in a buckled configuration. At this point, we also allow the box lengths L_x and L_y to relax. We do not relax the box lengths already in poorly relaxed samples, because then the sheet tends to develop all kinds of unphysical structures.

In our implementation, we use the fast inertial relaxation engine algorithm (FIRE) for local energy minimization [106]; the values of the parameters in this algorithm ($N_{\min}$, f_{inc}, f_{dec}, α_{start} and f_α) are taken as suggested in Ref. [107]. Figure 3.1 presents an initial polycrystalline graphene sample with periodic boundary condition generated from a Voronoi diagram and evolved based on the WWW-algorithm.

3.3 Dynamics of fluctuations in sample shapes

The oblong polycrystalline graphene sheet in our simulations has lengths L_x and L_y in the x- and the y-directions respectively, as shown in Fig. 3.1. These are not fixed quantities, but they fluctuate when bond transpositions are made.

Given that the sample is essentially two-dimensional, throughout this chapter we consider two geometric quantities defined as follows:

$$A(t) = L_x(t)L_y(t) \quad \text{and} \quad B(t) = L_x(t)/L_y(t). \tag{3.3}$$

Physically, for a flat, rectangular and homogeneous isotropic sample, the stiffness matrix is reduced and the mechanical properties of system can be efficiently characterized by two independent in-plane modes due to orthorhombic symmetry, It is easiest to associate $A(t)$ and $B(t)$ to fluctuations in the sample shape in the "bulk" and the "shear" modes respectively at the macroscopic scale without these
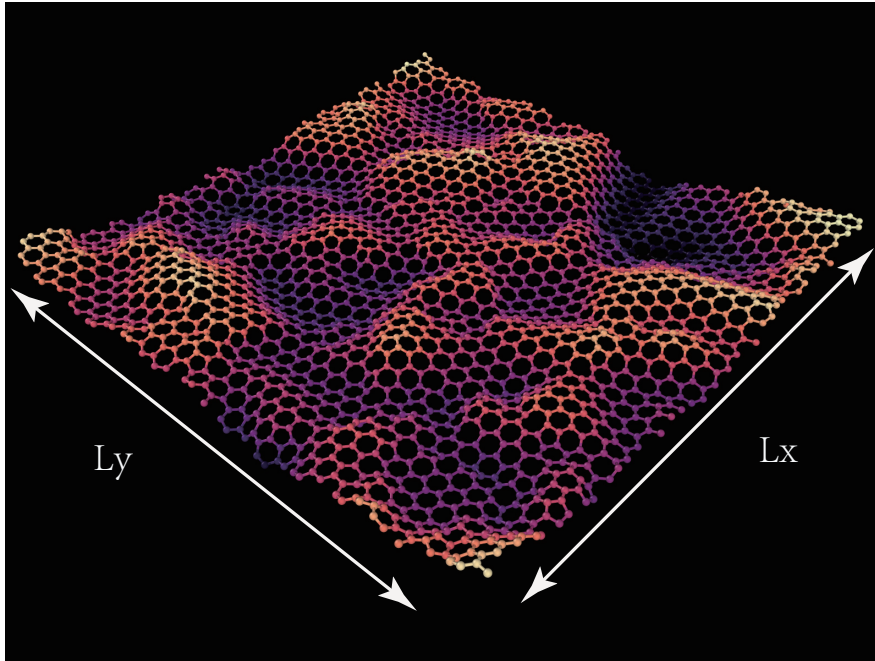
Figure 3.1: (color online) An initial buckled polycrystalline graphene sample with periodic boundary condition generated from a Voronoi diagram and evolved based on the WWW-algorithm. L_x and L_y represent the lateral dimensions of the sample.

symmetries breaking. We then track the dynamics of shape fluctuations of the sample in terms of their mean-square displacements $\text{MSD}_A(t) = \langle [A(t) - A(0)]^2 \rangle$ and $\text{MSD}_B(t) = \langle [B(t) - B(0)]^2 \rangle$, with the angular brackets denoting ensemble averages for a sample of fixed number of atoms and (more or less) constant density of defects. (We will soon see that the diffusion coefficients are functions of both these quantities.) Characteristic fluctuations in A and B for a sample with 1352 atoms are shown in Fig. 3.2 panel (a), and correspondingly, their MSDs are shown in panels (b) and (c). Therein we find that fluctuations in A are relatively much smaller in magnitude than those in B. Intuitively this makes sense, since relaxations through the shear mode is energetically much more favorable than through the bulk mode. This is also reflected in the MSDs. After a linear increase in time, MSD_A saturates at longer times, while MSD_B increases linearly at all times. From the data for MSD_A before it saturates, and MSD_B at all times, we identify the diffusion coefficients D_A and D_B, obtained from fitting the data to the relation given by

$$\text{MSD}(t) = 2Dt. \tag{3.4}$$
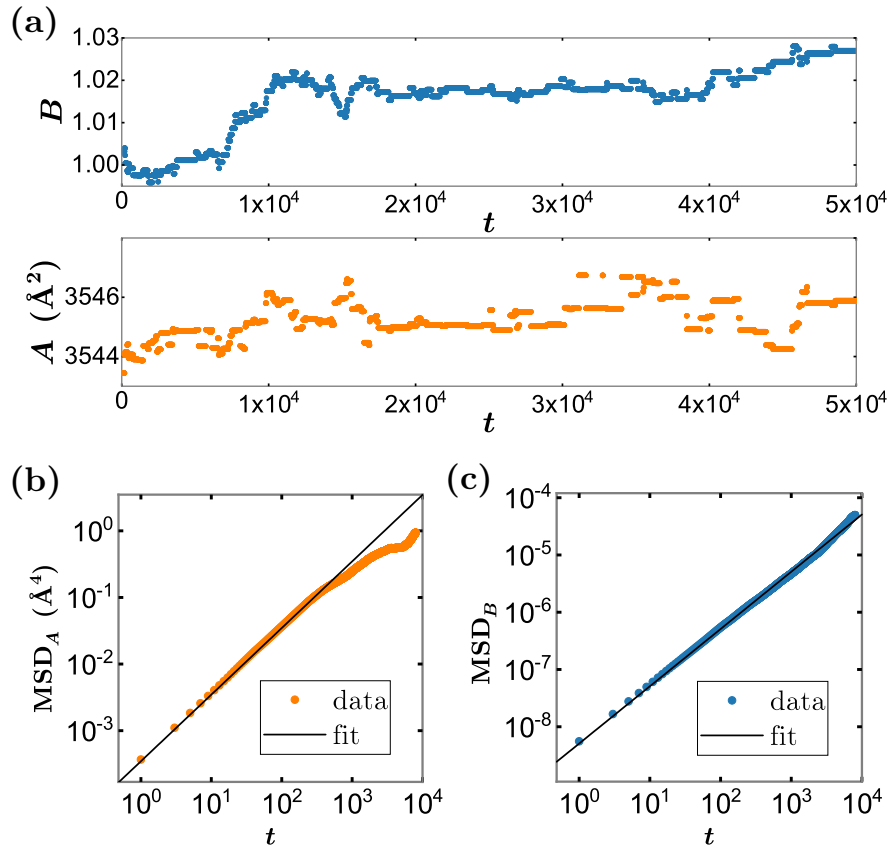
Figure 3.2: (color online) (a) Typical fluctuations in A and B in time for a sample with $N = 1352$; note that the range of fluctuations in B are considerably higher than in A. (b) $\mathrm{MSD}_A(t)$ and $\mathrm{MSD}_B(t)$ for this sample. The measured diffusion coefficients, as per Eq. (3.4) are $D_A \approx 1.737 \times 10^{-4}$ Å^4/[MC unit] and $D_B \approx 2.544 \times 10^{-9}$ [MC unit]$^{-1}$. See text for details.

Since time is measured in MC units (bond transposition moves are being attempted once per unit of MC time), and length is measured in Å, the units of D_A and D_B are Å^4/[MC unit] and [MC unit]$^{-1}$ respectively. Time all throughout the chapter is measured in MC units.

3.3.1 D_B increases linearly with defect density

An interesting question is what determines D_B for a sample with a given number of atoms N. As we expect D_B to be equal to zero for a perfect graphene sample, our first guess is that D_B might depend on the density of defects. In our computer simulations of perfectly three-fold coordinated networks, defects are topological, in particular rings which are not six-fold. A convenient measure of the defect density ρ is then obtained by the number of such rings per area. Note that rings are almost exclusively 5-, 6- and 7-fold in the well-relaxed samples as we studied.

Since 5- and 7-fold rings generally appear and disappear in pairs, one can expect that the ratio of N5/N7 (N represents the number of 5- for 7-fold rings) is close to unity.
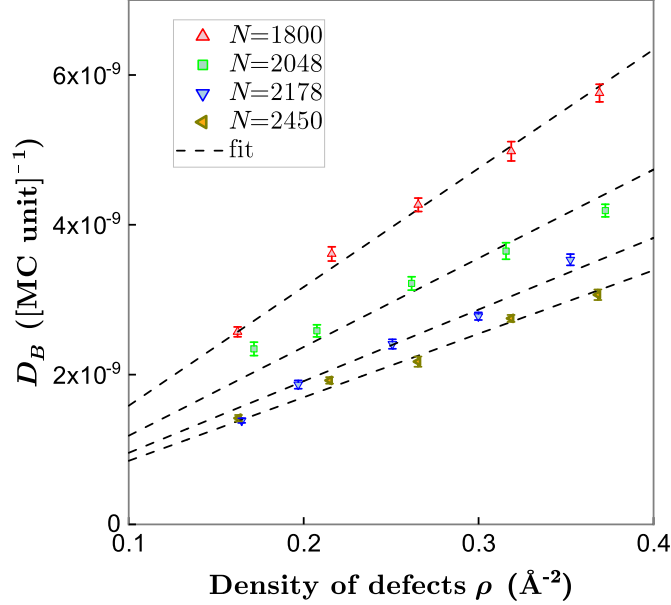
Figure 3.3: (color online) D_B plotted for four differently-sized samples, each with four different defect densities (points: simulation data, lines: best fit passing through origin). Error bars represent standard error of the mean, obtained from the ensemble of simulation runs. See text for details.

In order to test our intuition, we simulate graphene samples for four different atom numbers (around $N = 2000$), each with four different defect densities. The results are shown in Fig. 3.3. Points represent simulation data with statistical error bars, and dashes lines are best fit lines with each line passing through the origin (corresponding to $D_B = 0$ at $\rho = 0$). Even though there is no *a priori* reason for D_B to increase linearly with ρ for every value of N, Fig. 3.3 demonstrates that the linear scaling holds for the range of defect densities we simulated. Also clear is the decreasing trend in D_B with increasing N for a certain defect density. On a technical side, each point is obtained from averaging over 10 independent samples, and each sample is simulated 16 times over 30,000 attempted bond transpositions at a temperature of $kT = 0.25$ eV within each run. We perform further averaging over the initial time. The CPU time of a single attempted bond transposition is on average 0.76 s for samples (N=2000).

3.3.2   Relation between D_A and D_B

Further, since both A and B bear relations to L_x and L_y, one would expect them to be related through these length parameters, which we establish below. In order

to do so, having denoted the change in A and B over a small time interval dt for samples with dimensions L_x and L_y by dA and dB respectively, we express them in terms of small changes dL_x and dL_y as

$$
\begin{aligned}
\langle dA^2 \rangle &= \left\langle [L_y dL_x + L_x dL_y]^2 \right\rangle \quad \text{and} \\
\langle dB^2 \rangle &= \left\langle \frac{1}{L_y^4} [L_y dL_x - L_x dL_y]^2 \right\rangle .
\end{aligned}
\tag{3.5}
$$

Using $\langle dL_x dL_y \rangle = 0$ after an ensemble averaging, Eq. (3.5) leads to the simplified form

$$
\begin{aligned}
\langle dA^2 \rangle &= L_y^2 \langle dL_x^2 \rangle + L_x^2 \langle dL_y^2 \rangle \quad \text{and} \\
\langle dB^2 \rangle &= \frac{1}{L_y^4} \left[L_y^2 \langle dL_x^2 \rangle + L_x^2 \langle dL_y^2 \rangle \right] ,
\end{aligned}
\tag{3.6}
$$

i.e., $\langle dA^2 \rangle / \langle dB^2 \rangle = L_y^4$. If we extend this analysis to finite times, for which L_y does not appreciably change, then we expect the ratio D_A/D_B to behave $\sim L_y^4$.
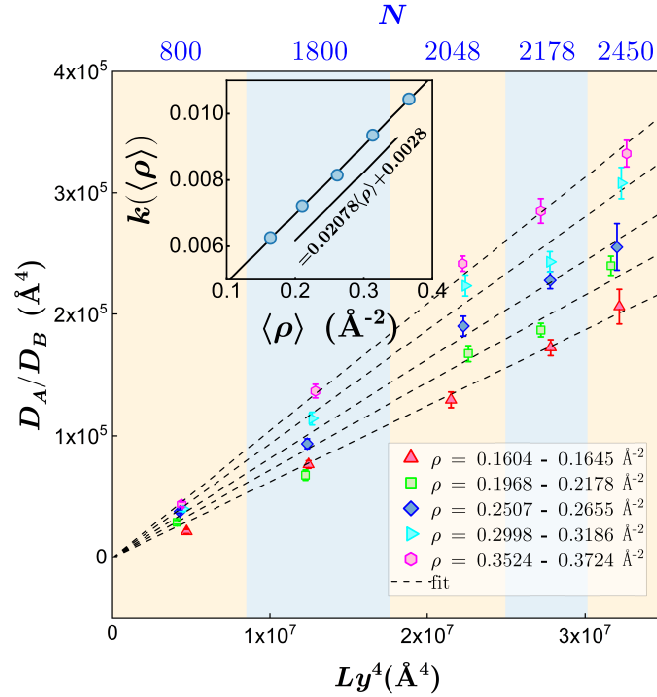
Figure 3.4: (color online) The ratio D_A/D_B vs L_y^4 for different N-values and defects densities [points: simulation data, lines: best-fit of the form $D_A/D_B = k(\langle \rho \rangle) L_y^4$]. Error bars represent standard error of the mean, obtained from the ensemble of simulation runs. The points located a color bar are measured with the same N. The inner plot shows that $k(\langle \rho \rangle)$ also bears a linear relation with $\langle \rho \rangle$ obtained from averaging in the ranges: $k(\langle \rho \rangle) = 0.02078\langle \rho \rangle + 0.0028$.

In Fig. 3.4 we plot D_A/D_B for N=800, 1800, 2048, 2178, 2450 and five different ranges with approximate defect densities. We indeed observe that $D_A/D_B \sim L_y^4$: once again, simulation data are shown as points, while the dashed lines are the best-fit $D_A/D_B = k(\rho) L_y^4$ lines through the data points. The k-values, summarized in Tab. 3.1, are plotted as an inset to Fig. 3.4. Here we determine k by using statistical quantity $\langle \rho \rangle$ obtained from averaging in the ranges, these $k(\langle \rho \rangle)$ vs $\langle \rho \rangle$ points also lie on a straight line, whose best-fit estimate is $k(\langle \rho \rangle) = 0.02078\langle \rho \rangle + 0.0028$.
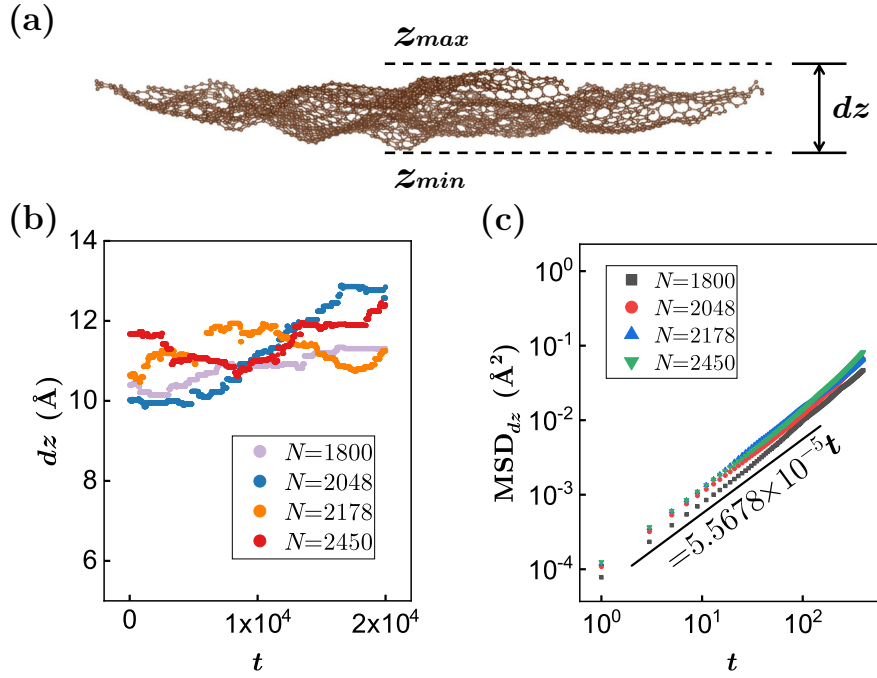
Figure 3.5: (color online) (a) A suspended graphene sample naturally tends to buckle, dz is the thickness of the sample. (b) The variation of dz for four differently-sized samples, the initial defects densities for all sample are fixed at around 0.15. (c) MSD_{dz} for these samples.

$\langle \rho \rangle$	$k(\langle \rho \rangle)$
0.16433	6.24×10^{-3}
0.21065	7.20×10^{-3}
0.26154	8.14×10^{-3}
0.31323	9.35×10^{-3}
0.36670	1.04×10^{-2}

Table 3.1: Values of k for different values of $\langle \rho \rangle$, corresponding to the best-fit $D_A/D_B = k(\langle \rho \rangle) L_y^4$ lines in Fig. 3.4.

N	$\langle L_{x,\text{initial}}\rangle(\text{Å})$	$\langle L_{y,\text{initial}}\rangle(\text{Å})$
800	45.35	45.72
1800	68.47	68.95
2048	73.91	72.58
2178	75.78	75.39
2450	80.15	80.38

Table 3.2: Dimensions of initial configurations obtained after optimization. Averaging for each N was done over 5 ($\langle\rho\rangle$ values listed in the table 3.1) $\times$ 10 (independent samples) $\times$ 16 (repetitions).

3.3.3   MSD in the z-direction

The graphene in our simulations is free-floating, and the presence of defects causes it to buckle, i.e., the carbon atoms show displacements in the out-of-plane direction. During bond transpositions, the buckling structure changes. To quantify the dynamics of buckling, we determine the minimal and maximal values of the z-coordinates of the atoms, and the difference $dz = z_{max} - z_{min}$; this is illustrated in the top panel of Fig. 3.5.

$$\text{MSD}_{dz}(t) = \langle [dz(t) - dz(0)]^2 \rangle. \tag{3.7}$$

Analogous to our analysis of the dynamics of $L_x(t)$ and $L_y(t)$, we then determine the MSD_{dz} of $dz(t)$. The results for various system sizes are shown in figure 3.5, in samples with a defect density around 0.15, simulated at a temperature of $kT = 0.25$ eV. Fig. 3.5(b) shows that the dz fluctuates around a level ≈ 11 Å, which is the typical equilibrium amplitude of the buckling for these samples; out-of-plane displacement-related studies can be found in our previous simulations [99]. Fig. 3.5(c) shows that the initial behavior is diffusive, with a diffusion coefficient that is insensitive to N.

3.3.4   Summary: defect density determines shape fluctuation dynamics

In summary so far, we have established that the density of defects determines D_B, and that the ratio $D_A/D_B = k(\langle\rho\rangle)L_y^4$ in Sec. 3.3.2. Putting these results together then implies that the density of defects is the sole determining factor for the dynamics of fluctuations in the sample shapes.

3.4   Sample response to external forces

That the fluctuations in quantity B lead to diffusive behavior without being limited by geometric constraints made us follow-up with the response of the samples

to externally applied forces. In particular, if we apply a (weak) force F_B to excite the shear mode, then we expect the (linear) response in terms of "mobility" μ_B in the relation $v_B = \mu_B F_B$ for the "deformation velocity v_B of the sample along the B-direction" to satisfy the Einstein relation

$$\mu_B = \frac{D_B}{k_B T}; \quad \text{i.e.,} \quad v_B = \frac{D_B}{k_B T} F_B, \tag{3.8}$$

where k_B is the Boltzmann constant and T is the temperature of the sample.

(a)

(b)

(c)

(d)
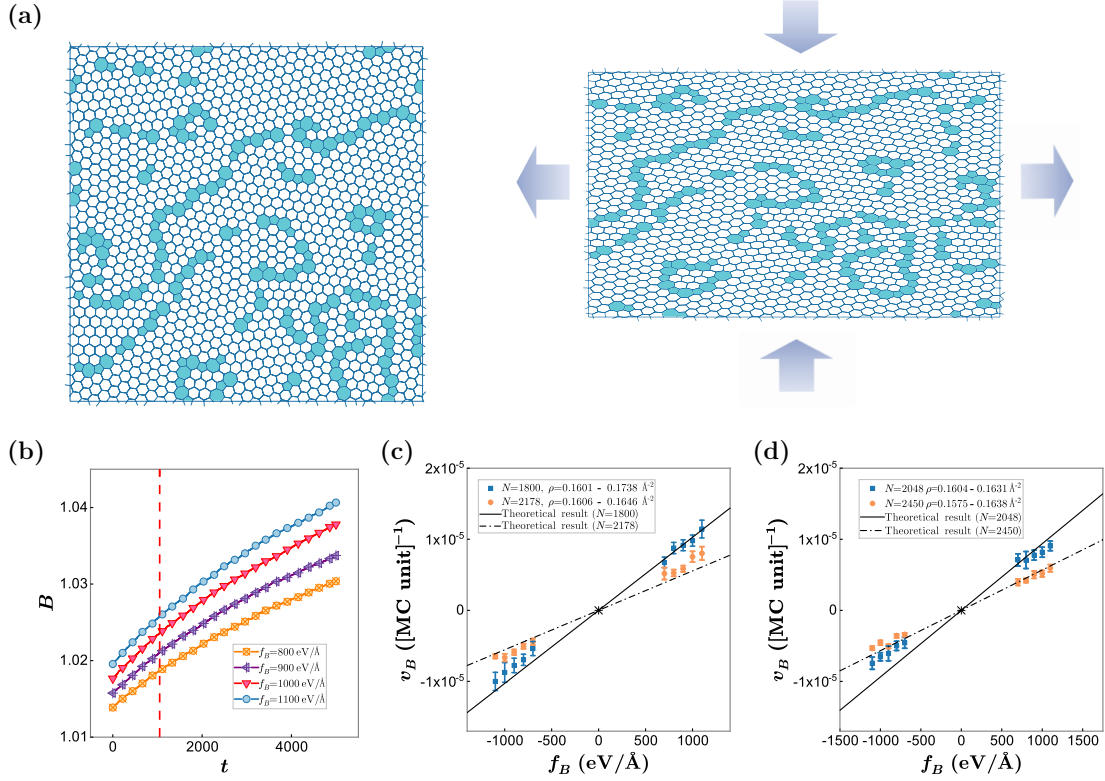
Figure 3.6: (color online) (a) A relaxed polycrystalline graphene sample. Elongated domains arise if the sample is stretched significantly within a short period of time. (b-c) v_B directly measured vs. predicted by the Nernst-Einstein relation (3.8). Error bars represent standard error of the mean, obtained from the ensemble of simulation runs. (d) Change in B in time when a constant stretching force is applied to the sample, restoring tendencies of elongated domains cause slower-than-linear increases at longer times ($t > 1000$).

In order to check for this relation in our simulations, we add an extra "force term" in the Hamiltonian in Eq. (3.2), to have the new Hamiltonian as

$$E = E_0 + c\frac{L_x}{L_y} \equiv E_0 + cB, \tag{3.9}$$

and calculate v_B in the following manner, for the applied force $F_B = \partial E/\partial B = c$.

The behavior of the aspect ratio B as a function of time, under a constant force f_B, is shown in figure 3.6(a), for forces $f_B = \pm 800, 900, 1000$ and 1100 eV/Å. The curves in this figure are obtained by averaging over 8 independent samples, each one simulated 32 times for each value of the force. At relatively short times, B increases linearly in time. Afterwards, the shear rate has a tendency to slow down. We speculate that this slowing down at longer times might be due to deformation of domains: Initially, these crystalline domains are isotropic, but after the sample has sheared over quite some distance, the domains become elongated. The tendency to restore isotropy makes the sample resist further deformation. This is illustrated in fig. 3.6(a). There is no a priori reason to assume that the increase in energy due to shearing is harmonic. In analogy to the quartic increase of the length of a circle under this type of deformation, we rather expect highly non-linear behavior. At short times, where the sample has not deformed significantly, the change in B as a response to the force f_B is expected to be given by the Nernst-Einstein equation Eq. (3.7). To test this, we obtained the short-time shear velocity v_B by fitting the slopes in figure 6a for the various forces. These measurements of v_B are plotted in figures 6b and 6c, as a function of f_B. Also plotted in figures 3.6(b) and 3.6(c) are the theoretical expectations as obtained from the Nernst-Einstein equation, in which we used the earlier obtained values for D_B. The figures 6b and 6c show agreement between the direct measurements of v_B and the theoretical expectations, indicating that with forces of these strengths the mechanical response is well-understood.

3.5 Conclusion

Computer simulations of materials at the atomistic level usually involve samples containing typically a few thousand atoms, with periodic boundary conditions. Quantities that can be easily and reliably measured in such simulations, are for instance the evolution in time of the lateral sizes of the periodic box, such as their fluctuations. In the simulations on graphene as presented here, the directly observable quantities are the lateral lengths L_x and L_y of the rectangular periodic box. The dynamics of L_x and L_y are coupled and can be better understood by considering the area $A = L_x L_y$ and aspect ratio $B = L_x/L_y$. Specifically, we concentrate on the mean-squared displacements of A and B. At short times, in which only a few atomic rearrangements occur, A and B show ordinary diffusive behavior, with diffusion coefficients D_A and D_B. We show that if the changes in L_x and L_y are uncorrelated, D_A and D_B can be obtained from each other. While this might not seem very surprising at first sight, it does connect the dynamics of shear mode and bulk mode — two quantities that are usually assumed to be uncorrelated — at short times.

At longer times, A and B show different behavior. Graphene has a char-

acteristic density, which translates directly into a preferred value for A around which it fluctuates. The amplitude of the fluctuations in A are determined by the bulk modulus, which is an equilibrium property and therefore computationally obtainable from simulations without realistic dynamics. The aspect ratio B does not have an energetically preferred value, and its diffusive behavior is therefore unrestricted. A practical consequence is that in simulations the quantity D_B can be determined more accurately than D_A, as the latter shows a crossover from short-time diffusive behavior to late-time saturation.

In our simulations, we have studied samples of polycrystalline graphene with a variation in the amount of structural relaxation, the size of the crystalline domains, and the density of structural defects (mainly fivefold and sevenfold rings). In our simulations, we show a linear relation between the number of such structural defects and the diffusion coefficient D_B. In well-relaxed samples, large crystalline domains are separated from each other by rows of structural defects. Consequently, the number of defects decreases linearly with the average domain size. We therefore expect also that the diffusion coefficient D_B decreases linearly with the average domain size. In this context it will be useful to deepen this connection to domain size engineering [91, 108, 109], fabrication of polycrystalline graphene [110–112], mechanics of grain boundaries [113, 114].

From a materials science point of view, as well as from an experimental point of view, the mechanical behavior of a sample of graphene under external forces is important. We show that the deformation of graphene under an external shear force is related to the quantity D_B which is readily accessible in simulations, via the Nerst-Einstein relation. For this purpose, the external shear force is translated into a force f_B on the quantity B, after which the shear rate $v_B = \partial B / \partial t$ can be obtained from equation (3.8), in which the diffusion coefficient D_B is used. And the mechanical deformation can then be readily obtained from v_B.

We have limited ourselves to a relatively modest dynamical range of L_x and L_y, as well as relatively mild deformation forces. Consequentially, in our simulations the domains do not get deformed to elongated shapes but retain circular symmetry. If the material would be stretched significantly in a time that is short enough to rule out complete structural rearrangement, elongated domains should arise, and the sample would experience restoring forces back towards its original shape. This is illustrated in Fig. 3.6(a). We speculate that this mechanism would actually slow down the shearing process, making the shear distance non-linear in time. Our simulations show signs of the onset of decreasing shear rate in time [Fig. 3.6(d)]. A quantitative study of this phenomenon, in which the possible relation between elongation of domains and non-linear shear is investigated both in experiments and mechanism, such as strengthening or weakening of graphene [10, 115, 116], fracture toughness [117–119], mechanical mutability [120], requires very long simulations, which we will pick up in future work. We believe these investigations enhance our understanding of the mechanical properties of polycrystalline graphene.

CHAPTER 4

Structural dynamics of a model of amorphous silicon

Abstract

We perform extensive simulations and systematic statistical analyses on the structural dynamics of a model of amorphous silicon. The simulations follow the dynamics introduced by Wooten, Winer and Weaire: the energy is obtained with the Keating potential, and the dynamics consists of bond transpositions proposed at random locations and accepted with the Metropolis acceptance ratio. The structural quantities we track are the variations in time of the lateral lengths (L_x, L_y, L_z) of the cuboid simulation cell. We transform these quantities into the volume V and two aspect ratios B_1 and B_2. Our analysis reveals that at short times, the mean squared displacement (MSD) for all of them exhibits normal diffusion. At longer times, they cross over to anomalous diffusion, with a temperature-dependent anomalous exponent $\alpha < 1$. We analyze our findings in the light of two standard models in statistical physics that feature anomalous dynamics, *viz.*, continuous time random walker (CTRW) and fractional Brownian motion (fBm). We obtain the distribution of waiting times, and find that the data are consistent with a stretched-exponential decay. We also show that the three quantities, V, B_1 and B_2 exhibit negative velocity autocorrelation functions. These observations together suggest that the dynamics of the material belong to the fBm class.

4.1 Introduction

Amorphous silicon (a-Si) has attracted a lot of attention in the computational materials science community over the last decades, partly because it is a material with many applications, and partly because it has become a prototypical example of a covalently bonded disordered material that lends itself well for simulations, as many empirical and semi-empirical potentials are readily available. There exist a myriad of experimental and simulation research works on the properties of a-Si, studying thermal transport [121, 122], structure and defects recognition [123], electronic properties and applications for solar cells [124–126], and vibrational properties [127]. Compared to structural and electronic properties, the dynamics of a-Si is less studied. In this chapter we fill the knowledge gap on how structural properties of the material evolve in time. Dynamics of covalently-bonded materials are well-known to be extremely slow. On the one hand, it makes them highly stable, but on the other it renders them nearly impossible to be accessed by experimental time scales. Computer simulations can provide a way forward, but there too, simulation studies of a-Si dynamics have often focused on how to generate well-relaxed samples as efficiently as possible, but do not study the fundamental properties of its dynamics.

In this chapter, we employ a relatively simple model for the dynamics of a-Si, as first introduced by Wooten, Winer and Weaire (WWW) [87]. The atomic structure in this model is described as a so-called continuous random network (CRN), in which each silicon atom has exactly four covalent bonds to other silicon neighbors. To each CRN-configuration, an energy is attributed using the Keating potential [89]. The dynamics consists of a sequence of bond transpositions proposed at random locations, and accepted or rejected according to the Metropolis algorithm. This technique allows for the simulation of the dynamics of a-Si over time scales that are much longer than those accessible to molecular dynamics (MD), at the expense of being a much cruder description. There is a however a connection between the two time scales. Within our Monte Carlo (MC) dynamics, the probability that a specific bond transposition is proposed in one MC unit of time is $2/(4 * 3 * 3 * N) = 1/(18N)$. Here, factors $1/N$, $1/4$, $1/3$ and $1/3$ respectively arise from picking a random atom (out of N total atoms), then one of its four neighbours, next twice one of the three remaining neighbours, and the factor of 2 comes from the possibility to generate the same string of atoms from two different ends. The acceptance probability is then $\exp(-\beta \Delta E)$, where ΔE is the energy difference between the initial and final states. Thus, the rate of structural changes in the sample is $(1/18N) \exp(-\beta \Delta E)$.

In molecular dynamics (MD), the rate would be $\nu \exp(-\beta B)$ where ν is the attempt frequency, often found to be around 10^{-12} s^{-1}=1 ps^{-1}, and B is the energy barrier between the initial and final states. The energy barrier B and the energy change ΔE are correlated, but loosely. For instance, we know that B has to be higher than ΔE. For example, from earlier work [Ref. [128], Table

1] we know that on average for bond transpositions (WWW events), $\langle \Delta E \rangle = 4.0$ eV and $\langle B \rangle = 2.2$ eV. As a rough estimate of $\Delta E - B$, we can then take $\langle B \rangle - \langle \Delta E \rangle = 1.8$ eV. Our simulations were carried out at a temperature of 0.14 eV, with $N = 2000$ atoms. We then obtain that one unit of MC time corresponds roughly to $(1/(18N)) \exp(1.8/0.14)$ ps ≈ 10 ps.

In our simulations, we use a cuboid simulation cell with periodic boundary conditions, and lateral dimensions $L_x \times L_y \times L_z$. At all times, these lateral dimensions, together with all the atoms, constitute $N+3$ degrees of freedom. After each WWW move, the bond list is updated, and all degrees of freedom are minimized to the global minimum of energy, and consequently these lateral dimensions of the simulation cell will fluctuate in time. In our case, these fluctuations are easily accessible in simulations, and are closely related to the mechanical deformations under (small) external forces, and therefore a standard approach for understanding the mechanical shear and stress properties of the bulk material. All dynamics studied in the chapter is performed at the temperature below the melting temperature of a-Si (1750K[129]).

We transform the three quantities $L_x(t)$, $L_y(t)$ and $L_z(t)$ into three other quantities, which are the volume $V(t) \equiv L_x(t) \cdot L_y(t) \cdot L_z(t)$ and the two aspect ratios $B_1(t) = L_y(t)/L_z(t)$ and $B_2(t) = L_y(t) \cdot L_z(t)/L_x^2(t)$. The aspect ratios $B_1(t)$ and $B_2(t)$ are two (almost) unconstrained degrees of freedom, which can vary over a wide range of values without preference. This however does not hold for the volume $V(t)$ as it is constrained to fluctuate around an ideal value set by the number of atoms and the ideal density. (It is well-known that well-relaxed samples of a-Si can be obtained within a wide range of densities: fluctuations of several percent are easily observed. Thus, the constraint is rather loose for this specific material.)

The focus of this chapter lies on the dynamics of V, B_1 and B_2. The motivation for this choice is that these are quantities that lend themselves well for computer simulations studies, and are directly connected to the mechanical behavior under shear, stress, etc., which are of experimental relevance. Our findings indicate that over short time scales, all three quantities exhibit diffusive behavior; this is to be expected, as over a short time, the dynamics consist of local atomic rearrangements which cause random changes in B_1, B_2 and V which are uncorrelated. At longer times, a negative velocity autocorrelation emerges: a positive change induces a bias at later times to be followed by a negative change, vice versa. These correlations are strong enough to change the dynamics from ordinary to anomalous diffusion: the mean squared deviations MSD_1, MSD_2 and MSD_V for B_1, B_2 and V can be fitted by a power-law $\sim t^\alpha$ with $\alpha < 1$. The exponent is found to be temperature-dependent. (Given that $V(t)$ is constrained to fluctuate around an ideal value as noted above would mean that the mean-square displacement of V must reach a plateau at a long time. Our simulation times are however not long enough, i.e., the mean-square displacement of V does not reach a high enough value to be influenced by the constraint.)

We analyze our findings in the light of standard models for anomalous diffusion, *viz.*, the continuous time random walk (CTRW) model and fractional Brownian motion (fBm). For this purpose, we also determine numerically the distribution of the waiting times. This distribution can be well fitted by a function with stretched-exponential decay. Although this is different from homogeneous, memoryless materials, where the decay is expected to be exponential, the decay is still too steep to be the sole explanation of anomalous diffusion. We also determine the velocity autocorrelation functions, and find them to be negative at all times.

The organization of this chapter is as follows. In Sec. 4.2, we introduce the model and simulation methods in detail. In Sec. 4.3.1, we define the structural quantities related to the mechanical properties, analyze the trajectories extracted from simulations, investigate the short-time behavior of mean-square displacements, and describe the relationships among the different diffusion coefficients. In Sec. 4.3.2, we analyze the probability distribution, both on waiting time and jump length, characterize sub-diffusive behaviors at long times, and reflect on the classification of the model. In Sec. 4.4 we summarize and conclude the chapter.

4.2 The model

The Keating potential is one of the simplest and most efficient models for describing a-Si. It uses an explicit list of bonds: whether two atoms interact with each other or not, is thus determined by this bond list, and not by the distance between the atoms. It is defined as

$$ E = \frac{3}{16}\frac{\alpha}{d^2}\sum_{<ij>}(\mathbf{r}_{ij}\cdot\mathbf{r}_{ij}-d^2)^2 + \frac{3}{8}\frac{\beta}{d^2}\sum_{<ijk>}(\mathbf{r}_{ij}\cdot\mathbf{r}_{ik}+\frac{1}{3}d^2)^2. \qquad (4.1) $$

Here, $\mathbf{r}_{ij}$ is the bond vector between atoms i and j. $d = 2.35$ Å is the ideal bond length for pure crystal silicon. α is two-body term constant, taken to be 2.965eVÅ$/d^2$, β is the three-body term, set as 0.285α.

At the beginning of each simulation, an initial sample has to be prepared. In order to ensure that our initial sample is homogeneous and isotropic, we start with randomly placed points in a cubic box, and then determine the Voronoi diagram between these random points. The set of edges in the Voronoi diagram forms a fourfold-coordinated CRN, and each edge is then seen as a bond of the initial explicit bond list. At the locations where four edges meet, a silicon atom is placed. From this moment on, the initial random points no longer have a role.
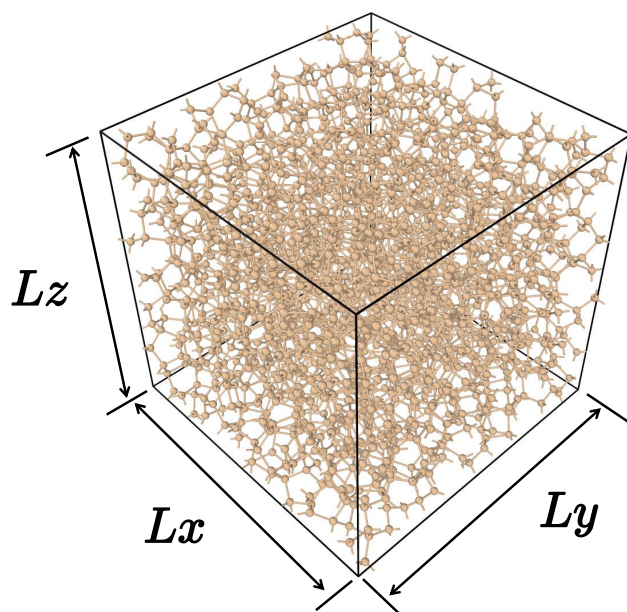
Figure 4.1: (color online) An initial sample of amorphous silicon with 2000 atoms, each connected to four neighboring atoms. The bonds have comparable length (2.35Å with a spread of 0.085Å), and the bond angles are close to the tetra-hedral angle (109.46° with a spread of 9.5°). The sample has been generated, starting from a Voronoi diagram and then evolved using the WWW-algorithm, as discussed in Sec. 4.2. It is a cuboid with periodic boundaries on the lateral dimensions L_x, L_y and L_z.
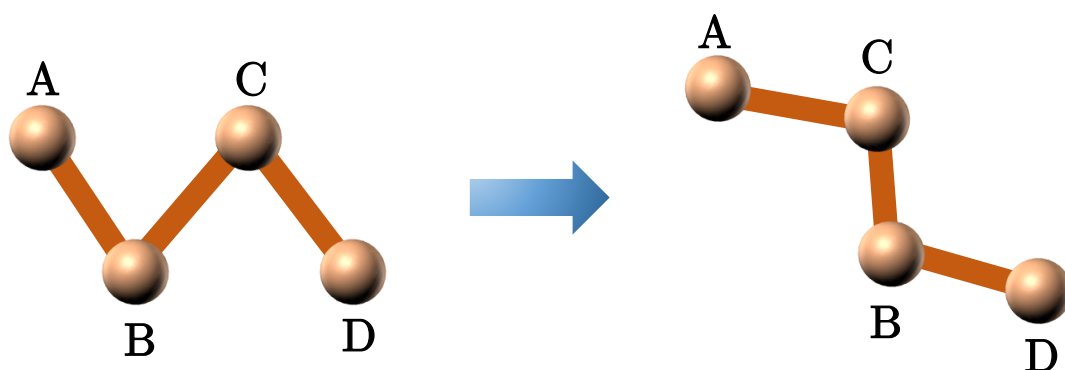
Figure 4.2: (color online) Diagram of a bond transposition which is part of the WWW algorithm. A string of connected atoms ABCD is chosen, then the bonds AB and CD are replaced by AC and BD. The new string is subsequently relaxed by the following local energy minimization.

Next, the atomic positions are allowed to relax, while preserving the explicit bond list; this is done by a straightforward local energy minimization (implemented as discussed below). The resulting initial sample is homogeneous and isotropic, but poorly relaxed. An often used characterization of the degree of relaxation is via the spread in bond angles. While in experimental a-Si samples, the angular spread ranges from 10 degrees for well-relaxed samples to 12 degrees for poorly relaxed samples, these initial Voronoi-created samples have an angular spread of 15 degrees or more. In order to relax the sample, we follow the procedure initially proposed by Wooten, Winer and Weaire (WWW). Randomly, somewhere in the sample, a string of four connected atoms ABCD is chosen. Next, a bond transposition is made: the bonds connecting these four atoms are reconnected, by replacing the bonds AB and CD by bonds AC and BD, as shown in Fig. 4.2. This is followed by a local energy minimization [130] under the new explicit bond list, which changes the atomic coordinates slightly. This proposed bond transposition is then either accepted or rejected, according to the Metropolis criterion [18]. The acceptance probability is given by

$$P_{\mathrm{acc}} = \mathrm{Min}\left[1, \exp(-\beta \Delta E)\right], \qquad (4.2)$$

where ΔE is the change in energy due to the proposed bond transposition, and $\beta = (k_{\mathrm{B}}T)^{-1}$ with temperature T and Boltzmann constant k_{B}. Typically, many thousands of such bond transpositions are required, for obtaining a well-relaxed a-Si sample.

The time-consuming part of this WWW algorithm is the local energy minimization. Our algorithm of choice for doing this, is the fast inertial relaxation engine (FIRE) algorithm. Typical parameters are set as same as in the Ref. [107]: $N_{\mathrm{min}} = 5$, $f_{\mathrm{inc}} = 1.1$, $f_{\mathrm{dec}} = 0.5$, $\alpha_{\mathrm{start}} = 0.1$ and $f_{\alpha} = 0.99$. Other custom parameters here are set as $\Delta t_{\mathrm{MD}} = 0.06$, $\Delta t_{\mathrm{max}} \sim 10\Delta t_{\mathrm{MD}}$ and the velocity Verlet method is chosen for integration in time.

To improve the computational efficiency, we use early rejection of 'hopeless' moves, as discussed in Ref. [130–132]. At each proposed bond transposition, a threshold value for the energy is set. If the energy after relaxation stays above the threshold, the proposed move is rejected, otherwise it is surely accepted. During energy minimization after a proposed bond transposition, the total force is monitored, and used to make a conservative estimate of the energy that would be obtained after full minimization. If it is clear that this energy stays above the threshold, the bond transposition is rejected well before the time-costly full relaxation is achieved. In well-relaxed samples, this early-rejection gives a speed-up of one or two orders of magnitude.
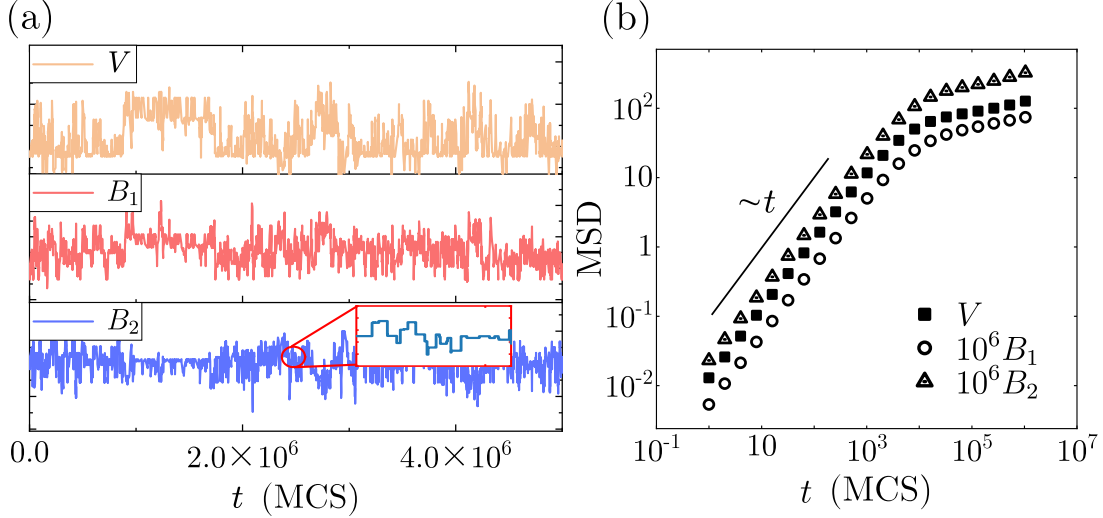
4.3   Dynamics of fluctuations in sample shapes

Figure 4.3: (color online) (a) Typical fluctuations of V, B_1 and B_2 (from top to bottom) evolved up to 5×10^6 Monte Carlo steps (MCS) for a sample with $N = 423$ atoms under $T = 1400\text{K}$. While, given enough time, B_1 and B_2 can take a wide range of values, V will only show fluctuations around its ideal value which is set by the density of the a-Si sample. The inset in the bottom panel exhibits stalling events (see text for details). (b) Measurements of the MSD for V, B_1 and B_2 respectively . B_1 and B_2 are multiplied by 10^6 to have the same scale as V. The results are obtained from averaging over 10 starting samples with 423 atoms ($T = 1400\text{K}$), each evolved 50 times with different random seeds over 10^7 proposed bond transpositions to achieve a good statistical performance, which offset the noise generated by a single evolution. At short times, all three curves of the MSD initially increase linear in time, i.e. show ordinary diffusion. After $\sim 10^4$ attempted bond transpositions, the increase slows down significantly. All curves show a crossover to subdiffusive behavior. For the MSD_V we expect eventually saturation; this seems to be at times beyond those of our simulations.

As shown in Fig. 4.1, we perform our simulations in the periodic and cuboid simulation box $L_x \times L_y \times L_z$ in the x-, y- and the z-directions respectively. These are however not fixed quantities, but are allowed fluctuate when the bond transpositions are made as the sample evolves in time.

Throughout this chapter, we consider three geometric quantities, defined as

follows:

$$
\begin{aligned}
V(t) &= L_x(t)L_y(t)L_z(t), \\
B_1(t) &= L_y(t)/L_z(t), \\
B_2(t) &= L_y(t)L_z(t)/L_x^2(t).
\end{aligned}
\tag{4.3}
$$

Physically, for a cuboid sample such as ours, the dynamics of shape fluctuations of the sample can be efficiently characterized by associating $V(t)$ to the dynamics of the "bulk" mode, and $B_1(t)$ and $B_2(t)$ with that of the "shear" modes. Fig. 4.3(a) shows the trajectories for these quantities in Monte-Carlo time at short times. The stalling events seen therein (inset, Fig. 4.3(a)) result from the *rejected* bond transpositions at short time intervals. Figure 4.3(b) displays the MSD for V, B_1 and B_2, respectively. At short times, there are only few bond transpositions which occur at spatially separated locations, and thus these are uncorrelated events, which yield normal diffusive behavior. At longer times, this spatial separation breaks down, and the bond transpositions start to feel each other; for instance, a bond transposition which leads to local contraction has an enhanced probability to be followed by another bond transposition that leads to local expansion. The cross-over point represents the transition from normal diffusion to anomalous diffusion of the physical quantity under study.

4.3.1 Diffusive behavior at short times

At short times, we track the dynamics of shape fluctuations of the samples in terms of the mean-square displacements $\mathrm{MSD}_V(t) = \langle [V(t) - V(0)]^2 \rangle$, $\mathrm{MSD}_1(t) = \langle [B_1(t) - B_1(0)]^2 \rangle$ and $\mathrm{MSD}_2(t) = \langle [B_2(t) - B_2(0)]^2 \rangle$, with the angular brackets denoting ensemble averages for a sample of fixed number of atoms and (more or less) constant energy. As shown in Fig. 4.3(b), At short times, all three quantities exhibit ordinary diffusive behavior, i.e. $\mathrm{MSD}(t) \sim t$. V is expected to saturate after super long times due to the constraint of structural density, while significant crossovers (nearly at 10^4) to sub-diffusion can be observed in $\mathrm{MSD}_1(t)$ and $\mathrm{MSD}_2(t)$ i.e. $\mathrm{MSD}(t) \sim t^\alpha$ ($\alpha < 1$). Here the results are obtained from averaging 10 starting samples ($N = 423$) each evolved 50 times.

$$
\mathrm{MSD}(t) = 2Dt.
\tag{4.4}
$$

By fitting the MSD for V, B_1 and B_2 we extract the corresponding diffusion coefficients D. Since V, B_1 and B_2 all bear relations to L_x, L_y and L_z, one would expect them to be related through these length parameters, which we establish below. In order to do so, having denoted the change in V, B_1 and B_2 over a small time interval dt for samples with dimensions L_x and L_y by dV, dB_1 and

dB_2 respectively, we express them in terms of small changes dL_x, dL_y and dL_z as

$$\langle dV^2 \rangle = \langle [L_y L_z dL_x + L_z L_x dL_y + L_x L_y dL_z]^2 \rangle$$

$$\langle dB_1^2 \rangle = \left\langle \frac{1}{L_z^4}[L_z dL_y - L_y dL_z]^2 \right\rangle \quad \text{and}$$

$$\langle dB_2^2 \rangle = \left\langle \frac{1}{L_x^6}[L_x L_y dL_z + L_z L_x dL_y - 2L_y L_z dL_x]^2 \right\rangle. \tag{4.5}$$

Numerically, we find that cross-terms such as $\langle dL_x dL_y \rangle$ etc. are much smaller than terms like $\langle dL_x^2 \rangle$. Similarly, it can be argued that thermal kicking on a sample acts like a force in the x-, y- and z- directions as stretching forces, and the sample cannot distinguish among the three directions. In particular, if the condition holds that the extension of the sample along the x-direction is inversely proportional to the corresponding spring constant $(L_y L_z)^{-1}$, then $\langle dL_x^2 \rangle \sim (L_y L_z)^{-2}$ etc. These two assumptions lead to the following scaling relations between the diffusion coefficients:

$$D_V/D_{B_1} \propto \langle L_x^2 L_z^4 \rangle$$
$$D_{B_1}/D_{B_2} \propto \langle L_x^4/L_z^4 \rangle$$
$$D_V/D_{B_2} \propto \langle L_x^6 \rangle. \tag{4.6}$$
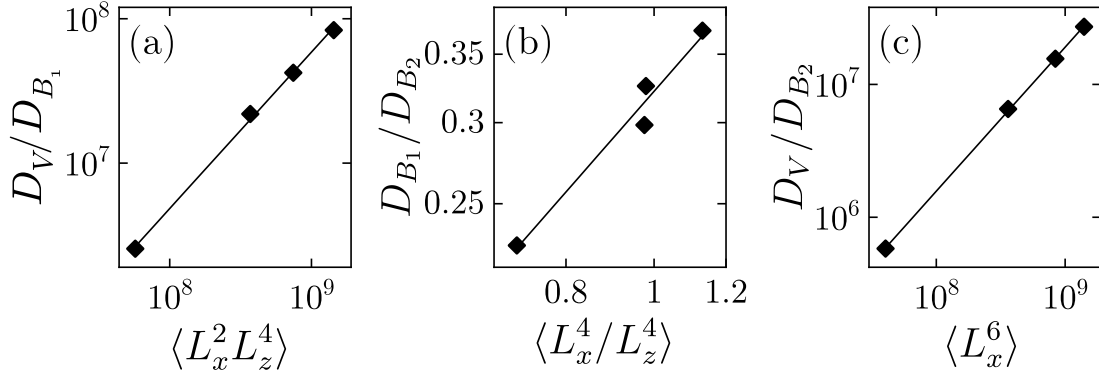
Figure 4.4: (a)-(c) Double logarithmic plots showing the relations between any two of the diffusion coefficient of the quantities we construct, which are built through statistical value of the lateral lengths. $D_V \sim \alpha_1 \langle L_x^2 L_z^4 \rangle D_{B_1}$, $D_V \sim \alpha_2 \langle L_x^4 \rangle D_{B_2}$, $D_{B_1} \sim \alpha_3 \langle L_x^4/L_y^4 \rangle D_{B_2}$, here α_1, α_2 and α_3 are constants and numerically obtained from our simulations as: 0.0584, 0.3302 and 0.0195, respectively

The numerical results are shown in the Fig. 4.4, the diffusion coefficients (corresponding to the short time part in the Fig. 4.3(b)) are measured according to the Eq. 4.4, the four data points in each plots are measured over

$N = 423, 1000, 1500$ and 2000. Data is collected by averaging over 10 initial samples, each evolved 50 times over 10^7 proposed bond transpositions. It is numerically found that $D_V \sim \alpha_1 \langle L_x^2 L_z^4 \rangle D_{B_1}$, $D_V \sim \alpha_2 \langle L_x^6 \rangle D_{B_2}$, $D_{B_1} \sim \alpha_3 \langle L_x^4 / L_z^4 \rangle D_{B_2}$, the factors α_1, α_2 and α_3 are constant and fitted from our simulations: 0.0584, 0.3302 and 0.0195, respectively, we infer that these values are more likely to depend on factors such as sample size, amount of data, measurement time length, system noise, etc., which can be used as references in future experiments.

4.3.2 Characterizing material dynamics at long times
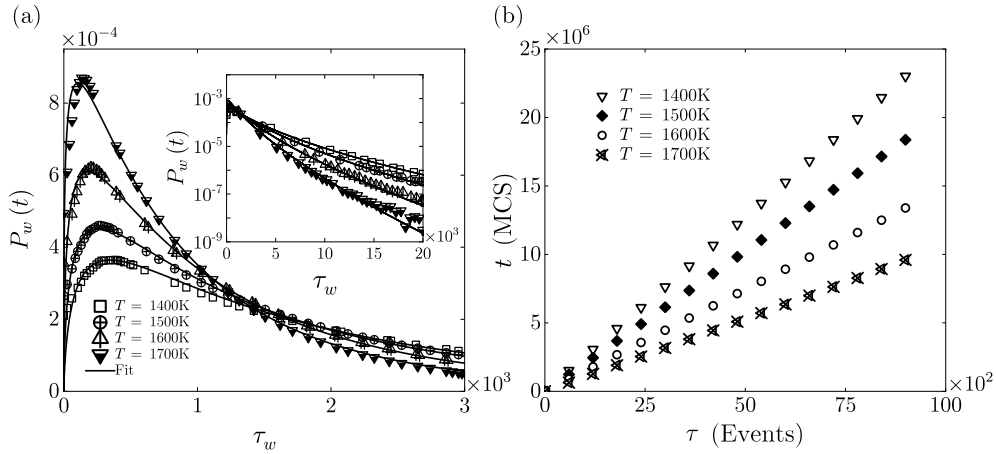
Figure 4.5:   (a) Waiting time distribution fitted to Eq. (4.7) for $N = 423$ at various temperatures (up to $\tau_w =$ 3,000), inset: fit for lager scales (up to $\tau_w =$ 20,000). (b) Monte Carlo time t for a sample with $N = 423$, measured in the number of proposed bond transpositions, in comparison with the event time τ, measured in the number of accepted bond transpositions. Each dot in this scatter plot is a measurement of both times, elapsed between accepted bond transpositions. The data show a linear relation between t and τ, with a temperature-dependent scale factor. As is to be expected, there is some spread in the data points at short times, which decreases with increasing times.

In comparison to the short time dynamics, the dynamics at long times is much more noisy, simply because obtaining very long time series for an a-Si sample is not easy. Just to give an idea, a run on a single core of Intel i7-9700k CPU, our simulations require 0.005s/step for a sample with 1000 atoms for $T = 1500K$. Given that the crossover event often takes place at 10^4 steps, at least 10^6 steps, and averaging over 50 independent sample runs, costing five days, would be required for obtaining results with good statistics (larger samples and lower temperatures would require even longer times.) To complicate matters, we also have to deal

with the stalling events. Fortunately, we have found a way to go around the complications due to the stalling events, as described in Sec. 4.3.2 below.

Stalling events complicate handling of time-series data

The stalling events pose us with a difficulty on how to cleanly handle the dynamics data at long times: specifically, V, B_1 and B_2 changing only at irregular time intervals means that ensemble averages, calculated standardly from time-series data, is bound to be very noisy (it is!) at long times. Stalling events are a manifestation of the MC procedure: over a stalling period, which is synonymous to a *waiting time* (i.e., the sample configuration is waiting for a change), all proposed bond transposition events in the MC procedure are rejected. That said, the stalling events also provide us with the opportunity to measure time in units of *accepted* bond transposition moves, τ, instead of the standard units of MC time t, measured in units of *attempted* bond transposition moves. Clearly, the quantity τ increases by unity at every accepted move, even though the MC time between two successive accepted moves, the waiting time can be widely different due to stochasticity of the process. Indeed, when measured in units of τ, we find that the dynamical quantities at long times are far less noisy, and for this reason, throughout this section we measure time in units of τ.

But before we get to the dynamics, we present the probability distribution of the waiting time $P_w(t)$ in Fig. 4.5(a) for a sample with $N = 423$ and a couple of different temperature values. Plotting the data in log-linear plot, and subsequent analysis, reveals that the $P_w(t)$ data are well fitted by the following formula:

$$P_w(t) = at^b e^{-(\tau_w/\tau_c)^d}, \tag{4.7}$$

where a is a normalization constant. The fitting parameters are noted in Table 4.1. In particular, we note that the waiting time distributions do not have power-law tails. We will return to this aspect later in this section. Moreover, in Fig. 4.5(b) we also show that the mean waiting time is a constant throughout the duration of the simulation (the constant corresponds to the inverse rate of the accepted moves).

Table 4.1: Parameters for the fitted waiting time distribution in Fig. 4.5(a).

Temperature (K)	a	b	τ_c	d
1400	2.070×10^{-5}	0.767	125.000	0.474
1500	4.721×10^{-5}	0.615	195.100	0.525
1600	1.179×10^{-4}	0.466	274.800	0.595
1700	3.315×10^{-4}	0.300	350.000	0.667

Anomalous diffusion of V, B_1 and B_2
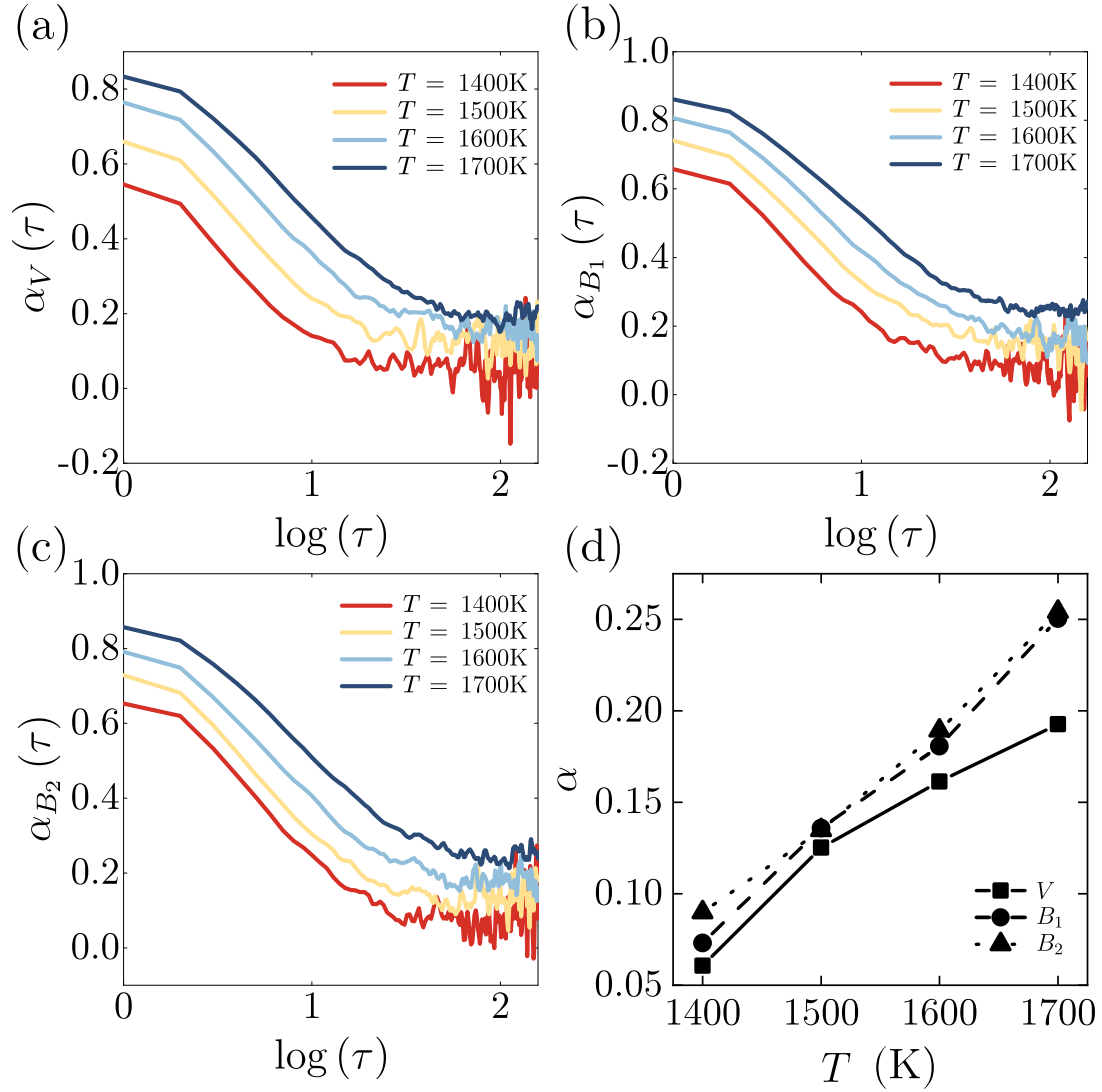
Figure 4.6: (color online) (a)-(c) Measurement of the exponent α in $\log(\tau)$ scale for various temperatures with fixed $N = 423$. α is smaller then 1 throughout the entire time, which indicates a subdiffusive behavior for the corresponding mean-square displacement. After an initial period of crossover time, α eventually converges to a small value (0.1-0.3). (d) The anomalous exponent (as defined in Eq. 4.8) as obtained from the MSD of B_1, B_2 and V, as a function of temperature. At higher temperatures, the values of α obtained from the MSD of V are lower than those for B_1 and B_2, probably because large deviations of the density away from the crystalline value are suppressed (as discussed in the text).

Double logarithmic plots of the mean-square displacements reveal that the dynamics of V, B_1 and B_2 is no longer diffusive, i.e., they are anomalous, at long times. Assuming that the $\mathrm{MSD}_V(\tau)$, $\mathrm{MSD}_{B_1}(\tau)$ and $\mathrm{MSD}_{B_2}(\tau)$ increase as a power-law in τ at long times, we compute the effective exponents for these variables, collectively denoted by Q, as

$$\alpha_Q(\tau) = \frac{d\log[\mathrm{MSD}_Q]}{d\log\tau}. \tag{4.8}$$

An example plot for α_Q is shown for $N = 423$ in Fig. 4.6(a)-(c) above. The exponents we find are dependent on temperature (shown in Fig. 4.6(d)). It seems to us that lower temperature leads to lower subdiffusion exponent, even though measuring exact exponents properly is difficult given long run times. The approximate exponents for each quantities at various temperature are list in Tab. 4.2.

Table 4.2:   The anomalous diffusive exponent α for V, B_1, and B_2 with fixed $N = 423$ and various T.

Quantity	T (K)	α
V	1400	0.06
V	1500	0.13
V	1600	0.16
V	1700	0.20
B_1	1400	0.07
B_1	1500	0.14
B_1	1600	0.18
B_1	1700	0.25
B_2	1400	0.09
B_2	1500	0.13
B_2	1600	0.19
B_2	1700	0.25

Further analysis of anomalous diffusion

Long runtimes required to obtain long time series of sample snapshots prevent us to pinpoint the exponents with higher numerical accuracy. Nevertheless, we can still reflect on the nature of the anomalous diffusion we observe here for a-Si. In particular, in the past work of two of us, we have observed that anomalous diffusion in materials tend to belong to the fractional Brownian motion (fBm) class, while their stochastic dynamics described by Generalized Langevin equation (GLE) with power-law memory [133–136], with the exponent of the power-law memory, within the numerical accuracy, matching the anomalous diffusion exponent really well. The memory can be interpreted in terms of restoring forces:

when thermal fluctuations move a sample configuration one way, subsequent fluctuations tend to undo that move. If the simulations of a-Si were amenable to reach sufficiently long times, we would be able to perform a similar analysis here as well; unfortunately that is not the case.
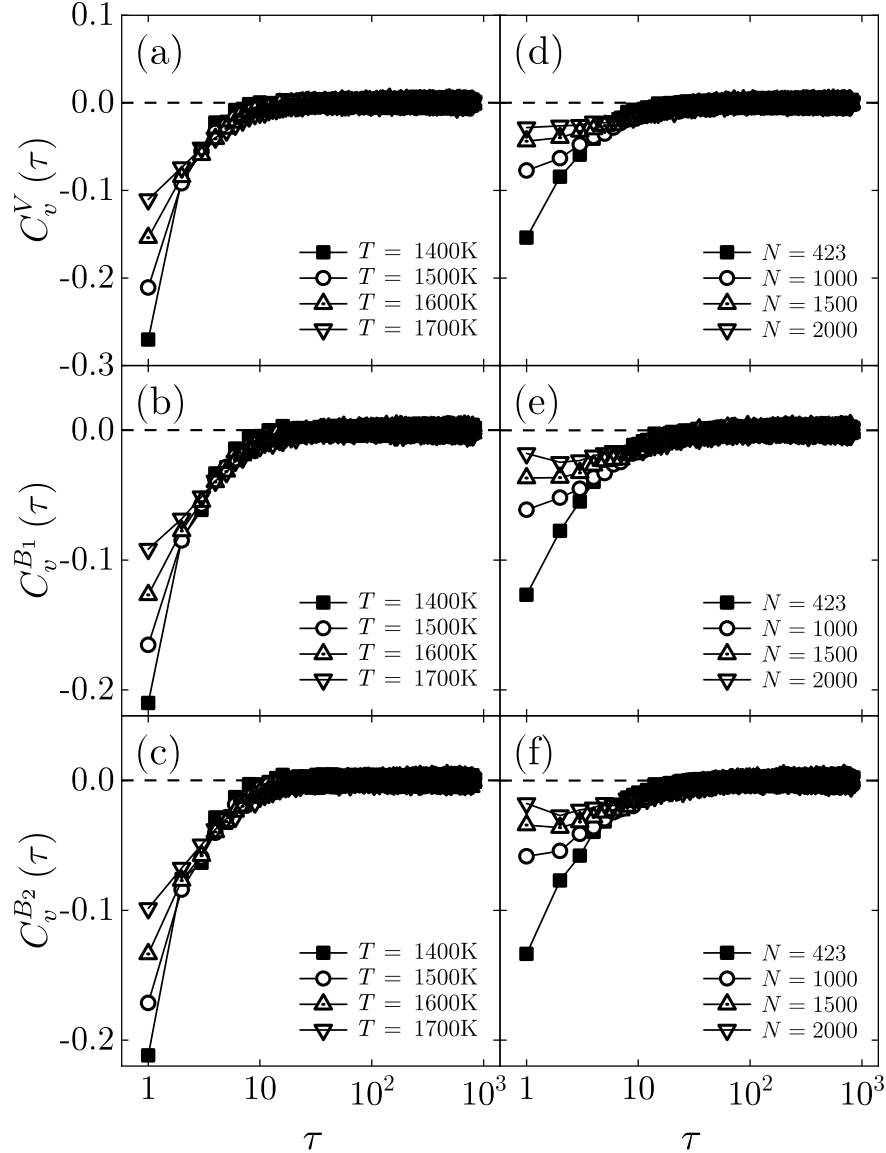
Figure 4.7: Normalized velocity auto-correlation functions (VACF) of V, B_1 and B_2 for various temperatures with fixed $N = 423$ (a)-(c) , and (d)-(f) for various the number of atoms with a fixed temperature of 1500K. The VACF are clearly negative at very short times, indicating that there is a restoring tendency: if in one bond transposition, the sample shears one way, the following bond transposition has a bias in favor of undoing the earlier shear. It also implies the autocorrelation is weaker for a larger system.

$$C_v^Q(\tau) = \frac{\langle v_Q(\tau)\, v_Q(0)\rangle}{\langle (v_Q(0))^2\rangle}. \tag{4.9}$$

That said, given that the waiting times do not have a power-law tail, as demonstrated in Fig. 4.5 rules out a continuous-time random walk (CTRW) type stochastic process for V, B_1 and B_2. To completely rule out CTRW, we plot the velocity autocorrelation function (VACF) for these quantities in Fig. 4.7, VACF $C_v^Q(\tau)$ is defined in Eq. 4.9 for quantity Q, where $v_Q(\tau) = \partial Q/\partial \tau$ is the velocity of the quantity Q. These data rather cleanly demonstrate that the VACF is negative for $\tau \neq 0$, and approaches zero for large τ from below the x-axis.

For completeness, we also present the jump length distributions of B_1, B_2 and V in Fig. 4.8. Note that these distributions do not feature fat tails, thereby ruling out Levy-flight like effects.

4.4   Discussion
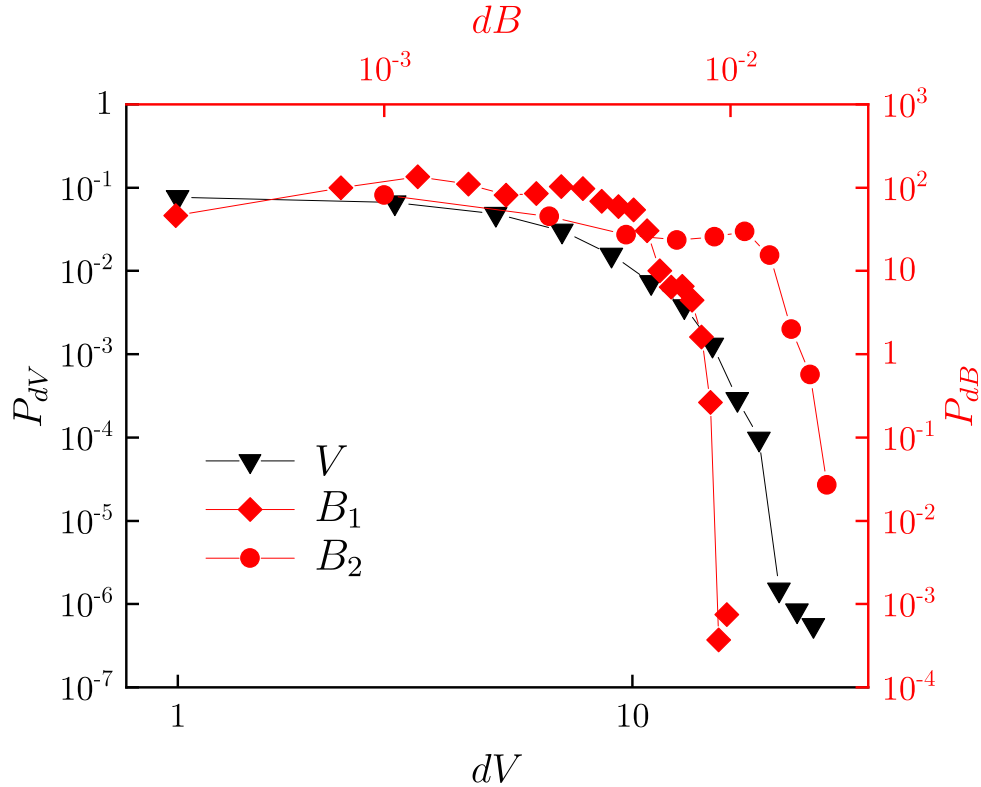

Figure 4.8: (color online) Double logarithmic plots of the jump length distribution for B_1, B_2 and V ($N = 423$, $T = 1500$K). None of these distributions feature fat (power-law) tails, thereby ruling out Levy-flight behavior.

This manuscript studies the structural dynamics of a model of amorphous silicon, in particular the fluctuations in the volume V of the simulation box, as well as in its aspect ratios B_1 and B_2. The simulations show that these three variables show ordinary diffusive behavior at very short times, crossing over to anomalous diffusion at longer times: their MSDs can be well fitted with a power-law MSD$\sim t^\alpha$ with $\alpha < 1$. We find that the anomalous exponent α is temperature-dependent.

Various models in statistical physics exist that also feature anomalous dynamics; two well-known examples are the continuous time random walker (CTRW) and fractional Brownian motion (fBM). In further investigation, we present the distribution of the waiting times, as well as the velocity autocorrelation functions. These further results show that the observed anomalous dynamics is consistent with fBM-like behavior, and not with CTRW-like behavior.

The observed fluctuations in the shape of the simulation cell are directly related to deformations of the material under external compression and shear forces. Our findings are therefore directly linked to experiment.

Domain coarsening in polycrystalline graphene

Abstract

Graphene is a two-dimensional carbon allotrope which exhibits exceptional properties, making it highly suitable for a wide range of applications. Practical graphene fabrication often yields a polycrystalline structure with many inherent defects, which significantly influence its performance. In this study, we utilize a Monte Carlo approach based on the optimized Wooten, Winer and Weaire (WWW) algorithm to simulate the crystalline domain coarsening process of polycrystalline graphene. Our sample configurations show excellent agreement with experimental data. We conduct statistical analyses of the bond and angle distribution, temporal evolution of the defect distribution, and spatial correlation of the lattice orientation that follows a stretched exponential distribution. Furthermore, we thoroughly investigate the diffusion behavior of defects and find that the changes in domain size follow a power-law distribution. We briefly discuss the possible connections of these results to (and differences from) domain growth processes in other statistical models, such as the Ising dynamics. We also examine the impact of buckling of polycrystalline graphene on the crystallization rate under substrate effects. Our findings may offer valuable guidance and insights for both theoretical investigations and experimental advancements.

This chapter is partially based on the following publication:

5.1 Introduction

Graphene is a two-dimensional (2D) material in which carbon atoms are organized in the structure of a honeycomb lattice. It exhibits a wide range of appealing properties in comparison to more conventional materials, including exceptionally high strength and toughness [137–142], remarkable thermal conductivity [143–147], and outstanding electrical conductivity [148]. As a result, use of graphene-based devices has witnessed a substantial surge in recent years [149–152]. Graphene can be fabricated experimentally through different methods, such as chemical vapor deposition (CVD) [153–156], epitaxial growth on silicon carbide [157, 158], and liquid-phase exfoliation [159, 160]. However, graphene produced using these techniques typically exists in a polycrystalline form, which means that the structure consists of many crystalline domains, each with its own lattice orientation. Neighboring domains are separated by strings of defects, usually five-fold and seven-fold rings. A sample of polycrystalline graphene is depicted in Fig. 5.1(d). Polycrystalline graphene grown on substrates often exhibits out-of-plane buckling near defects, a phenomenon that has been reported in numerous experiments and simulations [8, 161, 162]. Buckling can significantly affect the properties of graphene, however, its impact on the growth process is still less understood.

The structure of polycrystalline graphene is not stationary in time. Changes in the bonded structure occur all the time via the so-called bond translocations. If such a bond translocation occurs in the middle of a crystalline region, four six-fold rings evolve into two five- and two sevenfold rings [middle panel of Fig. 5.1(b)], a structure known as a Stone-Wales defect. Occasionally arising Stone-Wales defects in otherwise crystalline graphene tend not to last, and in due time, the crystalline structure is restored. If a bond translocation occurs in the immediate vicinity of a five- and sevenfold ring, the result is that this 5-7 pair is actually displaced sideways [right panel of Fig. 5.1(b)]. Via this mechanism, the domain walls separating the crystalline regions, consisting of alternating strings of five- and sevenfold rings, can actually wander.

The global effect of this wandering of the domain walls is *coarsening* or *domain growth*: bigger domains tend to grow at the expense of smaller ones, because of energetic considerations, and the density of domains decreases in time.

Here we study the domain growth process in graphene using computer simulations. First, in order to understand the force that drives the coarsening process, we study the energetics of polycrystalline graphene: in particular, we show that the total energy of the system increases monotonically with the number of 5- and 7-fold rings in a more or less linear fashion (Fig. 5.4). Next, we study the evolution in time of the defect density, spatial correlation of the lattice orientation and the average domain size. We find that the defect density scales as $t^{-1/3}$ in flat polycrystalline graphene, the spatial correlation of the lattice orientation is well fitted by a stretched exponential function, and the average size of the domains grows like $t^{1/6}$. We discuss similarities to the domain growth process (so-called

Ostwald ripening) in the Ising model. We also investigate the influence of buck-ling on the coarsening process and find that buckling of polycrystalline graphene slows it down. This implies that graphene samples with better crystallinity are best produced if the graphene is kept as flat as possible by a substrate.

This chapter is organized as follows. First, in Sec. 5.2, we describe our model for graphene, including its dynamics. In Sec. 5.3, we validate our model, and present that the structures resulting from simulations are in good agreement with experimental data. Next in Sec. 5.4, we present a statistical analysis of the spread in bond lengths and bond angles, structural disorder and defect density, as a function of time. We also present an extensive study of the lattice orientations, both in its spatial distribution and its dynamics. In Sec. 5.4.2, we analyses the diffusive behavior of defects and the separation of crystal phases. In section 5.4.3, we discuss the influence of binding to the substrate for buckled polycrystalline graphene. We conclude the chapter with a summary in Sec. 5.5.

5.2   Model

The overwhelming majority of carbon atoms in graphene are covalently bonded to three neighboring atoms; undercoordinated carbon atoms do exist, but at a density which is so low, that it can be safely neglected. In this work, we use the recently developed semiempirical energy potential which has the following form [99]:

$$E = \frac{3}{16}\frac{\alpha}{d^2}\sum_{i,j}\left(r_{ij}^2 - d^2\right)^2 + \frac{3}{8}\beta d^2\sum_{j,i,k}\left(\theta_{jik} - \frac{2\pi}{3}\right)^2 + \gamma\sum_{i,jkl}r_{i,jkl}^2. \qquad (5.1)$$

Here, r_{ij} is the distance between two bonded atoms i and j, θ_{jik} is the angle between the two bonds connecting atom i to atoms j and k and $r_{i,jkl}$ is the out-of-plane distance from atom i to the plane through the three atoms j, k and l. The parameter α is chosen as 26.060eV/Å^2 to control bond stretching and is fitted to the bulk modulus. The parameter $\beta = 5.511$eV/Å^2 governs bond shearing and is fitted to the shear modulus. The parameter $\gamma = 0.517$eV/Å^2 describes the stability of the graphene sheet against buckling; note that this third out-of-plane term is zero in perfectly flat graphene (2D simulations). $d = 1.420$Å is the ideal bond length for pure graphene. All these parameters are obtained by fitting to density functional theory (DFT) calculations [99]. Note that the elastic potential strictly requires the bond list where each atom is bonded to exactly three atoms; the number of bonds equals therefore $3N/2$, in which N is the number of atoms. This potential enables one to efficiently estimate the energies of the relatively stable configurations encountered in our simulations of graphene coarsening.
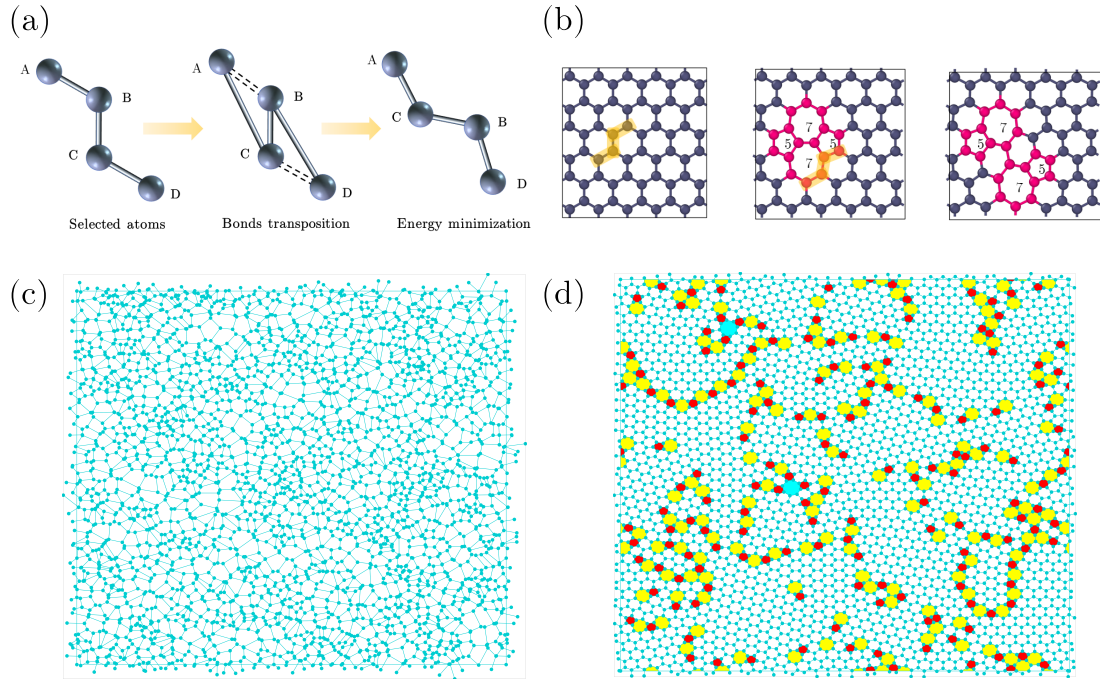
(a)

(b)

(c)

(d)

Figure 5.1: (a) Elementary move in the structural evolution of polycrystalline graphene, also known as a bond transposition. In a string of four carbon atoms A-B-C-D, the bonds A-B and C-D are replaced by bonds A-C and B-D, leaving the central bond B-C untouched. (b) Left panel: if a bond transposition occurs in crystalline graphene, it results in two oppositely oriented pairs of 5-7 rings. Right panel: if a bond transposition occurs in the immediate vicinity of a 5-7 pair, it effectively displaces sideways. The atoms marked in orange are selected for the bond transposition. (c) Visualization of an initial sample, created from a Voronoi network as described in the text. Note that the network is disordered and homogeneous, with at most tiny crystalline regions. (d) Same network after structural relaxation with 9×10^4 proposed bond transitions, when crystalline regions have appeared. In this figure, 5-, 7- and 8-fold rings are marked in different colors.

Simulations of covalently-bonded materials are typically slow and computationally expensive; their high stability causes the relevant experimental time scales to be well beyond those accessible by standard molecular dynamics simulations. Here we employ a relatively simple and accurate model for dynamics of polycrystalline graphene, which was initially applied for generating silicon samples with realistic structures. The model constructs atomic configurations generated by the evolution of a continuous random network (CRN) via bond transpositions, which is a well-established and widely used method to generate realistic atomic configurations of carbon/silicon materials. More specifically, we use the algorithm introduced in Ref. [131], an improved version of the original method of Wooten,

Winer and Weaire [87]. The improved bond transposition procedure consists of the following sequential steps: (1) constructing a comprehensive list of bonds in the current sample configuration; (2) randomly selecting four connected atoms (ABCD); (3) breaking the bonds between AB and CD and forming new bonds between AC and BD, as shown in Fig. 5.1(a); (4) performing global energy minimization and comparing the energy E_a after the bond switch with a predefined energy threshold, defined as:

$$E_t = E_b - k_\mathrm{B} T \ln (s), \tag{5.2}$$

where k_B is Boltzmann constant, T is temperature, E_b is the energy before the bond transposition and s is a uniform random number between 0 and 1. If the energy E_a after the bond transposition is less then E_t, the proposed change is accepted; otherwise, it is rejected, and the atoms and bond list are restored.

To accelerate the evolution program, we first relax only the atoms in the near vicinity of the bond transposition, bringing the total energy down to E_l. We then estimate the energy E_a after global relaxation (without performing the global minimization), employing a local energy criterion in term of the linear relationship between local minimum energy and the total remaining forces $|F|^2$:

$$E_a \approx E_l - c_f |F|^2 \tag{5.3}$$

Here, c_f is a linear factor obtained from simulations. In our recent work [104], we found that the performance of the local decision depends on the set of atoms allowed to move during the local relaxation; and for this, a shell of atoms was selected with the shortest-path distance l from the atoms involved in the bond transpositions. In the simulations discussed in the chapter, l and c_f are chosen as 3 and $6 \times 10^{-3} \ s^2 u^{-1}$ to achieve the best performance, respectively. Note that the quantity c_f is expressed in units of seconds squared over the atomic mass unit.

The minimization approach exerted in our simulations is the so-called fast inertial relaxation engine (FIRE) algorithm, in which parameters corresponding to Ref. [107] are set as: $N_{min} = 5$, $f_{inc} = 1.1$, $f_{dec} = 0.5$, $\alpha_{start} = 0.1$ and $f_\alpha = 0.99$. Other custom parameters here are set to be $\Delta t_{MD} = 0.03$ and $\Delta t_{max} \sim 10 \Delta t_{MD}$. The velocity Verlet method is chosen for the integration in time.

The domain growth presented in this chapter consists of Monte Carlo (MC) dynamics, consisting of a sequence of proposed bond transpositions described above. The time scale in this MC dynamics can be related to standard molecular dynamics method (MD). Within our MC dynamics, the probability that a specific bond transposition is proposed in one MC unit of time is $2/(3*2*2*N) = 1/(6N)$. Here, factors $1/N$, $1/3$, $1/2$ and $1/2$ respectively arise from selecting a random atom (out of N total atoms), then one of its three neighbors, next twice one of the two remaining neighbors, and the factor of 2 comes from the possibility

to generate the same string of atoms from two different ends. The acceptance probability is then $\exp(-\beta\Delta E)$, where ΔE is the energy difference between the initial and final states. Thus, the rate of structural changes in the sample is $(1/6N)\exp(-\beta\Delta E)$. In molecular dynamics (MD), the rate would be $\nu\exp(-\beta B)$ where ν is the attempt frequency, often found to be around 10^{-12} s^{-1}=1 ps^{-1}, and B is the energy barrier between the initial and final states. The energy barrier B is roughly equal to the sum of the energy for breaking a single bond and, if positive, the energy change ΔE.

Fig. 5.1(c) to (d) demonstrate the evolution process of polycrystalline graphene samples. Fig. 5.1(c) presents a Voronoi diagram with a random structure, providing an initial disordered state. Note that this initial state merely provides a homogeneous disordered network without orientational bias, and does not reflect any practical physical process. The construction of the Voronoi diagram involves several steps: (1) randomly choose a set of points within a simulation box; (2) for each seed point, determine its region, i.e. the set of points which are nearer to it, than to another seed point. (3) construct the boundaries of the Voronoi cells, which are formed by the perpendicular bisectors of the lines connecting neighboring seed points; (4) these boundaries are considered the covalent bonds, and the positions where three of these meet are considered as "atom'. Each "atom" within the Voronoi diagram is strictly limited to having three neighbors, and periodic boundary conditions (PBC) are applied to ensure a constant number of atoms (N) and bonds ($3N/2$) within the simulation box. Fig. 5.1(d) shows the evolution of a polycrystalline graphene structure with a defined defect density achieved by implementing 9×10^4 proposed bond transpositions. The nanocrystalline domains with distinct crystal orientations are separated by domain walls consisting mainly of 5- and 7-fold rings. Further, individual defect islands emerge within the crystalline domains.

5.3   Model validation

The model was first introduced in Ref. [99], which is based on Kirkwood's potential [163]. This potential has been used, for instance, for studying the structural dynamics of single-layer polycrystalline graphene[132], for studying the long-range relaxation of structural defects [99], for probing crystallinity of graphene samples via their vibrational spectrum [100] and for the study of the discontinuous evolution of the structure of stretching polycrystalline graphene [104].

Crystalline graphene is a 2D material, but as soon as the structure has defects — in particular if it is polycrystalline — the carbon atoms tend to relief stress by *buckling*, i.e. displace with respect to each other in the out-of-plane direction. For free-floating graphene in vacuum, the buckling can have an amplitude of many angstroms, while for graphene attached to a substrate, the amplitude of the buckling away from the substrate is suppressed significantly. In the first part

of our simulations, we confine the graphene to a 2D plane without any buckling; further on, we relax the constraint to the plane and allow for buckling.
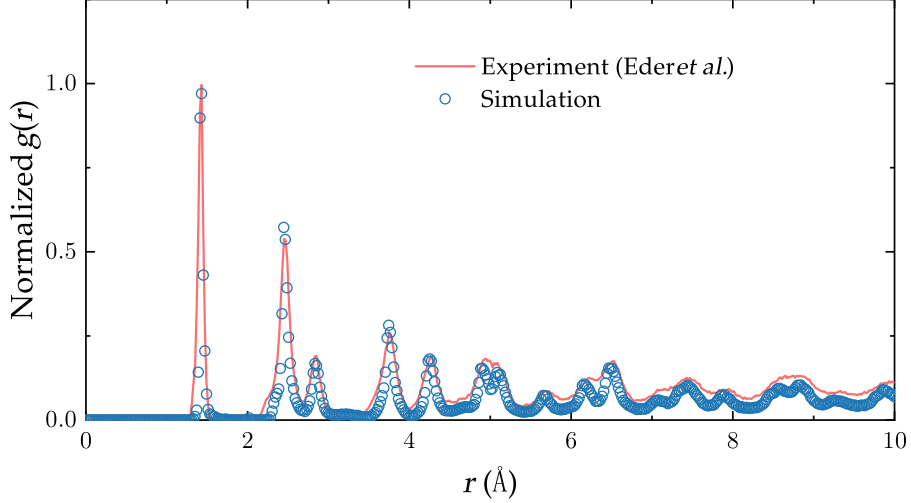

Figure 5.2: Comparison of the normalized radial distribution function $g(r)$ of our generated sample and experiment, at comparable defect density. The two curves match very well, up to about the first ten peaks.

In order to ensure the validity of the obtained samples, we employ the radial distribution function (RDF) as defined in Eq. (5.4), which characterizes the average spatial distribution of particles in a system. The RDF is defined as [164]

$$g\left(r\right) = \frac{\lim\limits_{\Delta r \to 0} \frac{N_r}{\pi(r+\Delta r)^2 - \pi r^2}}{\rho} \tag{5.4}$$

where r is the radial distance from reference particle, ρ is the average atoms density and N_r is the number of atoms between r and $r + \Delta r$. Starting from the initial configuration [Fig. 5.1(c)] we let the sample evolve in time. We then compare in Fig. 5.2, the normalized radial distribution function of the samples [Eq. (5.4)] on the 2D plane when the defect density reaches the same value ($\sim 20\%$) as in the experiment of Eder *et al.* [165]. (The defect density is defined as the ratio of non-hexagonal rings to the total number of rings.) The comparison reveals an excellent simulation-experiment agreement. Note also that the simulated samples we used have similar long-range disorder as the ones observed in real polycrystalline graphene.

5.4 Results

5.4.1 Domain growth in flat polycrystalline graphene

For studying domain growth of realistic polycrystalline graphene samples, at $t = 0$ we start with one consisting of 9800 atoms and a defect density of $\sim 20\%$. We then evolve it for 4.5×10^5 Monte Carlo steps (MCS) under weak pressure and quench to 3000K, a temperature significantly below the melting temperature of polycrystalline graphene. To improve our statistics, all statistical data presented in the chapter is obtained by repeating the evolution process 50 times using different random number seeds. The simulations were performed on an Intel i7-9700 CPU, with an average runtime of approximately 0.02s per MCS. Figures 5.3(a) and 5.3(b) display the distributions of bond angles and bond lengths for different times, respectively. Note here that in flat polycrystalline graphene, the third term in the potential function [Eq. (5.1)] related to dihedral angles can be neglected due to the absence of out-of-plane forces. Consequently, the bond angles gradually approach the ideal value of 120°, while the bond lengths tend to converge to 1.42Å. Figure 5.3(c) illustrates the time-dependent changes of the RDF in the range of 5Å to 10Å. With increasing time, distinct peaks of the RDF appear at multiple positions, indicating the gradual appearance of longer-ranged order and an increase in the domain area. Figure 5.3(d) displays the power-law behavior of the defect density as a function of time, with an exponent of -0.330 ± 0.002. Based on this result, we speculate that the exponent for the defect density decrease under ideal conditions (adequate statistical sampling) is $-1/3$ at $T = 3000$K. Eq. 5.2 indicates that temperature can affect the evolution by either increasing or decreasing the acceptance rate.

Figure 5.4 shows the linear relationship between the total energy and the number of 5-7 pairs; it can be linearly fitted by $f(x) = 1.75x + 7.86$. As a reference, this corresponds to the formation energy of a single Stone Wales (SW) defect in the flat polycrystalline graphene by nearly 3.5eV [99], as each SW defect consists of two 5-7 pairs.

During the growth process of polycrystalline graphene, it is common to observe the formation of domains with different lattice orientations. The lattice orientation of these domains is complex and influenced by various factors, such as the motion of individual defects, the alignment of domain boundaries, and external pressure. These factors can exert torques to the domains, leading to a certain degree of lattice rotation within the domains. For graphene, the range of the lattice orientation is $-30°$ to $30°$, with positive values indicating orientations corresponding to rotations around the z-axis in the positive direction and negative values indicating orientations pointing towards the negative direction of rotation around the z-axis. Identification of the crystal orientation in disordered 2D materials relies on descriptors to quantify the local order in atomic systems [166–169]. Here, we applied polyhedral template matching (PTM) to identify
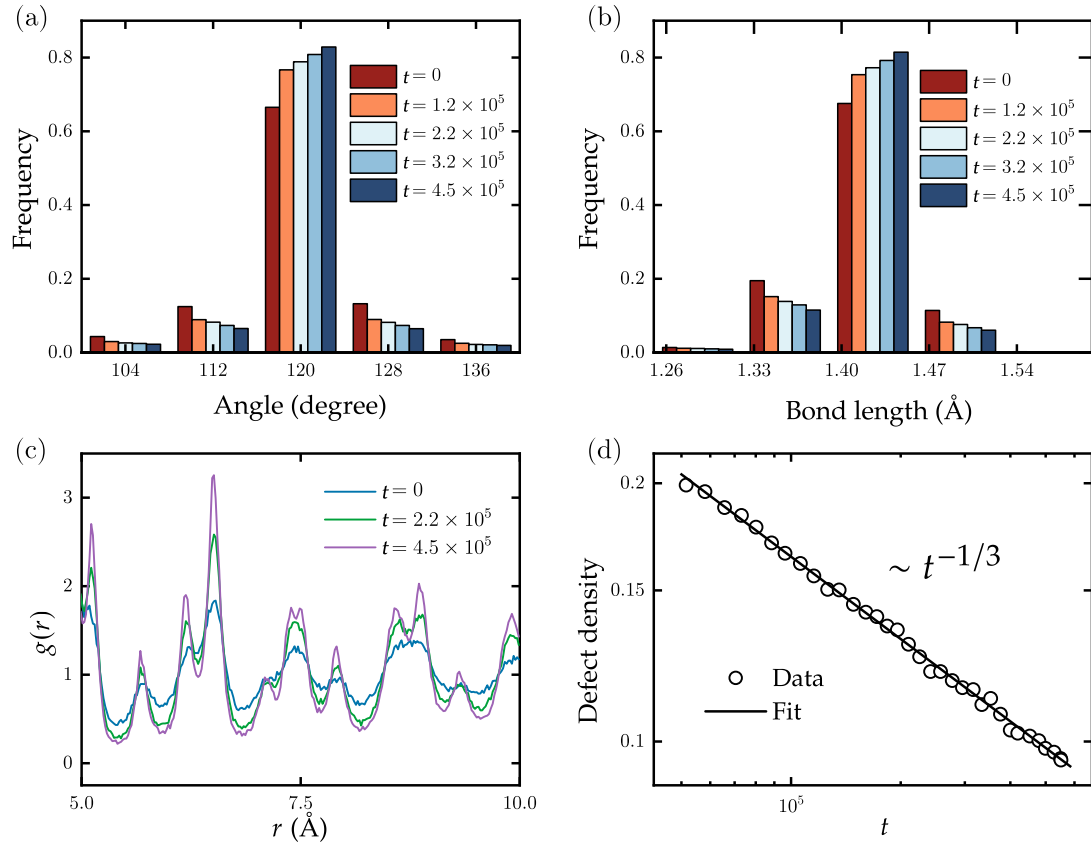
Figure 5.3: Time evolution of the distribution of (a) the bond angles and (b) the bond lengths in planar samples of graphene. With increasing simulation times, both distributions become narrower. (c) Time evolution of the radial distribution function. With increasing simulation time, the peaks at longer distance become increasingly pronounced. (d) Density of defects (5- and 7-rings) as a function of simulation time. The decay can be well fitted by a power-law decay $t^{-1/3}$ (solid line).
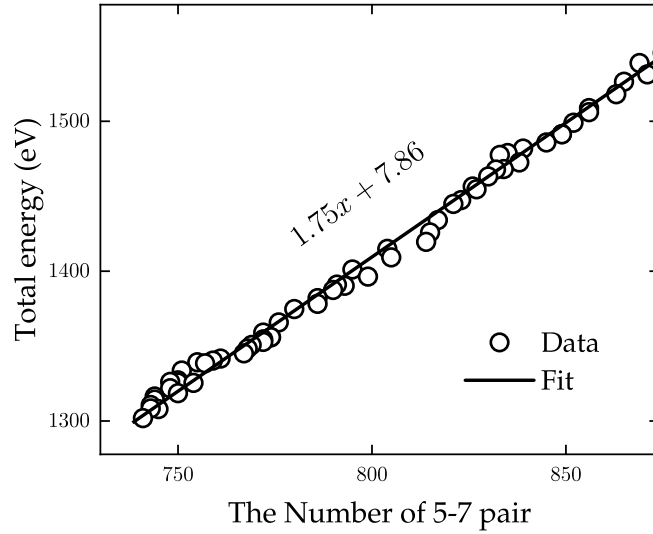
Figure 5.4: Total energy as a function of the number of defects (pairs of 5- and 7-rings) in planar graphene. The data can be well fitted with a linear relation: $E = 1.75x + 7.86$. As a reference, a single SW defect consists of two such pairs and would thus correspond to a defect formation energy of 3.5 eV.

the lattice orientation of atoms in polycrystalline graphene [170]. This method enables to classify structures according to the topology of the local atomic environment, without any ambiguity in the classification, and with greater reliability than, e.g., common neighbor analysis in the presence of thermal fluctuations. It is important to note the custom parameter root-mean squared deviation (RMSD), a higher RMSD cutoff will lead to more identifications (and fewer defect atoms), though possibly at the expense of false positives. A lower RMSD cutoff will result in fewer structural identifications (and more defect atoms and greater sensitivity to perturbations of the lattice), though possibly at the expense of false negatives. The RMSD has been set to 0.1 in our simulations to achieve optimal identification results. With this setting, the hexagonal lattice structure and defects can be identified relatively accurately. However, the identification performance for defects is not as robust as the ring identification algorithm used in the previous text, which can identify non-hexagonal ring defects with 100% accuracy.
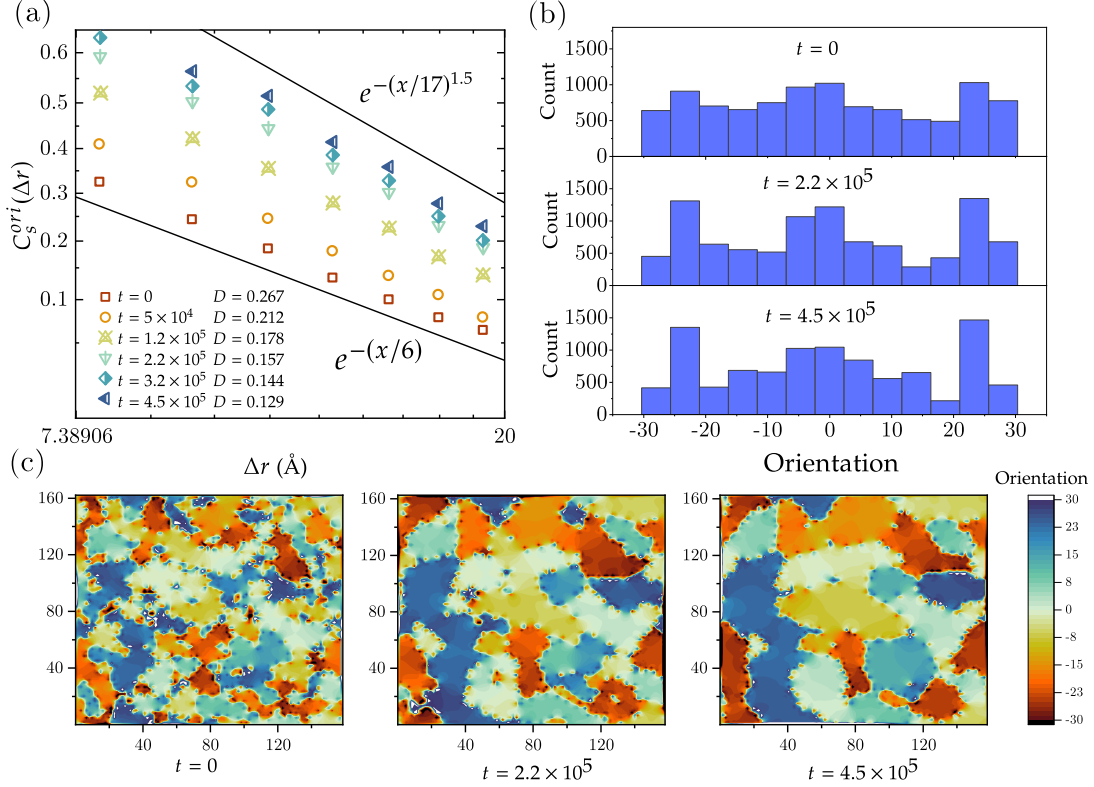
Figure 5.5: Analysis of the orientation of the hexagons in the lattice structure. (a) Normalized correlation function C_s^{ori} of the orientations as defined in Eq. (5.5), as a function of distance r, for various times. The data show a linear trend if $(-\ln(C_s^{\text{ori}}))$ is plotted as a function of distance r in a double-logarithmic plot, indicating that the correlation function C_s^{ori} decays as a stretched-exponential. (b) Histogram of the hexagon orientations at different times. While the crystalline regions grow in time, these histograms become increasingly rugged. (c) Evolution of the maps of the hexagon orientations. Some regions grow (while conserving their orientation), at the expense of other regions that shrink and sometimes disappear.

In order to investigate the spatial distribution of the lattice orientation, we define the normalized spatial correlation of the lattice orientation C_s^{ori} below,

$$C_s^{\text{ori}}\left(\Delta r\right) = \frac{\langle o_i \times o_j \rangle}{\langle o_i^2 \rangle}, \tag{5.5}$$

where o_i and o_j are the orientation of atoms i and j, respectively, $\vec{r}_i$ and $\vec{r}_j$ are the corresponding position, and with the fixed distance $\Delta r = |\vec{r}_i - \vec{r}_j|$. Figure 5.5(a) shows the variation of C_s^{ori} as a function of Δr at different times t and corresponding defect density D. The vertical axis shows $\ln[-\ln(C_s^{\text{ori}})]$, while the horizontal axis is logarithmically scaled. The data exhibits a straight decay

pattern in the figure, suggesting a trend that follows stretched exponential decay with a form like $C_s^{\text{ori}} \sim e^{-(\Delta r/b)^c}$. Due to the limitations of sample size and the effects of periodic boundary conditions, there is a significant amount of noise present on spatial scales larger than 20 Å. As a result, it becomes difficult to present the spatial correlation lattice orientation at larger scales. As shown in Fig. 5.5(a), the reference lines indicate that an anomalous exponent c is observed in the range from 1 to 1.5.

The histogram distribution plots in Fig. 5.5(b) illustrate the quantitative analysis of lattice orientations at three different times. Evidently, that there is a symmetry around zero orientation, indicating that the polycrystalline graphene can be regarded as a binary mixture composed of two types of regions: those with orientations greater than zero degrees and those with orientations less than zero degrees, in equal proportions. The average size of the binary mixture corresponds to the intersection between the correlation curve and the x-axis in Fig. 5.5(a). In the histogram, three prominent peaks are observed in the intervals $(-30°)$-$(-20°)$, $(-10°)$-$(10°)$, and $(20°)$-$(30°)$, suggesting a higher concentration of atomic orientations within these ranges. Further, we observe that as time progresses from $t = 0$ to $t = 4.5 \times 10^5$ in terms of MCS, the intensity of these peaks increases, which is also in line with the lattice orientation distribution map shown in Fig. 5.5(c). There is a trend suggesting that smaller regions with the same orientation have a higher tendency to merge into larger regions, and regions with similar orientations are more prone to fusion.

5.4.2 Dynamics of crystal phases

In the samples of polycrystalline graphene, crystal phases can be identified, each consisting of carbon atoms organized in a honeycomb lattice structure, with an orientation that differs from one domain to another. At the boundaries between domains, the three-fold coordination of the bond structure is preserved, but the honeycomb structure is discontinued by the presence of strings of 5- and 7-fold rings.

Identifying different crystal phases and their orientations can be challenging. In our simulations, we employ a method called graph clustering to identify the phases and their orientations. This approach is sensitive enough to detect sub-phases with subtle differences in domain orientations. The local structural environment and orientation of each atom is determined using the PTM algorithm, then graph edge weights are initialized as $\exp(-d^2/3)$, where d is the misorientation in degrees between two neighboring atoms. Domains are built up by contracting edges using the Node Pair Sampling method of Bonald *et al.* [171]. In our simulations, two important parameters, the merge threshold and the minimum grain size are set to 11 and 10, respectively, to achieve the best performance.

(a)

(b)

(c)

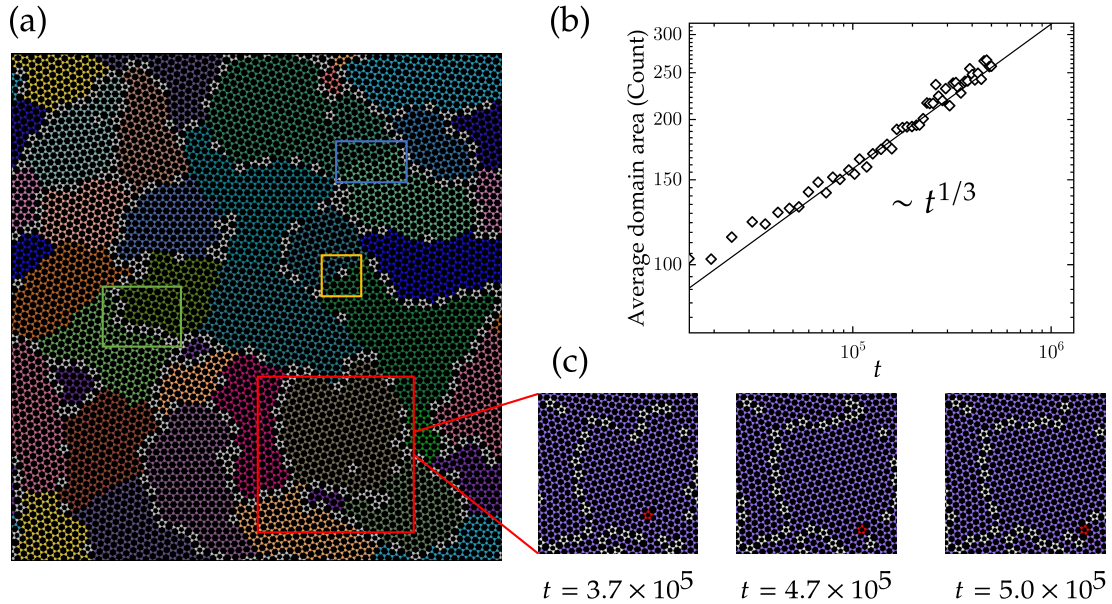$t = 3.7 \times 10^5$ $t = 4.7 \times 10^5$ $t = 5.0 \times 10^5$

Figure 5.6: (a) A polycrystalline graphene with 9800 atoms, 36 crystal phases are identified by using the graph clustering algorithm. Green, yellow and blue boxes represent three different kinds of defect structures, details see the text. (b) The average domain area changes in time, which approximately scales as a power law with 1/3 exponent. (c) Movement of a defect island from the inside domain to grain boundary, showing the diffusive behavior of defect.

Our simulations show that the dynamics of the domain structure in polycrystalline graphene are dominated by the motion of defects and domain boundaries. As shown in Fig. 5.6(a), 36 crystal phases (domains) were identified in a polycrystalline graphene consisting of 9800 atoms. Qualitatively, we observe various mechanisms that together constitute the dynamics of the domain structure. First, domain boundaries formed by strings of 5- and 7-rings separate the domains (in the green box of Fig. 5.6(a)). These domain boundaries are mobile, as is also observed experimentally using electron scanning microscopy. Second, isolated defects within the crystal domain exert a planar force on the adjacent lattices (in the yellow box of Fig. 5.6(a)). Third, shear stress generated by grain boundaries on both sides of the domain shears it into two fragments (in the blue box of Fig. 5.6(a)). During the domain growth process, the motion of defects can be classified into two scenarios. Some defects spontaneously disappear due to energy reduction, while others undergo diffusion motion. Figure 5.6(c) illustrates an example of defect diffusion, where a defect island located at the center of a domain moves to the adjacent continuous grain boundary after approximately 1.3×10^5 Monte Carlo steps. Upon reaching the grain boundary, it cannot cross over to the crystal domain on the other side of the grain boundary.

We continue with a quantitative discussion of the evolution of the domain

structure. The number of atoms in the domain is used as a representative measure of the domain area. In Fig. 5.6 (b), the average domain size is plotted as a function of time. It, square root of average domain area, exhibits a power-law increase with an exponent of 1/6. Given that the domains do not show a fractal structure, this is consistent with the decay exponent of defect density shown in Fig. 5.3(d).

At a first glance, the domain growth process in graphene resembles that of many other systems showing Ostwald ripening. A prototypical domain growth process is that in the Ising model [52]. With spin-flip (Glauber) dynamics, the theoretical framework is known as "Model A', in which domains of aligned spins grow proportional to $t^{1/2}$. If the magnetization is locally conserved, as in spin-exchange (Kawasaki) dynamics, the theoretical framework is known as "Model B", in which these domains grow proportional to $t^{1/3}$. In the case at hand, we do observe a growth exponent close to 1/3, but it is less clear that a local conservation law is active. There are a number of differences between the domain growth in graphene and the Ising model. For instance, the domains in graphene have a continuously varying orientation, rather than only "up" and "down'; additionally, long-ranged interactions might play a role, especially if buckling is allowed; and while some domain walls can easily move in some directions, the motion can be blocked in other directions. In future work, we hope to make a clearer connection between domain growth in graphene and the extensive literature on Ostwald ripening.

5.4.3 Domain growth in buckled polycrystalline graphene

The lowest-energy state of crystalline graphene in vacuum is a purely 2D structure. At finite temperature already, the carbon atoms will show out-of-plane displacements. Once structural defects are introduced, a free-floating layer of graphene will show even more structure in the out-of-plane direction. This buckling is suppressed significantly, but not completely, if the layer of graphene is placed on a substrate. For the current study on domain growth, the main effect of the substrate is the suppression of buckling. We therefore incorporate the main effect of the substrate by adding a harmonic confining energy term, defined as

$$E_s = K \sum_i^N z_i^2 \tag{5.6}$$

Here, N is the number of atoms, z_i is the normal-to-plane coordinate of the atom. The parameter K sets the strength of the interaction with substrate. Tison *et al.* [79] have reported that the buckling resulting from defects and domain boundaries extends to typically 5 to 20Å; according to our previous investigations, this corresponds to a range of K values between 0.05 and 0.3. Figure 5.7(a) displays a buckled polycrystalline graphene growing on a substrate, while Fig.

5.7(b) focuses on the evolution of defect density in time. Specifically, the density of non-hexagonal rings divided by $t^{-1/3}$ (the decay rate in the flat case), for various K values ranging from 0.01 to 2.00 eV Å^{-2}.

Notably, our findings indicate that the buckling of polycrystalline graphene significantly slows down the domain growth process. As the value of K increases, $D(t)/t^{-1/3}$ tends to reach a constant value in a shorter time. The difference for various K is however weak, because the higher buckling height Δz resulting from crystallization counteracts the suppression of substrates. In conclusion, flatter graphene exhibits faster coarsening. This intriguing observation highlights the intricate interplay between buckling, substrate effects, and defect dynamics in the crystallization process of graphene.
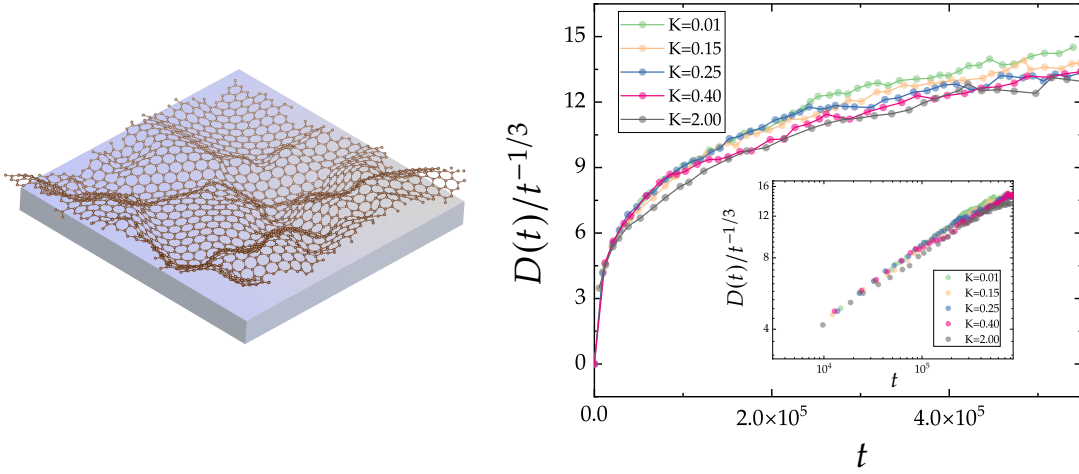
Figure 5.7: (a) A brief schematic diagram illustrating the growth of buckled polycrystalline graphene on a substrate. (b) Defect density of buckled polycrystalline graphene growing on various substrates divided by $t^{-1/3}$ (the decay rate in the flat case) over time. The inner figure is plotted on a double-logarithmic scale, demonstrating that the buckling of polycrystalline graphene slows down the crystallization rate. All samples are evolved start from an initial configuration with 20% defects density. Since well-crystallized sample leads to higher buckling height Δz, which counteracts the suppression of substrate, the difference is weak for various values of K (eV Å^{-2}).

5.5   Summary

In this chapter, we employed a recently developed and extensively validated model to investigate the dynamics of domain growth in polycrystalline graphene. The dynamics consists of a sequence of proposed bond transpositions at random locations, accepted or rejected according to Metropolis method. The technique enables access to much longer time scales, compared to molecular dynamics (MD)

method. The studied domain growth process is performed under zero pressure, quenching the system from infinite temperature to approximately 3000K. The radial distribution function shows that the spatial structures of our generated samples have good agreement with ones in experiments at the same defect density.

Through the simulations and analysis, the dynamics revealed underlying statistical mechanisms behind domain growth in polycrystalline graphene. Flat and buckled graphene are both investigated. For the flat case, we find that bond angles and bond lengths converged respectively towards 120° and 1.42Åas a function of time. The long-range disorder exhibited a gradual reduction, and the defect density, represented by the proportion of non-hexagonal rings, followed a power-law distribution with an exponent of $-1/3$ found from our simulations over time. In addition, the spatial correlation of lattice orientations statistically follows a stretched exponential form with less flat tail over times.

We identified different domains within polycrystalline graphene, and delved into discussions regarding phase separation and defect diffusion motion, the average domain size exhibits a power-law increase with an exponent of $1/6$ over times. We briefly compared the domain growth in polycrystalline graphene with the Ising dynamics. It was found that a similar growth exponent close to $1/3$ was observed in the Kawasaki dynamics with a conserved magnetization density. However, the domain growth in polycrystalline graphene exhibits more complexity. Nevertheless, we believe that this correlation will provide some guidance for our future related research.

For the buckled case, we briefly investigated the evolution of buckled polycrystalline graphene on substrates. Our findings demonstrated that the undulating buckling of polycrystalline graphene led to a reduction in the crystallization rate.

Our work may provide crucial insights into the dynamics of polycrystalline graphene during crystallization processes, which is difficult to achieve in experiments and MD simulations. Our findings also contribute to a deeper understanding of the development of advanced materials and the optimization of graphene-based applications. Moreover, the observation of reduced crystallization rates in buckled polycrystalline graphene on substrates emphasizes the need for careful consideration of substrate effects in future graphene-related research.

Summary

We have performed extensive computer simulations to study the dynamical properties. First, we study the Ising model with spin-flip dynamics at its critical point, and find that the magnetization shows anomalous dynamics, i.e. its mean squared deviation (MSD) does not increase linearly with increasing time, but instead as a power-law with an anomalous exponent $\alpha < 1$. Next, we study also the dynamical behavior of models of disordered materials, looking for anomalous dynamics. In particular, we simulate models of polycrystalline graphene and amorphous silicon (a-Si), in which the dynamics consists of a sequence of bond transpositions, in systems with periodic boundary conditions at zero pressure. We analyze the fluctuations of the area resp. volume of the periodic cell, as well as aspect ratios of the periodic cell. To characterize the anomalous dynamical properties over time scales we use two important statistical measures: the mean square displacement (MSD) and the autocorrelation function.

In Chapter 2, we have analyzed the results of extensive simulations of the two- and three-dimensional (2D and 3D) Ising model with Glauber dynamics. The MSD and the autocorrelation function of the magnetization reveal two crossover times, $\tau_1 \sim L^{z_1}$ and $\tau_2 \sim L^{z_2}$, and three separate dynamical regimes. In the short-time regime, MSD_M exhibits normal diffusion behavior, and the autocorrelation function displays an exponential decay. In the second, intermediate regime, MSD_M shows anomalous diffusive behavior, and the autocorrelation function decays in a stretched-exponential form. In the third, long-time regime, MSD_M tends to saturate at a fixed value, while the autocorrelation function shows an exponential decay again. The first crossover time is dominated by the dynamic critical exponent z_1 which was reported for the first time. Our simulation results reveal that z_1 is 0.45(5) and 1.32(2) for 2D and 3D cases, respectively. Purely based on numerical grounds, we speculate that z_1 is 1/2 for the 2D case. With the measured anomalous diffusion exponent α in the intermediate regime being 3/4 and 0.90(2), the derived second dynamic critical exponent z_2 is 13/6 and 2.032(3) for 2D and 3D, respectively, which align well with earlier reports. Due to the

existence of universality, the discovery of the first anomalous critical exponent z_1 in the Ising model with Glauber dynamics gives us reason to conjecture the presence of similar anomalous dynamical critical exponents in the Ising model with Kawasaki dynamics, the ϕ^4 model, and even more broadly, in a much wider range of systems.

In Chapter 3, we constructed two structure-related quantities in two-dimensional polycrystalline graphene, namely the area $A = L_x L_y$ and the aspect ratio $B = L_x/L_y$, where L_x and L_y are the lengths of the two sides of a rectangular polycrystalline graphene sample. A and B can easily be correlated to the material's bulk modulus and shear modulus. Then, under constant temperature and zero pressure, the dynamic evolution of $A(t)$ and $B(t)$ was constructed after applying a series of WWW moves. The mean square displacement reveals that both MSD_A and MSD_B exhibit normal diffusive behavior with diffusion coefficient D_A and D_B at short times. After a long time, due to a preferred value of the area, MSD_A tends to saturate around a certain value, while MSD_B keeps increasing. This makes the direct determination of D_B much more accurate than D_A. Our simulations also demonstrated that D_B can be linearly predicted based on the initial defect density under a fixed sample size, from which D_A can then be derived indirectly. We then show that the dynamic behavior of $B(t)$ under external forces can also be derived from D_B via the Nernst-Einstein relation. Our simulation results are in good agreement with theoretical predictions. The shear distance under external forces exhibits non-linearity (a decreasing shear rate) over time. We speculate that it results from elongated domains experiencing restoring forces that push them back toward their original shapes. Additionally, we also study the dynamics of the atomic coordinates in the out-of plane direction in buckled polycrystalline graphene and show that these present normal diffusive behavior.

In Chapter 4, similarly, we construct three structural-related quantities in amorphous silicon, which are the volume $V = L_x L_y L_z$, related to the bulk modulus, and the aspect ratios $B_1 = L_y/L_z$ and $B_2 = L_y L_z/L_x^2$, both related to the shear modulus. Our analysis reveals that at short times, the MSD for all of them exhibits normal diffusion. At longer times, they cross over to anomalous diffusion, with a temperature-dependent anomalous exponent $\alpha < 1$. We analyze our findings in the light of two standard models in statistical physics that feature anomalous dynamics, *viz.*, continuous time random walker (CTRW) and fractional Brownian motion (fBm). We obtain the distribution of waiting times, and find that the data are consistent with a stretched-exponential decay. We also show that the three quantities, V, B_1 and B_2 exhibit negative velocity autocorrelation functions. These observations together suggest that the dynamics of the material belong to the fBm class.

In Chapter 5, we employed simulations to study the domain growth process in flat polycrystalline graphene at a temperature of 3000K (below the melting point) and zero pressure. The polycrystalline graphene samples we generated were structurally well matched with experimental data, as verified by the radial

distribution function. During the domain growth process, the bond angles and bond lengths statistically tended to 120° and 1.42Å, respectively. Meanwhile, the long-range disorder significantly diminished, and the defect density decayed over time in a power-law form. We also investigated the spatial autocorrelation function of crystal orientations, which showed a decline in the stretched exponential form. The statistics and spatial distribution of the crystal orientations visually demonstrated that large-area domains tend to "engulf" adjacent small-area domains. Subsequently, we investigated the grain size growth with time, and found this to be related to a power-law with an exponent close to 1/3. This reminded us of systems also exhibiting Ostwald ripening, such as the Ising model below the critical temperature. In the Ising model with Kawasaki dynamics, known as an example of "Model B", the exponent for domain growth is also 1/3. However, the process of domain growth in polycrystalline graphene is influenced by more complex factors. We believe that our discussion can provide reference for future research. Finally, we studied the effect of the substrate on the domain growth process in buckled polycrystalline graphene, and although this effect is weak, our simulation results showed that a stronger graphene buckling tends to reduce the crystallization rate.

Samenvatting

Met behulp van computersimulaties hebben wij dynamische eigenschappen bestudeerd. Als eerste hebben we het Ising model bestudeerd, met spin-flip dynamica in het kritische punt, en we vinden dat de magnetisatie anomaal dynamisch gedrag vertoont, oftewel dat de gemiddelde kwadratische verandering niet lineair groeit met de tijd, maar in de plaats daarvan een machtswet volgt met een anomale exponent $\alpha < 1$. Vervolgens hebben we ook het dynamisch gedrag bestudeerd van modellen van ongeordende materialen, met oog voor anomaal dynamisch gedrag. Meer specifiek hebben we modellen gesimuleerd van polykristallijn grafeen en amorf silicium, waarbij de dynamica bestaat uit bondtransposities, in systemen met periodieke randvoorwaarden en zonder externe druk. We analyseren de fluctuaties van het oppervlak, resp. volume van de periodieke cel, alsmede de relatieve verhoudingen van de periodieke cel. Om de anomale dynamische eigenschappen als functie van tijd te karakteriseren gebruiken we twee maten: de gemiddelde kwadratische verandering en de autocorrelatie-functie.

In hoofdstuk 2 presenteren we de resultaten van grootschalige simulaties van het Ising model in twee en drie dimensies, met Glauber dynamica. De gemiddelde kwadratische verandering en de autocorrelatie-functie van de magnetisatie laten overgangen zien op twee verschillende tijden $\tau_1 \sim L^{z_1}$ en $\tau_2 \sim L^{z_2}$, en drie dynamische regimes. In het vroege regime vertoont de gemiddelde kwadratische verandering normaal diffusief gedrag en vervalt de autocorrelatie-functie exponentieel. In het tweede, tussenliggende regime vertoont de gemiddelde kwadratische verandering anomaal diffusief gedrag en de autocorrelatie-functie stretched-exponentieel verval. In het derde regime, over lange tijden, benadert de gemiddelde kwadratische verandering van de magnetisatie een constante, en vervalt de autocorrelatie-functie weer exponentieel. De eerste overgang gebeurt op een tijd bepaald door een dynamische kritische exponent z_1 die voor het eerst gerapporteerd wordt. Onze simulaties laten zien dat z_1 gelijk is aan 0.45(5) en 1.32(2) in respectievelijk 2D en 3D. Puur gebaseerd op numerieke resultaten speculeren we dat z_1 gelijk is aan $1/2$ in twee dimensies. In combinatie met een anomale exponent

α in het tussenliggende regime die $3/4$ en $2.032(3)$ is voor respectievelijk 2D en 3D, levert dat een tweede kritische dynamische exponent z_2 op van $13/6$ resp. $2.032(3)$ voor 2D en 3D, in lijn met eerder gerapporteerde waarden. In het licht van universaliteit verwachten wij dat het door ons gerapporteerde gedrag van het Ising model met Glauber dynamica ook vertoond wordt door het Ising model met Kawasaki dynamica, het ϕ^4 model en veel meer modellen.

In hoofdstuk 3 bestudeerden we twee structurele grootheden in twee-dimensionaal polykristallijn grafeen, namelijk de oppervlakte $A = L_x L_y$ en de lengteverhouding $B = L_x/L_y$, waarin L_x en L_y de lengtes zijn van de twee zijden van het rechthoekige sample van polykristallijn grafeen. A en B zijn direct gerelateerd aan de bulk modulus en shear modulus van het materiaal. Vervolgens bestudeerden we de evolutie van $A(t)$ en $B(t)$ tijdens een serie van bond transposities, bij constante temperatuur en zonder externe druk. De gemiddelde kwadratische verandering MSD_A en MSD_B van A en B laten normaal diffusief gedrag zien over korte tijdschalen, met diffusieconstanten D_A en D_B. Over lange tijden laat MSD_A afvlakking zien naar een constante, door de voorkeur voor een bepaalde oppervlakte A, en MSD_B blijft stijgen. Hierdoor kan D_B met een grotere nauwkeurigheid bepaald worden dan D_A, Onze simulaties laten zien dat D_B bepaald wordt door de aanvankelijke dichtheid van defects, en daarvanuit kan D_A indirect bepaald worden. Vervolgens laten we zien dat de evolutie van $B(t)$ onder een externe schuifkracht afgeleid kan worden met de Nernst-Einstein relatie, gebruik makend van D_B. Onze simulaties bevestigen de theoretische verwachtingen. Ook laten we zien dat de afschuifafstand onder een externe schuifkracht uiteindelijk minder dan lineair groeit met de tijd. We speculeren dat dit het gevolg is van krachten die domeinen die in één richting uitrekken door de afschuiving, terugduwen naar hun oorspronkelijke vorm. Ten slotte bestuderen we de dynamica van de koolstofatomen in gerimpeld grafeen, in de richting loodrecht op het grafeenvlak, en we laten zien dat deze normaal diffusief gedrag vertonen.

Hoofdstuk 4 lijkt sterk op het voorgaande hoofdstuk, maar dan wordt amorf silicium bestudeerd, waarin het volume $V = L_x L_y L_z$ gerelateerd is aan de bulk modulus, en de verhoudingen $B_1 = L_y/L_z$ en $B_2 = L_y L_z/L_x^2$ aan de shear modulus. Uit onze analyse blijkt dat over korte tijdschalen, de gemiddelde kwadratische verandering van al deze variabelen normaal diffusief gedrag vertoont. Over langere tijdschalen gaat dit over in anomaal diffusief gedrag, met een temperatuur-afhankelijke anomale exponent $\alpha < 1$. We vergelijken onze resultaten met twee statistisch-fysische standaardmodellen die anomaal-diffusief gedrag vertonen: continuous time random walker (CTRW) en fractional Brownian motion (fBm). We bepalen de distributie van de verblijftijden, en vinden dat deze data consistent zijn met stretched-exponentieel verval. We laten ook zien dat de drie variabelen V, B_1 en B_2 een negatieve snelheids-autocorrelatie laten zien. Gecombineerd suggereren deze bevindingen dat de dynamica van het materiaal behoort tot de fBm-klasse.

In hoofdstuk 5 gebruiken we simulaties voor de studie van domeingroei in vlak

polykristallijn grafeen bij een temperatuur van 3000K (onder de smelttemperatuur), in afwezigheid van externe druk. De structuur van onze samples van polykristallijn grafeen komt goed overeen met experimentele data, zoals blijkt uit de radiële distributiefunctie. Tijdens de domeingroei convergeren de bindingshoeken en bondlengtes naar respectievelijk $120°$ and 1.42Å. Dit terwijl de ongeordendheid afneemt en de concentratie van defects daalt volgens een machtswet. We onderzoeken ook de ruimtelijke autocorrelatie van de kristaloriëntaties, die een stretched-exponentiële daling vertoont. De statistiek en een visuele inspectie van de ruimtelijke verdeling van de kristaloriëntaties laten zien dat kleine domeinen vaak omringd zijn door grotere domeinen. Vervolgens bepalen we de groeisnelheid van de domeinen, en vinden dat deze een machtswet met exponent 1/3 volgt. Systemen met Ostwald ripening in de klasse "Model B", zoals het Ising model met Kawasaki dynamica, hebben ook een groei-exponent van 1/3. Het groeiproces in polykristallijn grafeen is echter meer complex. Mogelijk kan ons onderzoek een basis zijn voor toekomstig onderzoek. Ook hebben we gekeken naar het effect van het substraat op de domeingroei in gerimpeld grafeen, en al is het effect niet sterk, onze resultaten tonen wel aan dat sterkere rimpels leiden tot minder snelle domeingroei.

Bibliography

[1] Paolo Ossi. *Disordered materials: an introduction.* Springer Science & Business Media, 2010.

[2] Ed Gerstner. Nobel prize 2010: Andre geim & konstantin novoselov. *Nature physics*, 6(11):836–836, 2010.

[3] Vikas Berry. Impermeability of graphene and its applications. *Carbon*, 62:1–10, 2013.

[4] Phaedon Avouris and Fengnian Xia. Graphene applications in electronics and photonics. *Mrs bulletin*, 37(12):1225–1234, 2012.

[5] Chul Chung, Young-Kwan Kim, Dolly Shin, Soo-Ryoon Ryoo, Byung Hee Hong, and Dal-Hee Min. Biomedical applications of graphene and graphene oxide. *Accounts of chemical research*, 46(10):2211–2224, 2013.

[6] Edward P Randviir, Dale AC Brownson, and Craig E Banks. A decade of graphene research: production, applications and outlook. *Materials today*, 17(9):426–432, 2014.

[7] Edward L Wolf. *Applications of graphene: an overview.* Springer, 2014.

[8] Oleg V Yazyev and Yong P Chen. Polycrystalline graphene and other two-dimensional materials. *Nature nanotechnology*, 9(10):755–767, 2014.

[9] Kwanpyo Kim, Zonghoon Lee, William Regan, C Kisielowski, MF Crommie, and A Zettl. Grain boundary mapping in polycrystalline graphene. *ACS nano*, 5(3):2142–2146, 2011.

[10] Pinshane Y. Huang, Carlos S. Ruiz-Vargas, Arend M. van der Zande, William S. Whitney, Mark P. Levendorf, Joshua W. Kevek, Shivank Garg, Jonathan S. Alden, Caleb J. Hustedt, Ye Zhu, Jiwoong Park, Paul L.

McEuen, and David A. Muller. Grains and grain boundaries in single-layer graphene atomic patchwork quilts. *Nature*, 469:389–392, 2011.

[11] Sami Malola, Hannu Häkkinen, and Pekka Koskinen. Structural, chemical, and dynamical trends in graphene grain boundaries. *Physical review B*, 81(16):165447, 2010.

[12] David E Carlson and Cristopher R Wronski. Amorphous silicon solar cell. *Applied physics Letters*, 28(11):671–673, 1976.

[13] B Rech and H Wagner. Potential of amorphous silicon for solar cells. *Applied physics A*, 69:155–167, 1999.

[14] Sascha Sebastian Wald. *Thermalisation and Relaxation of Quantum Systems*. PhD thesis, Université de Lorraine, 2017.

[15] Ernst Ising. *Beitrag zur theorie des ferro-und paramagnetismus*. PhD thesis, Grefe & Tiedemann Hamburg, Germany, 1924.

[16] Lars Onsager. Crystal statistics. i. a two-dimensional model with an order-disorder transition. *Physical review*, 65(3-4):117, 1944.

[17] J. J Binney and N. J Dowrick. Fisher a j & newman me the theory of critical phenomena, 1995.

[18] Nicholas Metropolis, Arianna W Rosenbluth, Marshall N Rosenbluth, Augusta H Teller, and Edward Teller. Equation of state calculations by fast computing machines. *The journal of chemical physics*, 21(6):1087–1092, 1953.

[19] W Keith Hastings. Monte carlo sampling methods using markov chains and their applications. 1970.

[20] Kyozi Kawasaki. Diffusion constants near the critical point for time-dependent ising models. i. *Physical review*, 145(1):224, 1966.

[21] Ulli Wolff. Collective monte carlo updating for spin systems. *Physical review letters*, 62(4):361, 1989.

[22] Robert H Swendsen and Jian-Sheng Wang. Nonuniversal critical dynamics in monte carlo simulations. *Physical review letters*, 58(2):86, 1987.

[23] Kei Ito and Syuji Miyazaki. Crossover between anomalous superdiffusion and normal diffusion in oscillating convection flows. *Progress of theoretical physics*, 110(5):875–887, 2003.

[24] SERGEI Fomin, Vladimir Chugunov, and TOSHIYUKI Hashida. Mathematical modeling of anomalous diffusion in porous media. *Fractional differential calculus*, 1(1):1–28, 2011.

[25] Aljaž Godec, Maximilian Bauer, and Ralf Metzler. Collective dynamics effect transient subdiffusion of inert tracers in flexible gel networks. *New journal of physics*, 16(9):092002, 2014.

[26] Iva Marija Tolić-Nørrelykke, Emilia-Laura Munteanu, Genevieve Thon, Lene Oddershede, and Kirstine Berg-Sørensen. Anomalous diffusion in living yeast cells. *Physical review letters*, 93(7):078102, 2004.

[27] Dan V Nicolau, John F Hancock, and Kevin Burrage. Sources of anomalous diffusion on cell membranes: a monte carlo study. *Biophysical journal*, 92(6):1975–1987, 2007.

[28] Vasiliki Plerou, Parameswaran Gopikrishnan, Luís A Nunes Amaral, Xavier Gabaix, and H Eugene Stanley. Economic fluctuations and anomalous diffusion. *Physical review E*, 62(3):R3023, 2000.

[29] Igor M Sokolov. Models of anomalous diffusion in crowded environments. *Soft matter*, 8(35):9043–9052, 2012.

[30] Alessandro Taloni, Ophir Flomenbom, Ramón Castañeda-Priego, and Fabio Marchesoni. Single file dynamics in soft materials. *Soft matter*, 13(6):1096–1106, 2017.

[31] Seung Yun Yang, Jeong-A Yang, Eung-Sam Kim, Gumhye Jeon, Eun Ju Oh, Kwan Yong Choi, Sei Kwang Hahn, and Jin Kon Kim. Single-file diffusion of protein drugs through cylindrical nanochannels. *ACS nano*, 4(7):3817–3822, 2010.

[32] Qu Chen, Joshua D Moore, Ying-Chun Liu, Thomas J Roussel, Qi Wang, Tao Wu, and Keith E Gubbins. Transition from single-file to fickian diffusion for binary mixtures in single-walled carbon nanotubes. *The journal of chemical physics*, 133(9), 2010.

[33] Ludvig Lizana and Tobias Ambjörnsson. Single-file diffusion in a box. *Physical review letters*, 100(20):200601, 2008.

[34] Andrei N Kolmogorov. Wienersche spiralen und einige andere interessante kurven in hilbertscen raum, cr (doklady). *Acad. Sci. URSS (NS)*, 26:115–118, 1940.

[35] Laurent Decreusefond and Ali S Üstünel. Stochastic analysis of the fractional brownian motion. *Potential analysis*, 10:177–214, 1999.

[36] Benoit B Mandelbrot and John W Van Ness. Fractional brownian motions, fractional noises and applications. *SIAM review*, 10(4):422–437, 1968.

[37] L Chris G Rogers. Arbitrage with fractional brownian motion. *Mathematical finance*, 7(1):95–105, 1997.

[38] Ilkka Norros. On the use of fractional brownian motion in the theory of connectionless networks. *IEEE Journal on selected areas in communications*, 13(6):953–962, 1995.

[39] Elliott W Montroll. Random walks on lattices. In *Proc. symp. appl. math*, volume 16, pages 193–220, 1964.

[40] J Klafter and R Silbey. Derivation of the continuous-time random-walk equation. *Physical review letters*, 44(2):55, 1980.

[41] Eli Barkai, Ralf Metzler, and Joseph Klafter. From continuous time random walks to the fractional fokker-planck equation. *Physical review E*, 61(1):132, 2000.

[42] Ryszard Kutner and Jaume Masoliver. The continuous time random walk, still trendy: fifty-year history, state of art and outlook. *The european physical journal B*, 90:1–13, 2017.

[43] Eli Barkai and Yuan-Chung Cheng. Aging continuous time random walks. *The journal of chemical physics*, 118(14):6167–6178, 2003.

[44] Jaume Masoliver, Miquel Montero, and George H Weiss. Continuous-time random-walk model for financial distributions. *Physical review E*, 67(2):021112, 2003.

[45] Pierre Barthelemy, Jacopo Bertolotti, and Diederik S Wiersma. A lévy flight for light. *Nature*, 453(7194):495–498, 2008.

[46] Alexander A Dubkov, Bernardo Spagnolo, and Vladimir V Uchaikin. Lévy flight superdiffusion: an introduction. *International journal of bifurcation and chaos*, 18(09):2649–2672, 2008.

[47] Alexei V Chechkin, Ralf Metzler, Joseph Klafter, and Vsevolod Yu Gonchar. Introduction to the theory of lévy flights. *Anomalous transport: foundations and applications*, pages 129–162, 2008.

[48] Michael E Fisher. The renormalization group in the theory of critical behavior. *Reviews of modern physics*, 46(4):597, 1974.

[49] Michael E Fisher. Renormalization group theory: Its basis and formulation in statistical physics. *Reviews of modern physics*, 70(2):653, 1998.

[50] E. Ising. Beitrag zur theorie des ferromagnetismus. *Z. Physik*, 31:253–258, 1925.

[51] David Landau and Kurt Binder. *A guide to Monte Carlo simulations in statistical physics*. Cambridge university press, 2021.

[52] Mark EJ Newman and Gerard T Barkema. *Monte Carlo methods in statistical physics*. Clarendon press, 1999.

[53] Daniel J Amit and Victor Martin-Mayor. *Field theory, the renormalization group, and critical phenomena: graphs to computers*. World scientific publishing company, 2005.

[54] Pierre C Hohenberg and Bertrand I Halperin. Theory of dynamic critical phenomena. *Reviews of modern physics*, 49(3):435, 1977.

[55] R Folk and Günter Moser. Critical dynamics: a field-theoretical approach. *Journal of physics A: mathematical and general*, 39(24):R207, 2006.

[56] Martin Hasenbusch, Andrea Pelissetto, and Ettore Vicari. Relaxational dynamics in 3d randomly diluted ising models. *Journal of statistical mechanics: theory and experiment*, 2007(11):P11009, 2007.

[57] Wei Zhong, Gerard T Barkema, and Debabrata Panja. Super slowing down in the bond-diluted ising model. *Physical review E*, 102(2):022132, 2020.

[58] MP Nightingale and HWJ Blöte. Dynamic exponent of the two-dimensional ising model and monte carlo computation of the subdominant eigenvalue of the stochastic matrix. *Physical review letters*, 76(24):4548, 1996.

[59] Martin Hasenbusch. Dynamic critical exponent z of the three-dimensional ising universality class: Monte carlo simulations of the improved blume-capel model. *Physical review E*, 101(2):022126, 2020.

[60] Filip Kos, David Poland, David Simmons-Duffin, and Alessandro Vichi. Precision islands in the ising and o (n) models. *Journal of high energy physics*, 2016(8):1–16, 2016.

[61] Alan M Ferrenberg, Jiahao Xu, and David P Landau. Pushing the limits of monte carlo simulations for the three-dimensional ising model. *Physical review E*, 97(4):043301, 2018.

[62] Fabio Martinelli. Lectures on glauber dynamics for discrete spin models. *Lectures on probability theory and statistics (Saint-Flour, 1997)*, 1717:93–191, 1999.

[63] Dana Randall and Prasad Tetali. Analyzing glauber dynamics by comparison of markov chains. *Journal of mathematical physics*, 41(3):1598–1615, 2000.

[64] Claude Coulon, Rodolphe Clérac, Lollita Lecren, Wolfgang Wernsdorfer, and Hitoshi Miyasaka. Glauber dynamics in a single-chain magnet: From theory to real systems. *Physical review B*, 69(13):132408, 2004.

[65] BCS Grandi and W Figueiredo. Critical exponents of the ising model with competing glauber and kawasaki dynamics. *Physical review E*, 53(5):5484, 1996.

[66] G De Smedt, C Godreche, and JM Luck. Metastable states of the ising chain with kawasaki dynamics. *The european physical journal B-condensed matter and complex systems*, 32:215–225, 2003.

[67] Claude Godreche, Florent Krzakała, and Federico Ricci-Tersenghi. Non-equilibrium critical dynamics of the ferromagnetic ising model with kawasaki dynamics. *Journal of statistical mechanics: theory and experiment*, 2004(04):P04007, 2004.

[68] Paul D Coddington and Clive F Baillie. Empirical relations between static and dynamic exponents for ising model cluster algorithms. *Physical review letters*, 68(7):962, 1992.

[69] Heiko Rieger and Naoki Kawashima. Application of a continuous time cluster algorithm to the two-dimensional random quantum ising ferromagnet. *The european physical Journal B-condensed matter and complex systems*, 9:233–236, 1999.

[70] Henk WJ Blöte and Youjin Deng. Cluster monte carlo simulation of the transverse ising model. *Physical review E*, 66(6):066110, 2002.

[71] HK Janssen, B Schaub, and B Schmittmann. New universal short-time scaling behaviour of critical relaxation processes. *Zeitschrift für physik B condensed matter*, 73:539–549, 1989.

[72] Wei Zhong, Gerard T Barkema, Debabrata Panja, and Robin C Ball. Critical dynamical exponent of the two-dimensional scalar $\phi 4$ model with local moves. *Physical review E*, 98(6):062128, 2018.

[73] HWJ Blote, Erik Luijten, and Jouke R Heringa. Ising universality in three dimensions: a monte carlo study. *Journal of physics A: mathematical and general*, 28(22):6289, 1995.

[74] MP Nightingale and HWJ Blöte. Universal ising dynamics in two dimensions. *Physica A: statistical mechanics and its applications*, 251(1-2):211–223, 1998.

[75] M Hasenbusch, K Pinn, and S Vinti. Critical exponents of the three-dimensional ising universality class from finite-size scaling with standard and improved actions. *Physical review B*, 59(17):11471, 1999.

[76] Wei Zhong, Debabrata Panja, and Gerard T Barkema. Approximate dynamical eigenmodes of the ising model with local spin-exchange moves. *Physical review E*, 100(1):012132, 2019.

[77] Of course the total magnetization (zero mode) is not a good observable in this case, as it is strictly conserved; so one has to study, for instance, the first fourier mode of the magnetization.

[78] Haider I Rasool, Colin Ophus, Ziang Zhang, Michael F Crommie, Boris I Yakobson, and Alex Zettl. Conserved atomic bonding sequences and strain organization of graphene grain boundaries. *Nano letters*, 14(12):7057–7063, 2014.

[79] Yann Tison, Jérôme Lagoute, Vincent Repain, Cyril Chacon, Yann Girard, Frédéric Joucken, Robert Sporken, Fernando Gargiulo, Oleg V Yazyev, and Sylvie Rousset. Grain boundaries in graphene on sic (0001) substrate. *Nano letters*, 14(11):6382–6386, 2014.

[80] Paulo T Araujo, Mauricio Terrones, and Mildred S Dresselhaus. Defects and impurities in graphene-like materials. *Materials today*, 15(3):98–109, 2012.

[81] Thomas Trevethan, Christopher D Latham, Malcolm I Heggie, Patrick R Briddon, and Mark J Rayson. Vacancy diffusion and coalescence in graphene directed by defect strain fields. *Nanoscale*, 6(5):2978–2986, 2014.

[82] Teng Cui, Sankha Mukherjee, Parambath M Sudeep, Guillaume Colas, Farzin Najafi, Jason Tam, Pulickel M Ajayan, Chandra Veer Singh, Yu Sun, and Tobin Filleter. Fatigue of graphene. *Nature materials*, 19(4):405–411, 2020.

[83] Eric Ganz, Ariel B Ganz, Li-Ming Yang, and Matthew Dornfeld. The initial stages of melting of graphene between 4000 k and 6000 k. *Physical chemistry chemical physics*, 19(5):3756–3762, 2017.

[84] Pattabhi R Budarapu, Brahmanandam Javvaji, VK Sutrakar, D Roy Mahapatra, Goangseup Zi, and Timon Rabczuk. Crack propagation in graphene. *Journal of applied physics*, 118(6):064307, 2015.

[85] Linchun He, Siusiu Guo, Jincheng Lei, Zhendong Sha, and Zishun Liu. The effect of stone–thrower–wales defects on mechanical properties of graphene sheets–a molecular dynamics study. *Carbon*, 75:124–132, 2014.

[86] William Houlder Zachariasen. The atomic arrangement in glass. *Journal of the american chemical society*, 54(10):3841–3851, 1932.

[87] 9_F Wooten, K Winer, and D Weaire. Computer generation of structural models of amorphous si and ge. *Physical review letters*, 54(13):1392, 1985.

[88] F Wooten and D Weaire. Modeling tetrahedrally bonded random networks by computer. *Solid state physics*, 40:1–42, 1987.

[89] PN Keating. Effect of invariance requirements on the elastic strain energy of crystals with application to the diamond structure. *Physical review*, 145(2):637, 1966.

[90] Aron W Cummings, Simon M-M Dubois, Jean-Christophe Charlier, and Stephan Roche. Universal spin diffusion length in polycrystalline graphene. *Nano letters*, 19(10):7418–7426, 2019.

[91] Yuqiang Zeng, Chun-Li Lo, Shengjiao Zhang, Zhihong Chen, and Amy Marconnet. Dynamically tunable thermal transport in polycrystalline graphene by strain engineering. *Carbon*, 158:63–68, 2020.

[92] Ming Chen, Zhixun Wang, Xin Ge, Zhe Wang, Kazunori Fujisawa, Juan Xia, Qingsheng Zeng, Kaiwei Li, Ting Zhang, Qichong Zhang, et al. Controlled fragmentation of single-atom-thick polycrystalline graphene. *Matter*, 2(3):666–679, 2020.

[93] David Estrada, Zuanyi Li, Gyung-Min Choi, Simon N Dunham, Andrey Serov, Jungchul Lee, Yifei Meng, Feifei Lian, Ning C Wang, Alondra Perez, et al. Thermal transport in layer-by-layer assembled polycrystalline graphene films. *npj 2D Materials and applications*, 3(1):1–7, 2019.

[94] Sanghoon Park, Muhammad Arslan Shehzad, Muhammad Farooq Khan, Ghazanfar Nazir, Jonghwa Eom, Hwayong Noh, and Yongho Seo. Effect of grain boundaries on electrical properties of polycrystalline graphene. *Carbon*, 112:142–148, 2017.

[95] Teng Ma, Zhibo Liu, Jinxiu Wen, Yang Gao, Xibiao Ren, Huanjun Chen, Chuanhong Jin, Xiu-Liang Ma, Ningsheng Xu, Hui-Ming Cheng, et al. Tailoring the thermal and electrical transport properties of graphene films by grain size engineering. *Nature communications*, 8(1):1–9, 2017.

[96] Yufei Gao, Yuhang Jing, Jiaqiu Liu, Xiaochuan Li, and Qingyuan Meng. Tunable thermal transport properties of graphene by single-vacancy point defect. *Applied thermal engineering*, 113:1419–1425, 2017.

[97] Shuang Wu, Bing Liu, Cheng Shen, Si Li, Xiaochun Huang, Xiaobo Lu, Peng Chen, Guole Wang, Duoming Wang, Mengzhou Liao, et al. Magneto-transport properties of graphene nanoribbons with zigzag edges. *Physical review letters*, 120(21):216601, 2018.

[98] V Torres, D Faria, and A Latgé. Tuning transport properties of graphene three-terminal structures by mechanical deformation. *Physical review B*, 97(16):165429, 2018.

[99] Sandeep K Jain, Gerard T Barkema, Normand Mousseau, Chang-Ming Fang, and Marijn A van Huis. Strong long-range relaxations of structural defects in graphene simulated using a new semiempirical potential. *The Journal of physical chemistry C*, 119(17):9646–9655, 2015.

[100] Sandeep K Jain, Vladimir Juricic, and Gerard T Barkema. Probing crystallinity of graphene samples via the vibrational density of states. *The journal of physical chemistry letters*, 6(19):3897–3902, 2015.

[101] Albert J Pool, Sandeep K Jain, and Gerard T Barkema. Structural characterization of carbon nanotubes via the vibrational density of states. *Carbon*, 118:58–65, 2017.

[102] Sandeep K Jain, Vladimir Juričić, and Gerard T Barkema. Structure of twisted and buckled bilayer graphene. *2D Materials*, 4(1):015018, 2016.

[103] Sandeep K Jain, Vladimir Juričić, and Gerard T Barkema. Probing the shape of a graphene nanobubble. *Physical chemistry chemical physics*, 19(11):7465–7470, 2017.

[104] Federico D'Ambrosio, Vladimir Juričić, and Gerard T Barkema. Discontinuous evolution of the structure of stretching polycrystalline graphene. *Physical review B*, 100(16):161402, 2019.

[105] Franz Aurenhammer and Rolf Klein. Voronoi diagrams. *Handbook of computational geometry*, 5(10):201–290, 2000.

[106] Erik Bitzek, Pekka Koskinen, Franz Gähler, Michael Moseler, and Peter Gumbsch. Structural relaxation made simple. *Physical review letters*, 97(17):170201, 2006.

[107] Julien Guénolé, Wolfram G Nöhring, Aviral Vaid, Frédéric Houllé, Zhuocheng Xie, Aruna Prakash, and Erik Bitzek. Assessment and optimization of the fast inertial relaxation engine (fire) for energy minimization

in atomistic simulations and its implementation in lammps. *Computational materials science*, 175:109584, 2020.

[108] Xuesong Li, Carl W Magnuson, Archana Venugopal, Jinho An, Ji Won Suk, Boyang Han, Mark Borysiak, Weiwei Cai, Aruna Velamakanni, Yanwu Zhu, et al. Graphene films with large domain size by a two-step chemical vapor deposition process. *Nano letters*, 10(11):4328–4334, 2010.

[109] Li Lin, Hailin Peng, and Zhongfan Liu. Synthesis challenges for graphene industry. *Nature materials*, 18(6):520–524, 2019.

[110] Kaveh M Milaninia, Marc A Baldo, Alfonso Reina, and Jing Kong. All graphene electromechanical switch fabricated by chemical vapor deposition. *Applied physics letters*, 95(18):183105, 2009.

[111] Rajat K Paul, Sushmee Badhulika, Sandip Niyogi, Robert C Haddon, Veera M Boddu, Carmen Costales-Nieves, Krassimir N Bozhilov, and Ashok Mulchandani. The production of oxygenated polycrystalline graphene by one-step ethanol-chemical vapor deposition. *Carbon*, 49(12):3789–3795, 2011.

[112] Bohayra Mortazavi and Gianaurelio Cuniberti. Atomistic modeling of mechanical properties of polycrystalline graphene. *Nanotechnology*, 25(21):215704, 2014.

[113] Rassin Grantab, Vivek B Shenoy, and Rodney S Ruoff. Anomalous strength characteristics of tilt grain boundaries in graphene. *Science*, 330(6006):946–948, 2010.

[114] Na Xu, Jian-Gang Guo, and Zhen Cui. The influence of tilt grain boundaries on the mechanical properties of bicrystalline graphene nanoribbons. *Physica E: Low-dimensional systems and nanostructures*, 84:168–174, 2016.

[115] Zhigong Song, Vasilii I. Artyukhov, Boris I. Yakobson, and Zhiping Xu. Pseudo hall-petch strength reduction in polycrystalline graphene. *Nano letters*, 13:1829–1833, April 2013.

[116] Lijun Yi, Zhengnan Yin, Yingyan Zhang, and Tienchong Chang. A theoretical evaluation of the temperature and strain-rate dependent fracture strength of tilt grain boundaries in graphene. *Carbon*, 51:373–380, 2013.

[117] Jihoon Han, Dongwoo Sohn, Wanchuck Woo, and Dong-Kyu Kim. Molecular dynamics study of fracture toughness and trans-intergranular transition in bi-crystalline graphene. *Computational materials science*, 129:323–331, 2017.

[118] MAN Dewapriya and SA Meguid. Tailoring fracture strength of graphene. *Computational materials science*, 141:114–121, 2018.

[119] Bongkyun Jang, Alexander E Mag-isa, Jae-Hyun Kim, Byungwoon Kim, Hak-Joo Lee, Chung-Seog Oh, Takashi Sumigawa, and Takayuki Kitamura. Uniaxial fracture test of freestanding pristine graphene using in situ tensile tester under scanning electron microscope. *Extreme mechanics letters*, 14:10–15, 2017.

[120] Te-Huan Liu, Chun-Wei Pao, and Chien-Cheng Chang. Mechanical mutability of polycrystalline graphene from atomistic simulations. *Computational materials science*, 91:56–61, 2014.

[121] Jeffrey L Braun, Christopher H Baker, Ashutosh Giri, Mirza Elahi, Kateryna Artyushkova, Thomas E Beechem, Pamela M Norris, Zayd C Leseman, John T Gaskins, and Patrick E Hopkins. Size effects on the thermal conductivity of amorphous silicon thin films. *Physical review B*, 93(14):140201, 2016.

[122] Wu-Xing Zhou, Yuan Cheng, Ke-Qiu Chen, Guofeng Xie, Tian Wang, and Gang Zhang. Thermal conductivity of amorphous materials. *Advanced functional materials*, 30(8):1903829, 2020.

[123] Frederik Tielens, Maciej Gierada, Jarosław Handzlik, and Monica Calatayud. Characterization of amorphous silica based catalysts using dft computational methods. *Catalysis today*, 354:3–18, 2020.

[124] Xiaoning Ru, Minghao Qu, Jianqiang Wang, Tianyu Ruan, Miao Yang, Fuguo Peng, Wei Long, Kun Zheng, Hui Yan, and Xixiang Xu. 25.11% efficiency silicon heterojunction solar cell with low deposition rate intrinsic amorphous silicon buffer layers. *Solar energy materials and solar cells*, 215:110643, 2020.

[125] Shuangying Cao, Dongliang Yu, Yinyue Lin, Chi Zhang, Linfeng Lu, Min Yin, Xufei Zhu, Xiaoyuan Chen, and Dongdong Li. Light propagation in flexible thin-film amorphous silicon solar cells with nanotextured metal back reflectors. *ACS applied materials & interfaces*, 12(23):26184–26192, 2020.

[126] Mengxiao Huang, Yunfeng Wang, Ming Li, Vanhkeo Keovisar, Xuejuan Li, Decheng Kong, and Qiongfen Yu. Comparative study on energy and exergy properties of solar photovoltaic/thermal air collector based on amorphous silicon cells. *Applied thermal engineering*, 185:116376, 2021.

[127] Van-Thuc Nguyen and Te-Hua Fang. Abrasive mechanisms and interfacial mechanics of amorphous silicon carbide thin films in chemical-mechanical planarization. *Journal of alloys and compounds*, 845:156100, 2020.

[128] GT Barkema and Normand Mousseau. Identification of relaxation and diffusion mechanisms in amorphous silicon. *Physical review letters*, 81(9):1865, 1998.

[129] Mark D Kluge, John R Ray, and Aneesur Rahman. Amorphous-silicon formation by rapid quenching: A molecular-dynamics study. *Physical review B*, 36(8):4234, 1987.

[130] Federico D'Ambrosio, Joris Barkema, and Gerard T Barkema. Efficient structural relaxation of polycrystalline graphene models. *Nanomaterials*, 11(5):1242, 2021.

[131] Gerard T Barkema and Normand Mousseau. High-quality continuous random networks. *Physical review B*, 62(8):4985, 2000.

[132] Zihua Liu, Debabrata Panja, and Gerard T Barkema. Structural dynamics of polycrystalline graphene. *Physical review E*, 105(4):044116, 2022.

[133] Debabrata Panja. Generalized langevin equation formulation for anomalous polymer dynamics. *Journal of statistical mechanics: theory and experiment*, 2010(02):L02001, 2010.

[134] Debabrata Panja. Anomalous polymer dynamics is non-markovian: memory effects and the generalized langevin equation formulation. *Journal of statistical mechanics: theory and experiment*, 2010(06):P06011, 2010.

[135] Wei Zhong, Debabrata Panja, Gerard T Barkema, and Robin C Ball. Generalized langevin equation formulation for anomalous diffusion in the ising model at the critical temperature. *Physical review E*, 98(1):012124, 2018.

[136] Debabrata Panja, Gerard T Barkema, and JMJ van Leeuwen. Efficient simulation of semiflexible polymers. *Physical review E*, 92(3):032603, 2015.

[137] Ningning Song, Zan Gao, and Xiaodong Li. Tailoring nanocomposite interfaces with graphene to achieve high strength and toughness. *Science advances*, 6(42):eaba7016, 2020.

[138] Peng Zhang, Lulu Ma, Feifei Fan, Zhi Zeng, Cheng Peng, Phillip E Loya, Zheng Liu, Yongji Gong, Jiangnan Zhang, Xingxiang Zhang, et al. Fracture toughness of graphene. *Nature communications*, 5(1):3782, 2014.

[139] Ashivni Shekhawat and Robert O Ritchie. Toughness and strength of nanocrystalline graphene. *Nature communications*, 7(1):10546, 2016.

[140] Changgu Lee, Xiaoding Wei, Jeffrey W Kysar, and James Hone. Measurement of the elastic properties and intrinsic strength of monolayer graphene. *Science*, 321(5887):385–388, 2008.

[141] Ardavan Zandiatashbar, Gwan-Hyoung Lee, Sung Joo An, Sunwoo Lee, Nithin Mathew, Mauricio Terrones, Takuya Hayashi, Catalin R Picu, James Hone, and Nikhil Koratkar. Effect of defects on the intrinsic strength and stiffness of graphene. *Nature communications*, 5(1):3186, 2014.

[142] MC Wang, Cheng Yan, Lin Ma, Ning Hu, and MW Chen. Effect of defects on fracture strength of graphene sheets. *Computational materials science*, 54:236–239, 2012.

[143] Alexander A Balandin, Suchismita Ghosh, Wenzhong Bao, Irene Calizo, Desalegne Teweldebrhan, Feng Miao, and Chun Ning Lau. Superior thermal conductivity of single-layer graphene. *Nano letters*, 8(3):902–907, 2008.

[144] Shanshan Chen, Qingzhi Wu, Columbia Mishra, Junyong Kang, Hengji Zhang, Kyeongjae Cho, Weiwei Cai, Alexander A Balandin, and Rodney S Ruoff. Thermal conductivity of isotopically modified graphene. *Nature materials*, 11(3):203–207, 2012.

[145] Tae Yun Kim, Cheol-Hwan Park, and Nicola Marzari. The electronic thermal conductivity of graphene. *Nano letters*, 16(4):2439–2443, 2016.

[146] An Li, Cong Zhang, and Yang-Fei Zhang. Thermal conductivity of graphene-polymer composites: Mechanisms, properties, and applications. *Polymers*, 9(9):437, 2017.

[147] H Malekpour, K-H Chang, J-C Chen, C-Y Lu, DL Nika, KS Novoselov, and AA Balandin. Thermal conductivity of graphene laminate. *Nano letters*, 14(9):5155–5161, 2014.

[148] Haiqun Chen, Marc B Müller, Kerry J Gilmore, Gordon G Wallace, and Dan Li. Mechanically strong, electrically conductive, and biocompatible graphene paper. *Advanced materials*, 20(18):3557–3561, 2008.

[149] Yan Wang, Zhiqiang Shi, Yi Huang, Yanfeng Ma, Chengyang Wang, Mingming Chen, and Yongsheng Chen. Supercapacitor devices based on graphene materials. *The journal of physical chemistry C*, 113(30):13103–13107, 2009.

[150] Hyeokjo Gwon, Hyun-Suk Kim, Kye Ung Lee, Dong-Hwa Seo, Yun Chang Park, Yun-Sung Lee, Byung Tae Ahn, and Kisuk Kang. Flexible energy storage devices based on graphene paper. *Energy & Environmental science*, 4(4):1277–1283, 2011.

[151] Pai-Yen Chen and Andrea Alù. Terahertz metamaterial devices based on graphene nanostructures. *IEEE Transactions on terahertz science and technology*, 3(6):748–756, 2013.

[152] Fan Zhang, Tengfei Zhang, Xi Yang, Long Zhang, Kai Leng, Yi Huang, and Yongsheng Chen. A high-performance supercapacitor-battery hybrid energy storage device based on graphene-enhanced electrode materials with ultrahigh energy density. *Energy & Environmental science*, 6(5):1623–1632, 2013.

[153] YI Zhang, Luyao Zhang, and Chongwu Zhou. Review of chemical vapor deposition of graphene and related applications. *Accounts of chemical research*, 46(10):2329–2339, 2013.

[154] Xiuyun Zhang, Lu Wang, John Xin, Boris I Yakobson, and Feng Ding. Role of hydrogen in graphene chemical vapor deposition growth on a copper surface. *Journal of the american chemical society*, 136(8):3040–3047, 2014.

[155] Fengning Liu, Pai Li, Hao An, Peng Peng, Ben McLean, and Feng Ding. Achievements and challenges of graphene chemical vapor deposition growth. *Advanced functional materials*, 32(42):2203191, 2022.

[156] Piran R Kidambi, Caterina Ducati, Bruno Dlubak, Damian Gardiner, Robert S Weatherup, Marie-Blandine Martin, Pierre Seneor, Harry Coles, and Stephan Hofmann. The parameter space of graphene chemical vapor deposition on polycrystalline cu. *The journal of physical chemistry C*, 116(42):22492–22501, 2012.

[157] Neeraj Mishra, John Boeckl, Nunzio Motta, and Francesca Iacopi. Graphene growth on silicon carbide: A review. *Physica status solidi (a)*, 213(9):2277–2289, 2016.

[158] Holly Tetlow, J Posthuma De Boer, Ian J Ford, Dimitri Dimitrievich Vvedensky, Johann Coraux, and L Kantorovich. Growth of epitaxial graphene: Theory and experiment. *Physics reports*, 542(3):195–295, 2014.

[159] Yanyan Xu, Huizhe Cao, Yanqin Xue, Biao Li, and Weihua Cai. Liquid-phase exfoliation of graphene: an overview on exfoliation media, techniques, and challenges. *Nanomaterials*, 8(11):942, 2018.

[160] Artur Ciesielski and Paolo Samorì. Graphene via sonication assisted liquid-phase exfoliation. *Chemical society reviews*, 43(1):381–398, 2014.

[161] Andreas Isacsson, Aron W Cummings, Luciano Colombo, Luigi Colombo, Jari M Kinaret, and Stephan Roche. Scaling properties of polycrystalline graphene: a review. *2D Materials*, 4(1):012002, 2016.

[162] Aron W Cummings, Dinh Loc Duong, Van Luan Nguyen, Dinh Van Tuan, Jani Kotakoski, Jose Eduardo Barrios Vargas, Young Hee Lee, and Stephan Roche. Charge transport in polycrystalline graphene: challenges and opportunities. *Advanced materials*, 26(30):5079–5094, 2014.

[163] John G Kirkwood. The skeletal modes of vibration of long chain molecules. *The journal of chemical physics*, 7(7):506–509, 1939.

[164] R Ravinder, Rajesh Kumar, Manish Agarwal, and NM Anoop Krishnan. Evidence of a two-dimensional glass transition in graphene: Insights from molecular simulations. *Scientific reports*, 9(1):4517, 2019.

[165] Franz R Eder, Jani Kotakoski, Ute Kaiser, and Jannik C Meyer. A journey from order to disorder—atom by atom transformation from graphene to a 2d carbon glass. *Scientific reports*, 4(1):4060, 2014.

[166] Alexander Stukowski. Structure identification methods for atomistic simulations of crystalline materials. *Modelling and simulation in materials science and engineering*, 20(4):045021, 2012.

[167] Isaac M Felix and Luiz Felipe C Pereira. Thermal conductivity of graphene-hbn superlattice ribbons. *Scientific reports*, 8(1):2737, 2018.

[168] Pablo Miguel Ramos, Miguel Herranz, Katerina Foteinopoulou, Nikos Ch Karayiannis, and Manuel Laso. Identification of local structure in 2-d and 3-d atomic systems through crystallographic analysis. *Crystals*, 10(11):1008, 2020.

[169] Yuexing Han, Leilei Song, Bing Wang, Sheng Sun, Quan Qian, and Qian Wang. Atomicnet: a novel approach to identify the crystal structure of each simulated atom. *Modelling and simulation in materials science and engineering*, 28(3):035005, 2020.

[170] Peter Mahler Larsen, Søren Schmidt, and Jakob Schiøtz. Robust structural identification via polyhedral template matching. *Modelling and simulation in materials science and engineering*, 24(5):055007, 2016.

[171] Thomas Bonald, Bertrand Charpentier, Alexis Galland, and Alexandre Hollocou. Hierarchical graph clustering using node pair sampling. *arXiv preprint arXiv:1806.01664*, 2018.

Acknowledgments

Here, I wish to express my deepest gratitude to all those who have accompanied and encouraged me throughout my pursuit of a doctoral degree. The journey has been enriched by your presence.

In particular, I extend my sincerest thanks to my supervisor, Prof. Dr. Gerard T. Barkema. Upon my arrival in the Netherlands, I was daunted by the cultural and linguistic barriers, as well as the prospect of entering a new research field. Prof. Dr. Barkema provided immense support and encouragement during these times of confusion and anxiety. His patience was a beacon that helped me find new directions whenever I encountered obstacles in my research. Progress in my project bolstered my confidence in the field, empowering me to forge ahead with assurance. The hours spent discussing problems and writing programs with Professor Barkema are undoubtedly among the fondest memories of my doctoral life. The wealth of academic and non-academic knowledge I gained from him is an invaluable asset to my future career.

I would also like to thank my daily supervisor, Dr. Debabrata Panja, for his rapid and effective solutions to the difficulties I faced. His insightful suggestions were immensely useful for my doctoral work, and he contributed substantially to my research. From Dr. Panja, I learned a great deal about what it takes to be a competent researcher, and I will continue to strive in that direction.

My thanks go as well to the China Scholarship Council for their financial support, which allowed me the opportunity to pursue my Ph.D. at Utrecht University and to engage with so many outstanding researchers.

I am genuinely thankful to my office mate, particularly Wei Zhong, who was not just a great companion in life but also a tremendous help in my scientific endeavors. I remember the spark of interest ignited when he assisted me in completing my first small program simulation of the Ising model, marking the auspicious start of my Ph.D. journey. Our frequent discussions in the coffee room on various topics were the most delightful moments for relaxation amidst the workload. Additionally, I am grateful to D'Ambrosio Federico for his assistance with

107

my graphene simulations, which helped me quickly master the related programming skills during my first year. He always offered his help without hesitation to overcome any challenges. My gratitude is also extended to Dekker Mark, who welcomed me warmly when I first arrived in the Netherlands.

Lastly, I am eternally grateful to my family and friends, who are my steadfast support system always!

About the author

Zihua Liu was born on September 15, 1993, in Taigu County, Jinzhong, Shanxi province, China. He spent most of his childhood and completed his secondary education in Taiyuan, Shanxi province. In 2017, he received his Bachelor's degree in electronic science and technology from Guangdong University of technology in Guangzhou, Guangdong province. He then pursued a Master's degree in optical engineering at south China normal university in Guangzhou, where he was awarded the Master's degree in June 2019. During his studies, he was honored with the National scholarship of China and was selected for the national program for studying abroad. In December 2019, he commenced his Ph.D. at Utrecht University in the Netherlands, under the supervision of Prof. Dr Gerard T. Barkema, focusing on disordered materials and anomalous dynamics.